Tracing the origin of oxide inclusions in continuously casted steel using stable oxygen isotopes—An interdisciplinary approach

Dissertation
zur
Erlangung des Doktorgrades (Dr. rer. nat.)
der
Mathematisch-Naturwissenschaftlichen Fakultät
der
Rheinischen Friedrich-Wilhelms-Universität Bonn

vorgelegt von

Andreas Pack

aus

Gummersbach

Bonn 2000

Macht' ich's gut, so woll'n wir schweigen;
Macht' ich's schlimm-, so woll'n wir lachen
Und es immer schlimmer machen,
Schlimmer machen, schlimmer lachen,
Bis wir in die Grube steigen.

Freunde! Ja! So soll's geschehn? -
Amen! Und auf Wiedersehen!

Friedrich Nietzsche
Menschliches, Allzumenschliches: Ein Buch für freie Geister, 1884

Für M.

Contents

List of Figures

List of Tables

Acknowledgment

A thesis like this is never the product of one worker on his own. Many people were incorporated and all the credit is due to them. However, some of them shall be mentioned personally here at the beginning of the text.

First of all, I would like to thank my supervisor Professor Dr. S. Hoernes who contributed his knowledge and huge amounts of his steady optimism also during hard times we had with the laser line.

Dr. R. Broß (Mülheim) is thanked for initiating this work and for contributing both, samples and fruitful discussions. Without his engagement, this work would not have been possible.

Professor Dr. M. M. Raith is thanked for fruitful discussions and for undertaking the co-corrections of this thesis.

Dr. T. Walther of the Institute of Inorganic Chemistry in Bonn is thanked for conducting transmitted electron microscopy. Dr. A. Buhr (Frankfurt) is thanked for accompanying me during the sampling campaign. Professor M. Göbbels (Erlangen) is thanked for many helpful discussions and his support for the application for the DFG grant.

Holger Grote (Bonn) owns thank for many fruitful discussions and for the opportunity to use the SE-microscope at the Werkstoffzentrum Rheinbach GmbH.

Susanne Klerner is especially thanked for not loosing her patience when living together with a young scientist and his ups and downs during this work. But she owes also great thanks for introducing me into the work with the electron microprobe of the Institute of Mineralogy and Geochemistry (Cologne).

Of course my parents own great thank for giving me so much freedom and for their support.

Chapter 1

Introduction

> *In unserem deutschen Vaterlande regen sich im Verein mit der Wissenschaft zweimalhunderttausend Hände, um aus den Erzen Eisen zu gewinnen; sollte es da für uns nicht von großem Interesse sein, ihr Wirken und Schaffen uns näher zu betrachten und zu verfolgen, wie und mit welchen Mitteln sie dieses Ziel erreichen.*

A. Krauss
Eisen-Hütten-Kunde, Erster Teil: Das Roh-Eisen, 1902

1.1 The Problem: Non-metallic inclusions in continuously casted steels

Non metallic inclusions are present in all continuously casted steels. They can affect the physical and mechanical characteristics of products and, consequently, their service properties. The amount and type of non-metallic inclusions have a direct influence on properties such as:

- Welding properties
- Fatigue properties
- Finishing quality
- Cutting properties
- Ductility and brittle fracture
- Corrosion resistance

The steel makers are therefore concerned to obtain a steel as clean as possible. Only in rare cases it is desired to produce a steel grade with non-metallic inclusions of well defined

composition and distribution (Gaye et al., 1994). The different types of inclusions behave different during hot rolling or forging. According to Wijk (1995) four types of deformations of inclusions are to be distinguished:

- Deformation of ductile inclusions in a similar way as the surrounding steel matrix
- Brittle inclusions that are broken up into stringers of separate fragments during hot rolling or forging
- Inclusions with hard cores surrounded by a ductile rim. These inclusions behave ductile at low degree of deformation. At higher strain rates a thick center with prolonged ends develops.
- Very limited or no deformation of the inclusions: During rolling usually cavities open up in the pressure shadows in the rolling direction ("fish tails").

These inclusions vary in size between $<50\,\mu$m up to a few hundreds of micrometers (Zimmermann, 1974; Pleschiutschnigg, 1989). Especially large aggregates of inclusions considerably lower the quality of the final steel product. Inclusions are not only disadvantageous for the quality of the final product, but can also have a detrimental effect on the casting process.

Precipitation of inclusions along the inner walls of the submerged entry nozzle (SEN) can adversly affect the casting process. Non-metallic precipitates along the inner walls of the SEN are termed *clogging*. SEN clogging reduces pipe diameter and, consequently, can reduce the steel flow into the mould. Inclusions can deposit on the inner walls of the SEN to such an extent that total blockage of the SEN bore can occur. As the alumina build-up progresses in the bore of the SEN, it is possible that large deposits become detached from the bore and come through into the mould.

In this study, oxide SEN precipitates in low alloyed Al-killed steels were investigated. In these grades, alumina (Al_2O_3, corundum) is the predominant phase (Zimmermann, 1974; Pleschiutschnigg, 1989; Bannenberg, 1995). Corundum behaves highly brittle even at elevated temperatures of hot rolling.

It is generally accepted that alumina forms through oxidation of alloyed Al. To be able to reduce the concentration of corundum inclusions in continuously casted steels, it is necessary to know the source of the oxides (i. e. the source of the oxygen in the oxides). Although considerable improvements regarding the steel cleanliness were achieved during the last decades (see Jacobi et al., 1998), the question concerning the origin of the inclusions is still unanswered.

Aim of this study is to resolve the problem of the origin of oxygen in the precipitated alumina by means of oxygen isotope measurements. The model developed will be corroborated by thermodynamic calculations.

1.2 The approach: A stable oxygen isotope study

In this study, a new method for the characterization of oxide precipitates and inclusions in steel is presented. The approach is based on the measurement of the distribution of the

stable oxygen isotopes between oxide inclusions and the possible sources for the oxygen in the oxides. An isotopic characterization is comparable to a chemical characterization. The phases occurring in a system, usually exhibit different but characteristic oxygen isotope ratios. Oxygen occurs in three stable isotopes, namely ^{16}O (99.763%), ^{17}O (0.0375%), and ^{18}O (0.1995%). Since configuration of the electron shell of an atom is essentially unaffected by the number of neutrons in the core, no significant difference in chemical behavior exists between the different isotopes. Differences arise only due to the different masses of the isotopes.

The enrichment or depletion of a sample in ^{18}O relative to a chosen standard is expressed by the δ^{18}O value (Eqn. 1.1). The unit of the δ value is per thousand (‰).

$$\delta^{18}\mathrm{O} = \left(\frac{\frac{^{18}\mathrm{O}}{^{16}\mathrm{O}}\,\mathrm{Sample}}{\frac{^{18}\mathrm{O}}{^{16}\mathrm{O}}\,\mathrm{Reference}} - 1 \right) \times 1000 \tag{1.1}$$

V-SMOW (Vienna standard mean ocean water) is chosen as international reference. V-SMOW has an absolute ^{18}O/^{16}O ratio of 2.0052×10^{-3} (Prosser, 1998). A positive δ^{18}O means that the sample is enriched in ^{18}O relative to the standard, whereas a negative δ^{18}O indicates depletion of the sample relative to SMOW. The variation in δ^{18}O on earth lies between -40‰ (arctic snow) and +40‰ (chert).

In context of this investigation, two different processes are responsible for the variation in δ^{18}O:

- Mass dependent equilibrium fractionations between coexisting phases
- Kinetic partitioning of the oxygen isotopes

Mass dependent fractionation arises as a result of the different bonding energies of ^{16}O and ^{18}O in molecules, amorphous phases or crystals. The degree of partitioning between phases is a function of temperature. With increasing temperature, partitioning approaches zero. Since the pressure effect on the oxygen isotope ratios is negligible (isotope exchange reactions have a $\Delta V_R \approx 0$), oxygen isotopes are used as geothermometers. Kinetic fractionation can be observed as a result of slower exchange of ^{18}O compared to ^{16}O. Hence, during kinetically controlled reactions, a non-equilibrium partitioning of the ^{18}O/^{16}O will occur between educt and product.

Alumina inclusions form through oxidation of alloyed Al at temperatures well above 1500°C. The source for the oxygen is, however, matter of controversal debates. At the ultra-high formation temperatures of the alumina, no or only negligible oxygen isotope fractionation between the oxygen source and the inclusions is expected to occur.

> *Thus, the alumina inclusions and precipitates of inclusions should carry the oxygen signature of their oxygen source*[1].

[1] It is assumed that kinetic fractionation plays no major role

In this study, first data of the oxygen isotope composition of clogging and related possible oxygen sources are presented. Parts of this study were already published (Pack et al., 2000; Pack and Hoernes, 2000a,b).

Samples from two different steel plants (termed A and B) were investigated. A large set of samples from steel plant A were taken during a campaign in the time September/October 1997. Only a few samples of clogging were made available from steel plant B. Raw materials were supplied by R. Broß during this study.

Chapter 2

Steelmaking

2.1 What is a steel?

According to the Verein Deutscher Eisenhüttenleute (1989), a steel is

> *an iron material with aptitude for warm shaping and carbon contents less than 2 wt.%.*

The International Iron and Steel Institute (IISI) defined a steel to be a

> *metal composed of iron plus varying amounts of carbon as well as other elements such as chromium, nickel, molybdenum, zirconium, vanadium, tungsten, and so on.*

Steels are subdivided into two general classes:

1. Alloy Steels
2. Carbon Steels

In alloy steels, the properties of the steel are controlled by the percentage of alloying elements. In carbon steels, carbon is the element that has the greatest influence on the properties of the steel. Stainless steels, for instance, belong to the group of alloying steels. Plate steels used for car bodies, generally belong to the group of carbon steels.

The melts casted during the sampling campaign for this study were low alloyed carbon steels with carbon contents of $<$0.03–0.2 wt.%. The liquidus of a steel melt with 0.2 wt.% carbon is at 1530°C and the solidus at 1493°C (see Hansen, 1958; Fig. 2.1).

2.2 The process

2.2.1 Blast furnace

It is the purpose of a blast furnace to reduce iron oxides (Fe_2O_3 or Fe_3O_4) to liquid iron termed *hot metal*, *raw iron*, or *pig iron*. The blast furnace is a huge, steel stack lined with

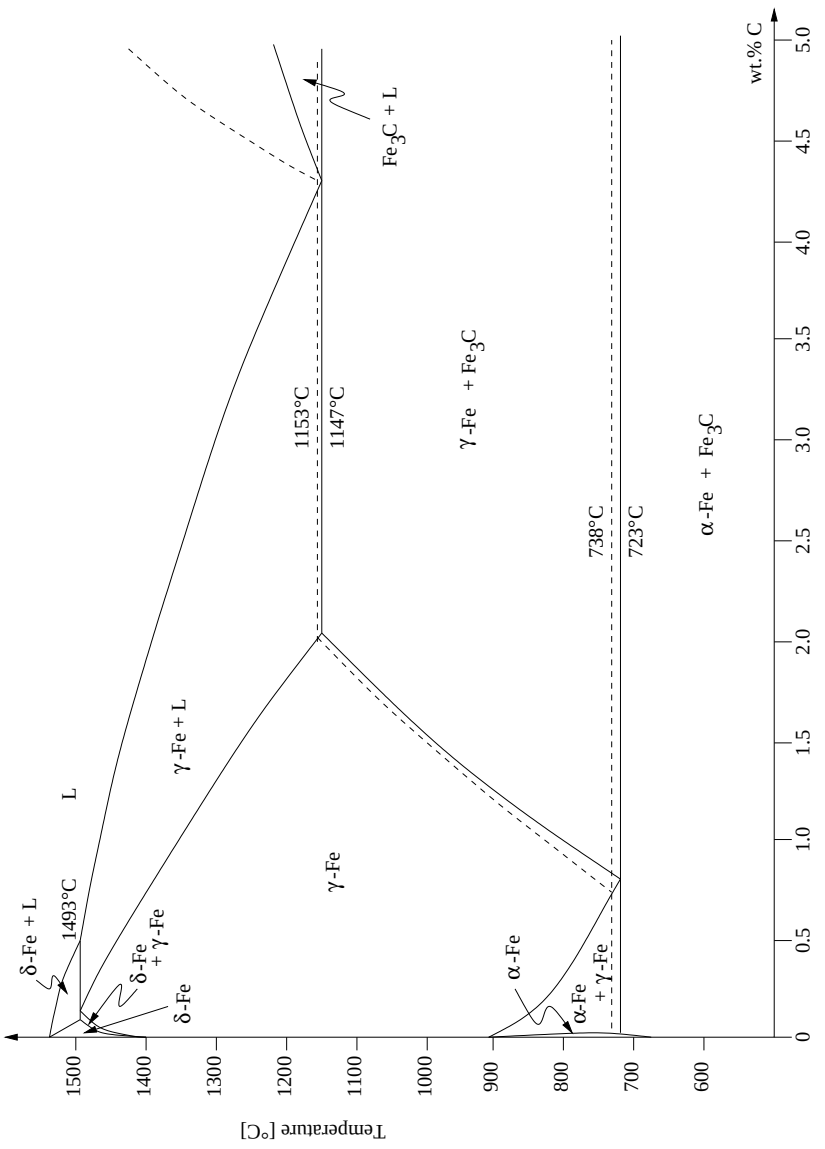

Figure 2.1: Phase diagram of the Fe-rich side of the binary system C-Fe (Hansen, 1958, modified after).

refractories. Iron ore, coke and limestone are dumped into the furnace from the top. To maintain a high temperature inside, preheated air is blown from the bottom upwards into the furnace. It requires 6–8 h for the raw materials (iron ore, coke, and limestone) to descend to the bottom of the furnace where they become the final product of molten slag and raw iron. These liquid products are drained from the furnace at regular intervals. Once a blast furnace is started it will continuously run for several years with only short stops to perform maintenance. A detailed introduction into how a blast furnace works is given in an early overview by Krauss (1902) or more recently by Ricketts (2000).

Coke is used as reducing agent. The coke is produced from a mixture of coals which are crushed, ground into powder, and then charged into an oven. As the oven is heated the coal is cooked so most of the volatile matter such as oil and tar are removed. The following reduction reactions are exited in the blast furnace at the distinct temperature levels:

$$\begin{aligned} 3Fe_2O_3 + CO &\rightleftharpoons CO_2 + 2Fe_3O_4 && \text{begins at } 450°C \\ Fe_3O_4 + CO &\rightleftharpoons CO_2 + 3FeO && \text{begins at } 590°C \\ FeO + CO &\rightleftharpoons CO_2 + Fe && \text{or} \\ FeO + C &\rightleftharpoons CO + Fe && \text{begins at } 700°C \end{aligned}$$

The limestone descends in the blast furnace and reacts to lime (CaO) and carbon dioxide at temperatures of 870°C. The CaO formed from this reaction is used to remove sulfur from the iron which is necessary before the pig iron becomes steel. Sulphur is removed by the reaction:

$$FeS + CaO + C \rightleftharpoons CaS + Fe + CO$$

CaS becomes part of the slag. The slag is also formed from any remaining SiO_2, Al_2O_3, MgO, or CaO that entered with the iron ore, pellets, sinter or coke. The liquid slag then trickles through the coke bed to the bottom of the furnace where it floats on top of the liquid iron since it is less dense. A typical raw iron chemistry is shown in Table 2.1 (data from Ricketts, 2000). The liquidus of a melt of the composition given in Table 2.1 is close to the eutectic temperature of the system γ-Fe–Fe_3C at only 1147°C (see Fig. 2.1).

The carbon rich raw iron is not suitable for applications with advanced quality acceptance criteria. Therefore, most of the raw iron is further processed to steel.

Table 2.1: Typical composition of raw iron as it is produced in a blast furnace from iron oxide ores

Element	wt.%
Fe	93.5–95.0
Si	0.30–0.90
S	0.025–0.050
Mn	0.55–0.75
P	0.03–0.09
Ti	0.02–0.06
C	4.1–4.4

2.2.2 The basic oxygen furnace (BOF, converter)

The major task of the basic oxygen furnace (BOF, also termed *converter*) is, to reduce the carbon content of the raw iron from initially >4 wt.% (Tab. 2.1) to values less than 2 wt.% through formation of CO and CO_2. At carbon contents less than 2 wt.%, no Fe_3C is stable. The iron metal with less than 2 wt.% C is termed *steel*.

The BOF is a pear-shaped furnace, lined with basic refractory bricks, that refines molten iron (pig iron) from the blast furnace and scrap into steel. Up to 30% of the charge into the BOF can be scrap, with hot metal accounting for the rest. A lance is lowered from above, through which blows a high-pressure stream of oxygen to cause chemical reactions that separate impurities as fumes or slag. The concentration of oxygen dissolved in the calcined raw iron is typically in the range of 100–800 ppm (Wijk, 1995).

2.2.3 The ladle

After refining the pig iron in the BOF, the raw steel is poured into the casting ladle which is a cylindrical shaped vessel, containing at steel plant A 190 t melt. A capacity of 190 t corresponds to the capacity of one converter (see Klaassen, 1997).

Initial task of the ladle was to be just a container for the transport of the steel melt from the converter to the casting stand. The steel was casted directly from the ladle into the moulds[1]. Nowadays, the task of the ladle in continuous casting processes is much more multifaceted. It is, of course, still the container for the transport of the heats from the converter to the casting stands. In addition, however, secondary metallurgy for the final adjustment of steel composition is performed in the ladle. Importance of secondary or ladle metallurgy increased with the development of modern high-technology steels. Deoxidation of the steel with reducing agents like Al are performed in the ladle. To remove small oxide particles, argon gas is rinsed through the melt to enforce impurities to be floated up to the ladle slags. Deep desulphurization may also be performed in the ladle. To maintain low sulphur contents (<0.005 wt.%), CaO is added to the slag in excess (i. e. $CaO/Al_2O_3 > 1$). Sulphur is removed from the steel melt by formation of CaS.

Steel bath temperatures in the ladle are in the range of 1570°–1620°C.

2.2.4 The tundish

In continuous casting processes the slabs, blooms, or billets are not casted directly from the ladle. The tundish is interposed as buffer between ladle and casting mould. It is a bath tub shaped vessel and less than half in capacity (≈40 t at steel plant A) than the ladle.

The steel melt flows through shroud tubes into the tundish. The shroud tube protects the melt flow from reoxidation through contact with atmospheric oxygen. Slide gates in the shroud tube control and lock the melt stream. The steel melt surface in the tundish is covered by synthetic tundish slag to avoid reoxidation by air oxygen. Liquid iron with its alloying metals is highly sensitive to reoxidation by atmospheric oxygen.

[1] The ladle thus is also termed casting ladle.

The steel is casted though the submerged entry nozzle (SEN) into the mould. The mould is a rectangular to the bottom open box bordered by cooled copper slabs. The nozzle submerges beneath the mould slag covering the bath level mould. The size of the casting box can be varied in a wide range. At steel plant A, two different sizes of slabs were casted. On three casting stands, two slabs were casted which can be varied in size between 800×220 mm and 1650×320 mm. On the fifth stand a single slab between 1800×220 mm and 2700×320 mm was casted (Gotthelf, 1999).

A thin film of molten mould slag prevents the solidified slab surface from sticking to the cooled copper plates.

The slab leaves the mould in vertical position and is subsequently rolled and bent in the bent device into horizontal position. Depending on the steel plant a rolling mill immediately follows the casting process.

2.2.5 The continuous caster

In modern steel plants, huge amounts of steel have to be casted in a short period of time. Conventional ingot casting is not suitable for the production of huge amounts of standard grade steels. In continuous casting, huge amounts of steel can be casted in a very short time. The steel flux from the ladle into the casting box is buffered by the tundish. Therefore, a single continuous slab can be casted from a whole sequence of ladles. Between 0.6 and 3.5 m slab are casted per minute (Verein Deutscher Eisenhüttenleute, 1989). Figures 2.2 and 2.3 are sketches, illustrating the continuous casting process. An overwiew over the continuous caster instrumentation is published by Ozgu (1996).

2.3 Non-metallic inclusions

Non metallic inclusions which may form in liquid metal at various stages of its elaboration or during its solidification have strong influence on the mechanical, machinability or fatigue properties of the transformed product (see Wintz et al., 1995).

Therefore, the control of non-metallic inclusions is one of the main challenges facing the modern steel makers. For certain applications, however, the presence of non-metallic inclusions may be desired (Wintz et al., 1995). But for most applications, it is important to obtain clean steels.

Non metallic inclusions are divided according to their composition into three groups:

- Oxides
- Sulphides
- Carbonitrides

Oxidic inclusions, on which this study focusses, are subdivided according to their origin into four subgroups:

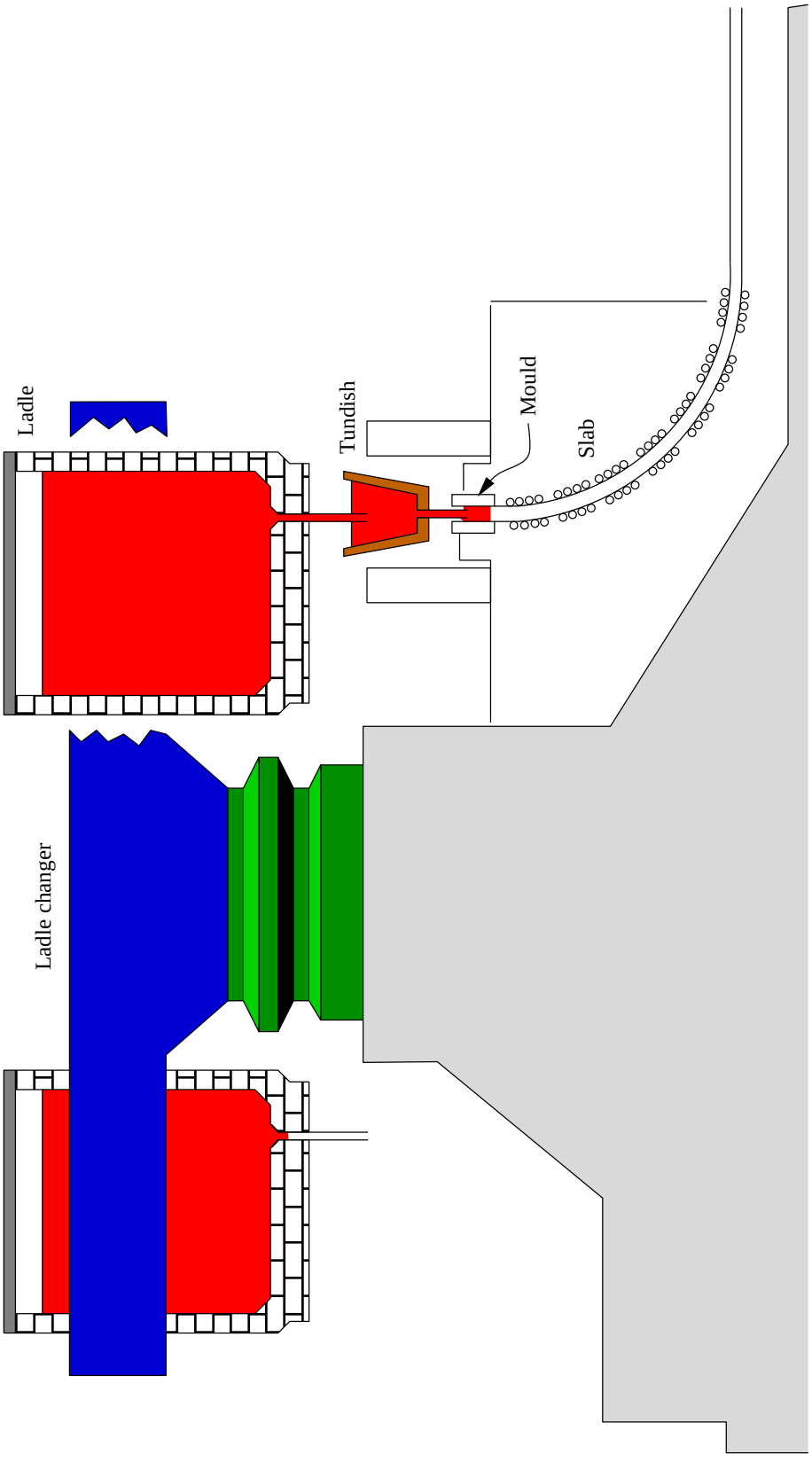

Figure 2.2: Overview illustrating the array of a continuous caster. The melt is casted from the ladle into the tundish and from the tundish into the casting mould. The ladles can be changed during casting without break off. The temperature in the ladle varies in a range of 1550–1650°C. The bath temperature in the tundish is 1545±10°C.

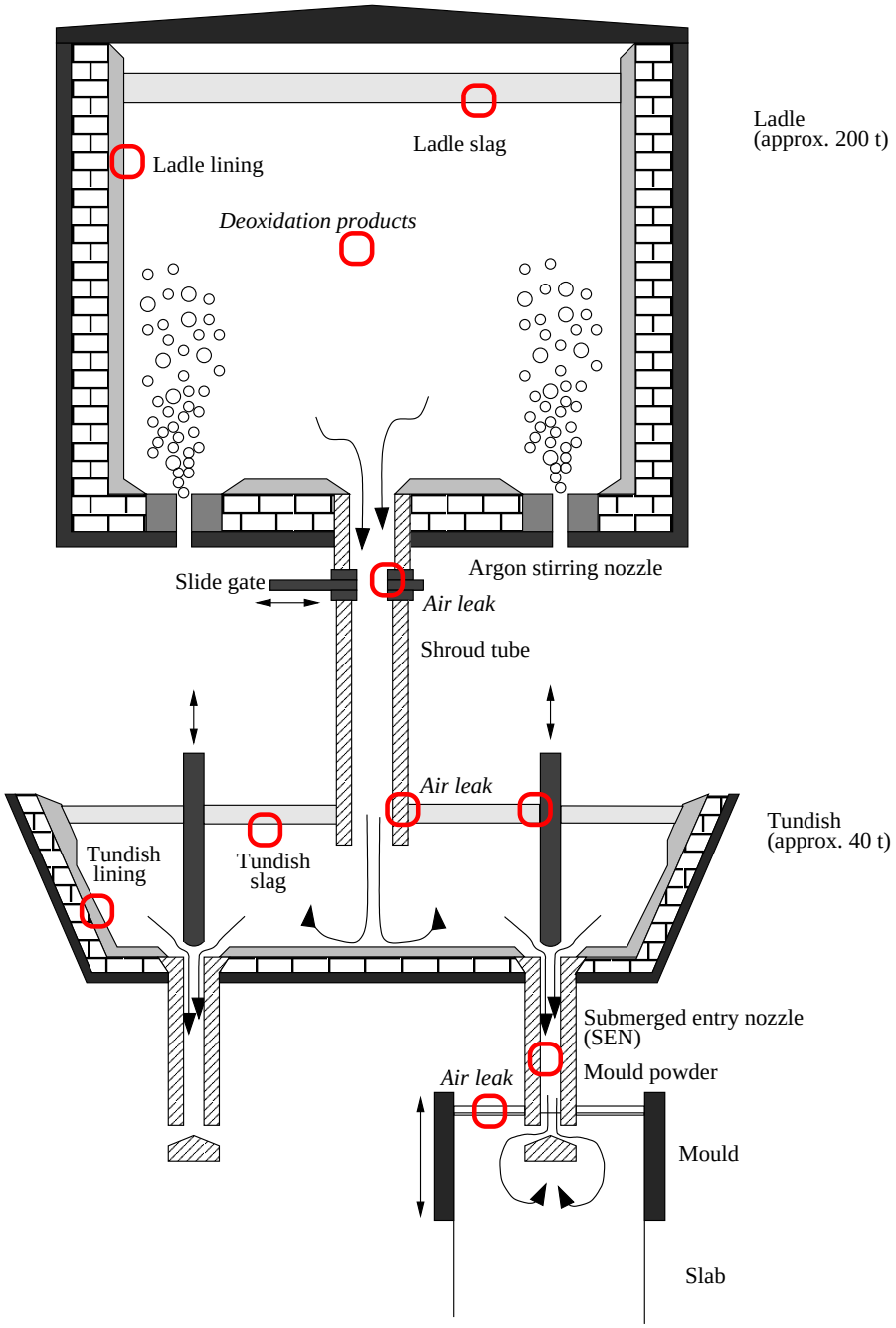

Figure 2.3: Sketch illustrating the array of ladle, tundish, and casting box (mould). Liquid steel, protected by the shroud tube, flows from the ladle into the tundish. The flux is controlled and locked using slide gates. From the tundish, the steel flows through the submerged entry nozzles into the casting mould. Stopper rods control the flux. The circles mark the locations of possible oxygen pick up and formation of non-metallic inclusions.

- Deoxidation products
- Reoxidation products
  - Reoxidation by atmospheric oxygen
  - Reoxidation by reaction with compounds of the refractories
  - Reoxidation by reaction with slags in ladle and tundish
- Eroded refractories
- Slag carry over (ladle, tundish, mould)

Deoxidation products form during steel killing process in the ladle. The oxide particles are small in size and should be absorbed by ladle and tundish slags. The smaller the diameter, however, the slower the particles rise (*Stoke's Law*) (see Gaye et al., 1994; Gotthelf, 1999). Reoxidation products originate from oxidation of melt compounds by atmospheric oxygen, refractory linings or slags. Especially highly lithophile elements like aluminum are quickly oxidized by atmospheric oxygen. Reoxidation may also occur when alloying metals reduce compounds of the refractory linings and slags in ladle or tundish. Erosion of refractory materials may also contribute to formation of non metallic inclusions. Slags may be introduced to the slab especially when bath levels in ladle and tundish decrease towards the casting end. Inclusions can also form *in situ* during solidification of the slab.

A number of techniques is applied to avoid formation and introduction of the inclusions into the slab. The melt in the ladle is stirred with inert argon gas to enforce the absorption of oxides in the ladle slag. It is the task of slags to protect the melt from contact with atmospheric oxygen (Pleschiutschnigg, 1989) and to prevent extensive heat loss (Bednarek, 1995). The shroud tube is used to protect the steel stream from the ladle into the tundish. Many parts of the continuous caster including shroud tubes, stopper rods, and submerged entry nozzles are purged with inert argon gas to prevent contact of the melt with atmospheric oxygen. Shroud tube and submerged entry nozzle are purged with argon to provide a positive pressure and therefor to prevent oxygen entrainment (Bednarek, 1995). The steel flow in the tundish and the casting box is optimized in order to prevent the formation of large deposits and absorption of inclusions in the slag (Huiquing, 1995; Horbach et al., 1995; Sawada et al., 1995; Jacobi et al., 1998). Size distribution and composition of the inclusions are controlled to minimize their detrimental effect on the quality of the final product (*inclusion engineering*, Gaye et al., 1994; Imagumbai and Takeda, 1994; Bednarek, 1995). The refractories are optimized to increase their resistance against attacks of the steel melt (see Bannenberg, 1995).

2.4 Refractories and slags

2.4.1 Ladle

Refractories

A large variety of refractory materials are used in the ladle. At steel plant A, however, only a very small part of the spectrum of ladle in-feeds were in use. Therefore, the description is reduced to the actually used types. The ladle refractory is a composite of two major layers. The permanent lining is approximately 50–120 mm thick. It is overlain by an approximately 200 mm thick layer of a neutral castable or a wall of basic bricks (Klaassen, 1997). The high-alumina monolithic castable is used for the entire ladle lining. The basic lining is built up more complicated. The bottom of the basic ladle is made of high alumina castable. The walls are bricked with a "dolomite"[2] walling and MgO-C bricks protect the slag zone. In steel plant B andalusite refractory bricks and basic bricks were in use.

The linings in teel plant A are to be distinguished into two general groups: Neutral, alumina-rich monolithic castables and basic refractory bricks of the system MgO, CaO, and C. The high-alumina castables are divided in two subgroups:

- High-alumina monolithic castables
  - High-alumina, spinel-forming castable (is also used as lining on the floor of basic ladles)
  - High-alumina bauxite castable
- Basic refractory bricks
  - MgO-C bricks, used in the slag zone
  - CaO-MgO-C bricks, used along the walling

In addition, a basic MgO-rich sprayed refractory is utilized to repair the pitted ladle refractory after use[3].

High-alumina castable Detailed descriptions of composition and corrosion behavior of the high-alumina ladle linings are published in Buhr (1996a,b) and Klaassen (1997). For more details, the reader is referred to this publications. The high-alumina spinel-forming castable is composed of Al_2O_3 and, subordinate, MgO. A representative analysis of the spinel-forming castable is given in Table 2.4.1.

The second type of high alumina ladle refractory used is a bauxite castable. This type is composed of Al_2O_3 with minor amounts of SiO_2 and TiO_2 (Tab. 2.4.1, data from Klaassen, 1997). Enrichment of TiO_2 is typical for bauxite deposits. Schneiderhöhn (1962) reported a typical concentration of TiO_2 in bauxite deposits of 4 wt.%.

[2] Dolomite is a common term for a material produced by calcination of dolomite. It is actually composed of CaO and MgO and not of dolomite ($CaMg[CO_3]_2$).

[3] Ladle are used up to >100 times (Buhr and Koltermann, 1996)

[1.5ex]

Table 2.2: Major and minor element composition of two different types of neutral ladle linings. The data are reported in wt.%.

Type	SiO_2	Al_2O_3	TiO_2	Fe*	CaO	MgO	Na_2O	K_2O	P_2O_5
SP	1.46	92.32	0.03	0.14	0.90	4.64	0.27	0.02	0.11
BAUX	8.09	85.37	3.15	1.39	1.01	0.21	0.10	0.18	0.36

Abbreviations: *SP* spinel-forming castable, *BAUX* bauxite castable
Fe* denotes $Fe + Fe^{2+} + Fe^{3+}$

Both types of ladle lining were used during the sampling campaign. For further reading, the reader is referred to Klaassen (1997); Buhr (1996a,b); Buhr and Koltermann (1996).

Basic refractory bricks The refractory bricks used at steel plant A are carbon bond CaO-MgO and MgO bricks, respectively. These materials are used in ladles, where deep desulphurization is performed.

Ladle slag

The composition of the ladle slag is carefully controlled during the steel refinement process. It is the task of the ladle slag to absorb oxide inclusions, to bind sulphur, to protect the melt from contact with the atmospheren and from heat loss. The slag should be liquid but should not react with the ladle lining. Slags that fulfill these requirements are composed of two major components: Al_2O_3 and CaO. Depending on the steel quality and on the refractory used in the ladle, two types of ladle slag are used:

- Dark colored slag which is used in neutral lined ladles, $CaO/Al_2O_3 = 1$
- White, highly reduced slag which is used in basic ladles, $CaO/Al_2O_3 > 1$

The ladle slag is composed of a mixture of different sources. A part is slag which is carried over from the basic oxygen furnace to the ladle. Slag of the converter contributes varying amounts of CaO, SiO_2, FeO, and MnO to the ladle slag. Alumina in the ladle slag may originate from floated deoxidation particles. MgO contents in the ladle slag (up to 25 wt.%) is contributed by erosion of refractories in the ladle (basic repair lining). Finally, lime and alumina are added to the ladle slag to adjust the desired CaO/Al_2O_3 ratio. An excess of lime in the ladle slag is required when deep desulphurization is performed ($S < 0.005$ wt.%, Trojer et al., 1981). CaF_2 is added as flux in slags with $CaO/Al_2O_3 > 1$ to avoid solidification.

The average composition of slag used in neutral and basic ladles is given in Klaassen (1997) (Tab. 2.3 and by Buhr (2000, pers. comm.). Notable are differences in the amounts of Fe and MnO which are mirrored in the color of the slag. Low Fe and Mn contents are due to highly reducing conditions which form a necessary condition for deep desulphurization. Slag with excess in CaO (i. e. $CaO/Al_2O_3 > 1$) is used exclusively in basic lined ladles (see also Trojer et al., 1981, p. 131).

Table 2.3: Average composition of slag used in neutral lined ladles (data from [1] Klaassen, 1997, Buhr 2000, pers. comm.) and this study. Notable are differences in Fe and MnO content and the lime to alumina ratio. Lime in excess is required for deep desulphurization (data are reported in wt.%).

	Neutral lining		Basic lining
	[1]	[2]	[this study]
CaO	43	40	53
Al_2O_3	40	40–45	26
SiO_2	5	5	7
Fe*	3	4	0.5
MnO	4	1–2	0.08
MgO	5	5	10
CaO/Al_2O_3	≈1	≈1	≈2

Fe* denotes $Fe + Fe^{2+} + Fe^{3+}$

2.4.2 Refractories and slags used in the tundish

2.4.3 Basic tundish lining

To protect the 200 mm thick permanent tundish refractory from corrosion, an approximately 30 mm thick layer of the basic tundish lining is sprayed onto the permanent castable (Berger et al., 1989; von Witzleben et al., 1996). The layer is thickened in its the upper part, where slag attacks the tundish lining. Figure 2.4 illustrates the cross section through the wall of a tundish. The temperature gradient in the sprayed tundish lining is as high as 350°C/30 mm (12 K/mm, von Witzleben et al., 1996).

The permanent castable is composed of Al_2O_3 and SiO_2 (andalusite castable) and is made to be used several hundreds of times (von Witzleben et al., 1996). The sprayed tundish lining is composed of MgO and SiO_2 (periclase and olivine) and is disposed together with steel and slag rests after use. It is desired that the basic tundish lining fulfills a number of different conditions:

- Resistant against liquid steel (i. e. high solidus temperature)
- Resistant against tundish slag
- Low heat conductivity (i. e. good isolation properties)
- Stable (i. e. no erosion of refractory during casting)
- High resistance to thermal shock
- Chemically inert with respect to the heat and the permanent castable
- Sprayable
- Must be disposable after use
- Reasonable in price

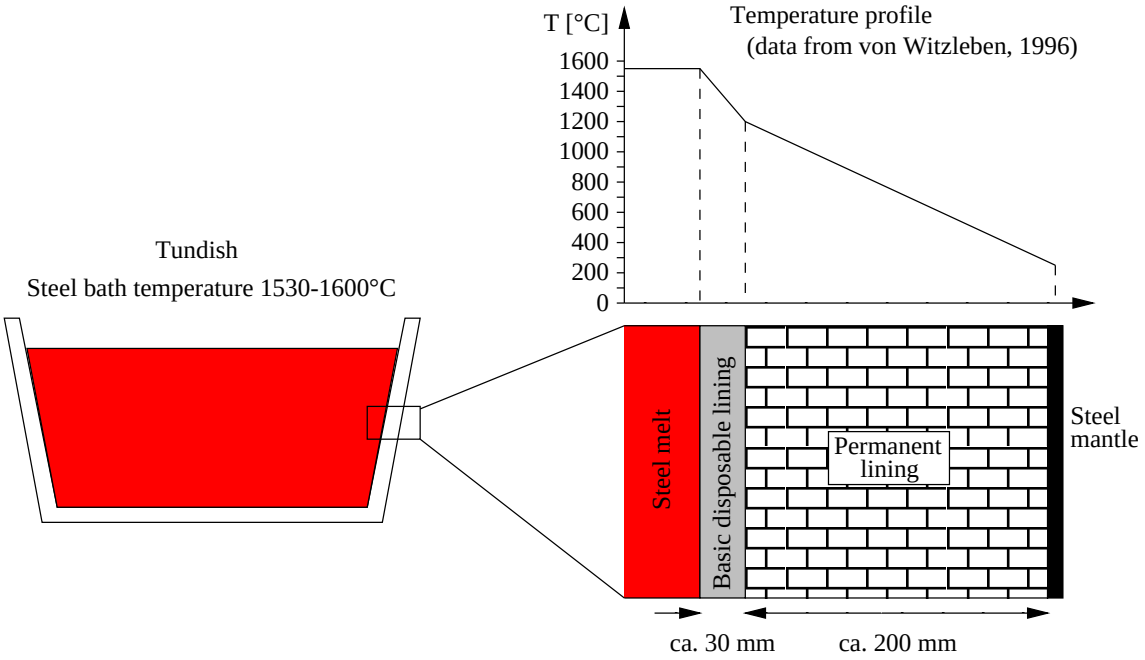

Figure 2.4: Sketch of a cross section through the wall of the tundish. An approximately 30 mm thick disposable lining protects the 200 mm thick permanent castable from heat and corrosion. A temperature profile is plotted to the top. Note the high temperature gradient of 350°C/30 mm in the disposable tundish lining (data from von Witzleben et al., 1996).

A high solidus temperature is ensured by using refractory materials like periclase and forsterite in the proportions 2/3 to 1/3, respectively. The resistance against aggressive slags is always a problem which is solved by thickening the lining in the slag zone. The high open porosity of up to 50 vol.% (Broß, 1999, pers. comm.) guarantees a low heat conductivity and, consequently, good isolation properties. Inorganic binders are used to stabilize the lining at high temperatures. The thermal shock resistance of periclase is relatively low. Therefore, and for the purpose of drying[4], the tundish lining is pre-heated to temperatures of up to 1250°C prior to being exposed the lining to liquid steel. Gas burners are used for heating.

Tundish slag

The raw material of the tundish slag is the ash of burned rice paring. This by-product of rice production contains SiO_2 and a few per cent carbon. The task of the tundish slag is to protect the steel melt from contact with atmospheric oxygen. Assimilation of components of the melt, the tundish lining, and slag carried over from the ladle results in the formation of a liquid silicate melt film on top of the melt.

[4] A high vapor pressure in the lining leads to hydrogen pick up of the melt.

Chapter 3

Sampling

3.1 General

A sampling campaign was undertaken a stay at the steel plant A in September/October 1997. A large set of samples was taken from tundish refractories, slags and from used submerged entry nozzles. Precipitates of oxide inclusions existed in all samples of the submerged entry nozzles. They occurred as crusts along the inner walls of the SEN and along the bottom side. These precipitates (termed *clogging*) are inferred to be identical in composition compared with inclusions dispersed the steel slab. Inclusions which form during solidification of the slab, however, are absent in the SEN precipitates. Only a small, and most probably not representative set of samples of ladle refractories and ladle slag was taken.

Hand specimens were taken from ladle, tundish and submerged entry nozzles (SEN). Chemical analyses of selected steel melts were kindly made available by steel plant A. The emphasis of sampling for this study was clearly clogging material of the submerged entry nozzle and on refractories and slags of the tundish. Samples of the raw materials used used for the sprayed basic tundish lining were made available by R. Broß.

Samples of various raw materials, especially periclase, used in steel making processes have been provided by R. Broß. These samples were analyzed in order to get an idea about the isotope composition of refractories in general.

From a second steel plant (steel plant B), only a very restricted set of samples was studied. These samples were not collected by the author but were sent to him by mail. Three samples of different andalusite refractory bricks, which were used in steel plant B, are available and were investigated. Basic linings, which were also used in steel plant B were not sampled, neither were samples of ladle slag available. The tundish used in steel plant A and B were lined and covered with exactly the same refractory linings and slags, respectively. Therefore, the result of the study of the tundish system apply to steel plant B. The melts casted in both steel plants were similar in composition. In both cases, low alloyed, Al-killed steels were continuously casted. The Al-content in plant B varied between 0.04 and 0.05 wt.%.

The list of samples with a brief description is in given the appendix (page 136ff).

3.2 Classification

The samples were classified into the following groups

- Ladle slag
- Ladle refractory
- Sprayed tundish lining
- Tundish slag
- Submerged entry nozzle (SEN)
- Clogging along the inner walls of the SEN
- Clogging along the bottom side of the SEN

3.2.1 Steel plant A

Ladle refractories

During the sampling campaign, only a very limited set of hand specimens of the ladle refractories could be collected. Since the lining in the ladle is used for up to 100 heats, it usually remains in the ladle. However, a few samples could be taken from the ladle. Two samples of neutral, high-alumina castables were taken. The specimens of the neutral, high-alumina castable are white with sometimes dark veinlet of penetrating slag. The degree of ladle slag reduction is less than in neutral lined ladles. The slag in neutral ladles is dark in color due to minor amounts of Fe and Mn. In addition, two samples of basic MgO-C bricks were sampled from a basic lined ladle. These bricks are composed of white to beige colored, millimeter-sized angular periclase aggregates embedded in a fine-grained black matrix composed of graphite.

Ladle slag

Samples of the ladle slag were taken using a steel lance which was lowered into the liquid slag during the steel refinement process. The slag was accessible through a small window in the lid of the ladle. Two different types of ladle slags were used during the sampling campaign depending on the ladle refractory lining

- White Mn- and Fe-poor slag used in basic lined ladles
- Dark colored, Mn- and Fe-rich slag used in neutral lined ladles

During the sampling campaign at steel plant A, only white slag was directly sampled from the top of the ladle. Samples of dark Mn-rich slag adhered to the neutral refractory concrete sampled from the ladle (Samples 76a and 101).

The white slag differed considerably in viscosity from sample to sample. Slags with low viscosity solidified as greenish glass on the steel lance, whereas highly viscous slags adhered as fine-grained white aggregates which immediately disintegrated to powder when cooled down. All ladle slag samples taken had in common a strong smell after H_2S, mirrored, in SO_3 contents up to 3 wt.%. This is expected since this CaO-rich type of slag is utilized for deep desulphurization.

Tundish slag

During casting, the bottom side of the tundish slag melts and thus protects the steel melt from the atmosphere, whereas the top of the slag remains cooler and unmolten. Samples of the tundish slag were taken from the tundish after casting had ended.

The slag solidified to a glass dark green to black in color with schlieren texture. Its texture is sometimes very porous (spongy) with millimeter sized isolated pores.

Sprayed tundish lining

Like the samples of the tundish slag, also those of the sprayed tundish lining were taken from the tundish after casting had ended. The samples are brownish beige in color and were easily accessible. When collected, the temperature of the samples was estimated to be still in the range of 100–200°C.

Alteration of the lining increased visibly towards the melt interface. The color changed from initially beige to colorless gray at the steel melt contact. The porosity decreases with increasing degree of alteration. Most samples of the tundish refractory were coated by a thin film of glassy tundish slag. The side of the tundish slag facing the permanent refractory lining did not show any signatures of alteration. The contact between the altered and unaltered part of the tundish lining was sharply developed and did not extend to more than a few millimeters.

SEN clogging

After lifting the tundish from the casting stand by a crane, the still red glowing SENs were immediately detached. Most of the SENs were smashed and samples of oxide deposits were taken from the inner walls and the bottom side of the SEN. The deposits along the inner part and the bottom side of the SEN were very fine grained and white to gray in color. Some samples exhibit a yellowish complexion, most probably due to secondary oxidation of iron. The deposits along the inner walls are generally thin, gray in color and rich in iron which occurs as tiny steel gray droplets. Up to 100 mm thick deposits occurred at the bottom end of the SEN in the melt impact zone (Fig. 3.1).

The clogging at the bottom side of the SEN is thin ($<$10 mm) and appears to be systematically zoned. The melt contact is constituted of very fine grained friable white alumina. The SEN contact is brownish colored due to amounts of ferric iron oxide.

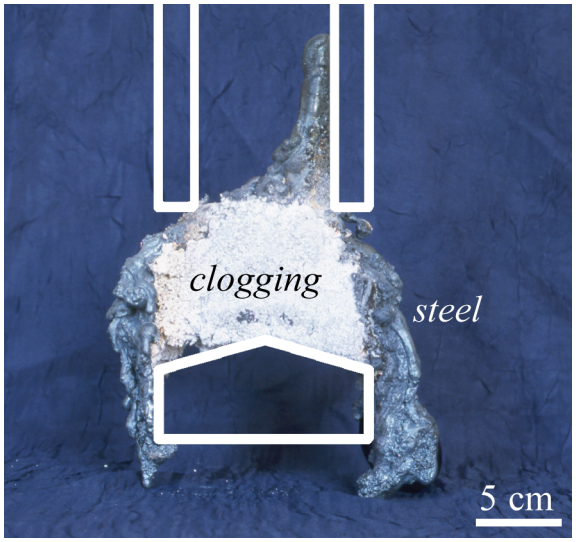

Figure 3.1: Thick white oxide deposit in the inner of the SEN. The shape of the SEN is outlined (Sample 63).

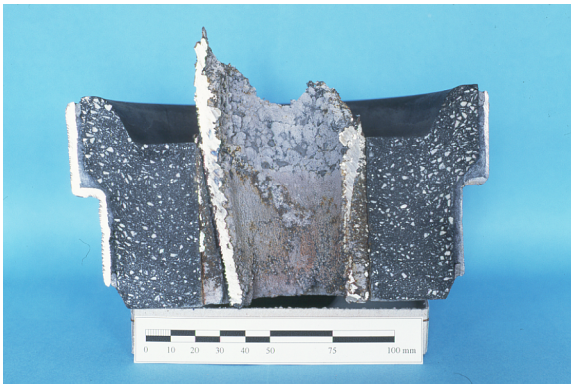

Figure 3.2: Cut through the upper part of a SEN (Sample 01). The SEN material is composed of white alumina- and SiC-grains embedded in a black C-rich matrix. Steel and thin oxide deposits occur adjacent to the inner walls.

The clogging is friable and porous and can easily be scrapped off. To study the texture of the clogging and the contact between the SEN and the oxide deposits, however, only bulk samples including parts of the adjacent SEN material were taken.

Submerged entry nozzle

The SENs are black in color and are composed of corundum, graphite and SiC (Fig. 3.2). SiC is added to the material to act as oxygen blocker through formation of silica. A ZrO_2 outer ring at bath level is used to protect the SEN from attack of the mould slag.

3.2.2 Steel plant B

Clogging

Seven samples of clogging from steel plant B were available. The samples resemble macroscopically the samples from steel plant A. The material is white to gray in color, fine-grained, and friable. Steel droplets were adjacent to the oxides.

Andalusite bricks

The andalusite bricks are white to beige in color. In two samples, reddish brown spots of iron oxide occur. The texture is homogeneous and fine-grained. Macroscopically no mineral

phases can be distinguished.

Chapter 4

Analytical Methods

4.1 Experimental section

4.1.1 Laser fluorination

Introduction

To obtain the oxygen isotope compositions from samples including the corundum-rich SEN precipitates, IR-laser fluorination *irm*MS was applied (see Sharp, 1990). Conventional fluorination is not suitable to analyze the alumina-rich samples because of the low yields during fluorination at temperatures of 600–700°C.

Sample preparation

The samples were ground to powder and mixed 1:1 with LiF. The LiF serves as moderator of the violent reaction between alumina and fluorine gas through formation of a LiF melt. Samples of the refractories were treated the same way as the alumina-rich clogging samples with the exception that they were mixed with less LiF (≈1:2). Using a 2 mm piston cylinder apparatus, small pellets are pressed from this powder. Aliquots corresponding to ≈1 mg oxide sample are loaded into the grooves of the Ni sample holder. Most samples were analyzed twice to exclude analytical errors. 19 samples can be loaded each. To remove any moisture, the sample holder is put into an oven over night at 110°C. In addition, all samples were prefluorinated at a pressure of approximately 8 mbar over night to ensure the entire removal of superficial impurities.

Instrumentation

The laser-fluorination line at the Department of Mineralogy in Bonn was set up by S. Hoernes in 1992 in collaboration with U. Lichtenstein shortly after the first publication of Sharp on the infrared laser-fluorination technique in 1990. Since that time many modifications were made on this line which shall not all be described here in detail. Regarding the earlier setup of the laser line, the reader is referred to the PhD-thesis of (Hagen, 2000).

In 1997 the line was connected to a new mass spectrometer, a *PDZ-Europa 20-20* triple collector gas mass spectrometer. The mass spectrometer is run in continuous flow mode and is equipped with a differential pumping system. Although using a new mass spectrometer, both precision and accuracy were still not satisfactory. Essentially vacuum problems lead 1998 to the decision to rebuild the whole laser line using stainless steel instead of glass parts. Materials of choice were electro polished 1/4" and 3/8" stainless steel tubings (*Dockweiler*) and stainless steel capillary tubings. Exclusively *Nupro* high vacuum bellow and membrane valves were used to maintain the vacuum in the range of 3–10$\times 10^{-6}$ mbar. Vacuum tight *Swagelock* stainless steel tube fittings were used.

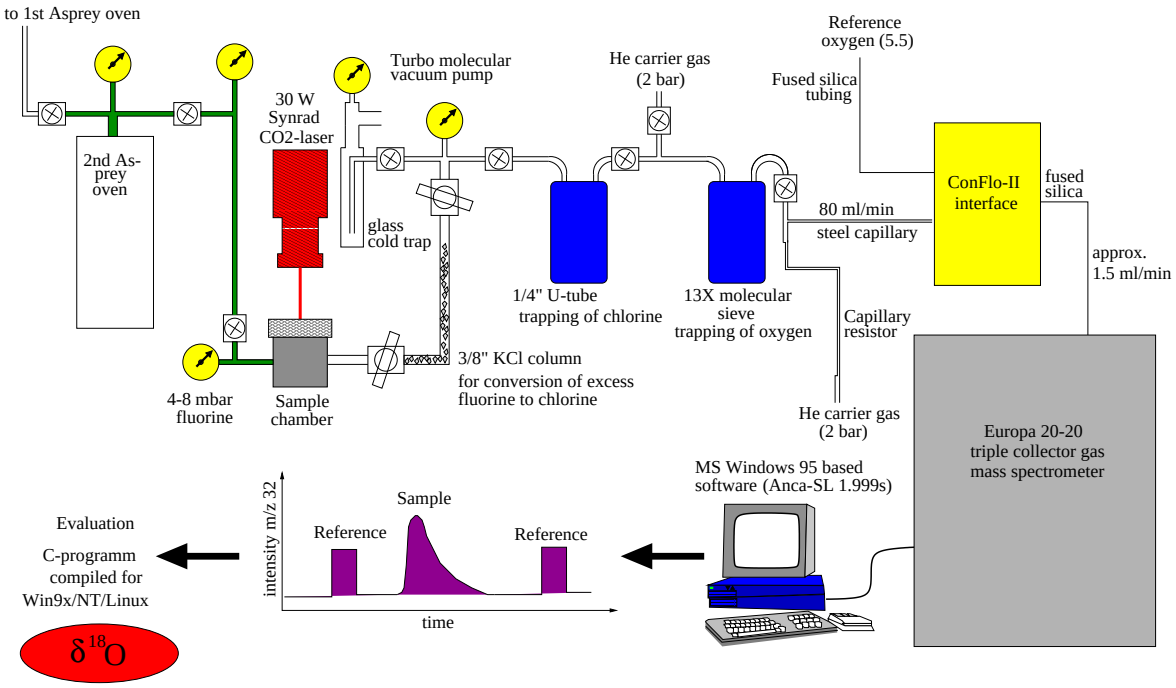

Figure 4.1: Sketch illustrating the set up of the IR-laser fluorination line at the Department of Mineralogy in Bonn. A maximum of 3 bar purified fluorine is produced in an Asprey oven. 1 bar of the fluorine is expanded to a ≈30 cm long 1/4" tube reservoir which acts as reservoir during the laboratory day. 3–8 mbar are expanded to the sample chamber where samples are melted and vaporized using a *Synrad* 30 W CO_2-laser. To remove excess fluorine from the sample oxygen, the gas mixture is led through a heated (90–110°C) KCl fluorine gatter. Chlorine is removed in a U-tube cold trap (-196°C). Sample oxygen is collected on 13$\times$ molecular sieve pellets in a second trap operated at temperature of liquid nitrogen. Oxygen is liberated from the sieve through heating and is flushed with He via a *Finnigan ConFlo-II* EA-MS interface into the source of an *PDZ-Europa 20-20* triple collector gas mass spectrometer. Laboratory oxygen reference gas is injected from a bottle into the open split of the *Con-Flo II* interface. Data evaluation is performed from the raw data using a self written software program.

Reaction chamber The cylindric reaction chamber is cut of a single block of 316 stainless steel. Its dimensions are 40 mm in diameter and 40 mm in height. The chamber is covered by an IR-transparent, polycrystalline ZnSe window (Ø = 50 mm, d = 5 mm) supplied by *Crystal GmbH, Berlin*. Alternatively, BaF_2 single crystal windows of the same diameter can be used. However, the laser energy is then reduced to 40% of the total energy. Increase in energy to more than 40% of the total energy immediately leads to cracking of the BaF_2 window. A further disadvantage of the BaF_2 windows was the very well developed cleavage which makes them very sensitive to breaking. A *Kel-F* O-ring seals the chamber vacuum tight. The ZnSe windows have to be polished from time to time to remove turbid reaction products from the surface which is exposed to fluorine.

Asprey oven An *Asprey* oven (see Asprey, 1976) is utilized to produce 1–3 bar of purified fluorine[1] at the beginning of each laboratory day. 1 bar of that fluorine is then expanded to a ≈30 cm long 1/4" tubing which acts as fluorine reservoir during the day. 4–8 mbar fluorine per sample and blank are expanded from that reservoir to the reaction chamber. To remove any traces of moisture or other impurities from the sample surface, the chamber was pre-fluorinated over night at a pressure of 4–8 mbar fluorine prior to sample analysis.

Fluorine gatter Task of the KCl column is to remove excess fluorine ($2KCl + F_2 \rightleftharpoons 2KF + Cl_2$). The KCl column is made of Ni and is maintained at a temperature between 90° and 110°C, respectively. The fine-grained, analytical grade KCl has to be melted and recrystallized (Ø ≈ 0.2–1 mm) prior to using it in the column. Fine-grained salt is not suitable for this purpose.

Cl_2 cold trap The chlorine released in the KCl-column from the conversion of excess fluorine to KF is removed from sample oxygen in a 1/4" U-tube kept at temperatures of liquid nitrogen[2]. The trap is filled with a *monel* net to enforce the Cl_2 removal through enlarging the active surface. Adsorption of oxygen on cooled metal surfaces at temperatures of liquid nitrogen was observed by Przybilla (1999, pers. comm.). This observation could not be confirmed in experiments conducted recently by Hoffbauer and Hoernes (2000, pers. comm.). Relatively large amounts of sample oxygen may, however, mask adsorption of a small fraction of oxygen in the cold trap.

Molecular sieve trap Sample oxygen is collected on 25–30 cooled (-196°C) 1/16" pellets of 13× molecular sieve. Alternatively, 5Å molecular sieve pellets and silica gel was used with similar results in terms of trapping time and adsorption efficency. Desorption of the oxygen is conducted at temperatures well above 100°C using hot water and a hot air gun.

Miller et al. (1999) report that heating of the 13× sieve to only 50°C is sufficient to liberate the entire oxygen gas but to keep NF_3 trapped. Hoernes (1999, pers. comm.) could

[1] The fluorine produced in the Asprey oven is purified in a first oven of this type in the conventional fluorination laboratory next door to the laser laboratory where also the fluorine bottle is stored.

[2] The freezing point of chlorine is at -102°C.

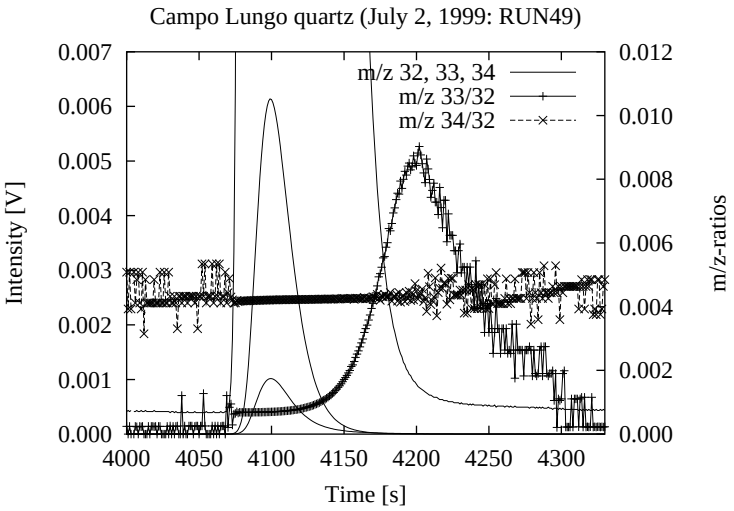

Figure 4.2: Plot of the intensities of the m/z 32, 33, and 34 and of the ratios 33/32 and 34/32 vs. time. Note the dramatic increase of the 33/32 ratio after the main oxygen signal. This increase is due to release of NF_3 from the molecular sieve.

confirm the separation of oxygen and NF_3 through heating of the molecular sieve in two steps.

Traces of NF_3 produce unrealistic high ^{17}O values typically being in the range of the ^{18}O signal, but sometimes even higher due to overlapping of the $^{33}O_2$ with the signal of the ^{33}NF molecule. Bombardment of NF_3 in the ion source of the mass spectrometer produces the ^{33}NF molecule.

The NF_3 is released later from the sieve than the sample oxygen, as shown in Figure 4.2. A characteristic increase of the ratio m/z 33/32 which is a measure for the amount of $^{33}O_2$ and ^{33}NF relative to $^{32}O_2$ can be observed after the main oxygen signal. Miller et al. (1999) have recently shown that this effect can potentially be used to separate NF_3 from the sample oxygen in laser-fluorination techniques.

In this study, only the $\delta^{18}O$ values are of interest and thus no attention was given to remove NF_3 in order to obtain accurate data of $\delta^{17}O$.

ConFlo-II interface The built in split valve of the *PDZ Europa 20-20* mass spectrometer was disconnected and, instead, a *Finnigan MAT ConFlo-II*[3] elemental analyzer to mass spectrometer interface was used. The interface allows to inject reference gas directly from a bottle of gas into the He carrier gas flow. The pressure in the open split valve is buffered by the atmosphere to ≈1 bar. Sample and reference oxygen entrapped in He is injected into the source of the mass spectrometer via a 0.075×1500 mm deactivated fused silica capillary tubing. Reference oxygen pressure is adjusted to approximately 1.5 bar and is injected through a 0.075×300 mm fused silica capillary into the open split (see Fig. 4.3).

The use of the ConFlo-II instead of the built in split valve allows to measure the reference oxygen between each of the sample measurements. This way the drift of the mass spectrometer can exactly be monitored and, if necessary, be corrected. Typically, the reference gas is measured three times per sample, twice before and once after the sample oxygen (Fig. 4.4).

[3]The interface was kindly made available by Professor J. Hoefs, Göttingen.

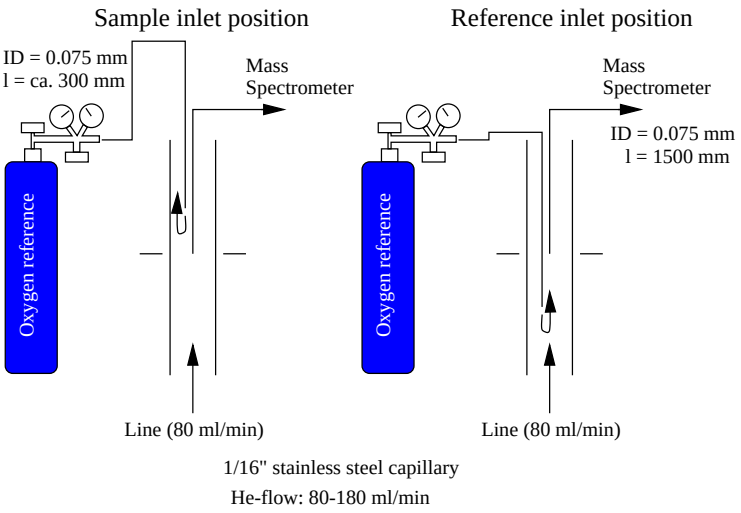

Figure 4.3: Sketch illustrating the principle of the open split valve as it is built in the *Finnigan ConFlo-II* interface (*Left*: Sample inlet position, *Right*: Reference gas inlet position). 80 ml/min He from the line enters the open split. One fused silica capillary which is connected with the ion source of the mass spectrometer permanently dips from the top into the He. A second capillary with reference gas can be lowered into the open split so that reference gas can enter the mass spectrometer.

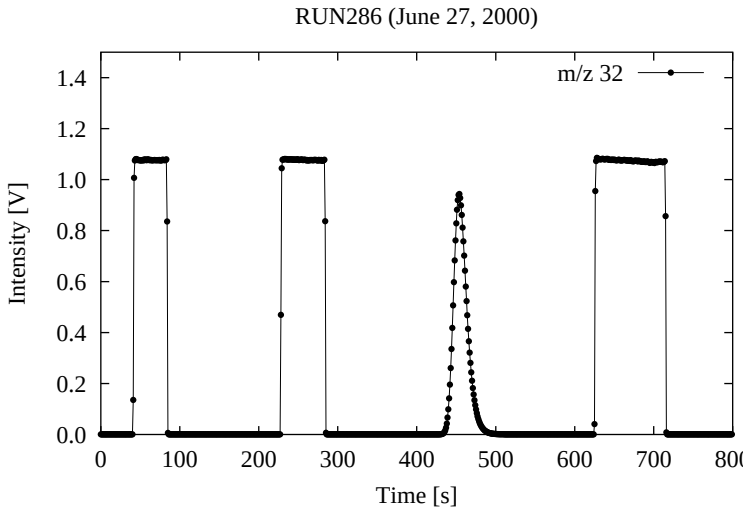

Figure 4.4: Plot of the intensity of the m/z 32 signal vs. time. Typically, two reference gas measurements are performed before and one after each sample. The reference gas peaks are cognizable on their rectangular shape in contrast to the smooth sample gas peaks.

Mass Spectrometer Isotopic abundances in O_2 as analyte are measured using a *PDZ Europa 20-20* triple collector isotope ratio mass spectrometer with 120° ion optics and 110 mm radius. The collectors are fixed Faraday cups connected to feedback resistors and could not individually be adjusted. The analyte is entrapped in a He carrier gas stream coming directly from the *ConFlo-II* open split valve into the ion source.

All settings of the mass spectrometer are controlled using the *Anca NT* MS Windows based software (Fig. 4.5). The ion source is maintained at a pressure of $2.0–3.6\times10^{-6}$ mbar whereas the analyzer region is pumped down to 1.7×10^{-7} mbar. Accelerating potential is adjusted at the beginning of each laboratory day by monitoring the ion currents and ion current ratios to a value in the range of 3.6 kV (Fig. 4.5). Trap currents are set to 400 μA and the ion repeller tension to -6.5 V. O_2^- ions are generated by electron impact (40–50 eV). Three ion currents are simultaneously monitored by the Faraday cups connected to feedback electrometers. The feedback resistors are nominally 100 MΩ (m/z 32) and 5000 MΩ (m/z 33 and m/z 34). A 1×10^{-8} A (10 nA) current at m/z 32 therefore produces a 1 V signal. Sample and reference gas are injected directly into the ion source via a fused silica tubing.

To avoid shifts in resistance, the feedback resistors are kept at constant temperature[4] by a self constructed, isolated 5 W heater placed around the detector unit. Integration intervals are set to 1 s[5] with an internal counting rate being in the range of ms (Park, 2000, pers. comm.). Electrometer offsets are automatically set.

Mass spectrometer drift To check the constancy of the mass spectrometer over a time interval, bottle oxygen (>2 bar) was introduced via a 1/4" union-T into the streaming He carrier gas flow. A bellow valve was used to adjust the intensity of the oxygen signal. The flow was assumed to be viscous, i. e. without causing any isotope fractionation. It has to be noted here that this experiment was conducted before the *ConFlo-II* interface was available. Instead of the construction with the valve and the union-T, nowdays the *ConFlo-II* would be used to determine the drift of the mass spectrometer device.

An opposite drift of the $\delta^{17}O$ and the $\delta^{18}O$ value was observed over a time span of two hours (Fig. 4.6). $\delta^{17}O$ shifted towards higher values, whereas $\delta^{18}O$ decreased during the time of monitoring. The opposite shift in $\delta^{17}O$ and $\delta^{18}O$ shows evidently that the observed shift is caused by the mass spectrometer device and not by a change in the isotopic composition of the gas introduced. In latter case, both, $\delta^{17}O$ and $\delta^{18}O$ should drift in the same direction with $\delta^{17}O = 0.5 \times \delta^{18}O$.

Using the *Con-Flo II* interface, the batch length for individual samples is in the range of 15 min (see Fig. 4.4). No or only little drift correction has to be performed for such short time spans. Figure 4.6 shows that drift correction is necessary if batches more than one hour in length are measured. In such cases, drift correction is performed using a linear regression function.

[4]The temperature is maintained a few degree above laboratory temperature with a precision better than ±0.1°C. A proper air condition for the whole laboratory would do the same job and, furthermore, would chill down the laboratory worker himself during hot summer afternoons.

[5]Though the *Anca-NT* 1.999 software offers to choose between 0.1 and 1 s, respectively, in both cases the integration interval is 1 s.

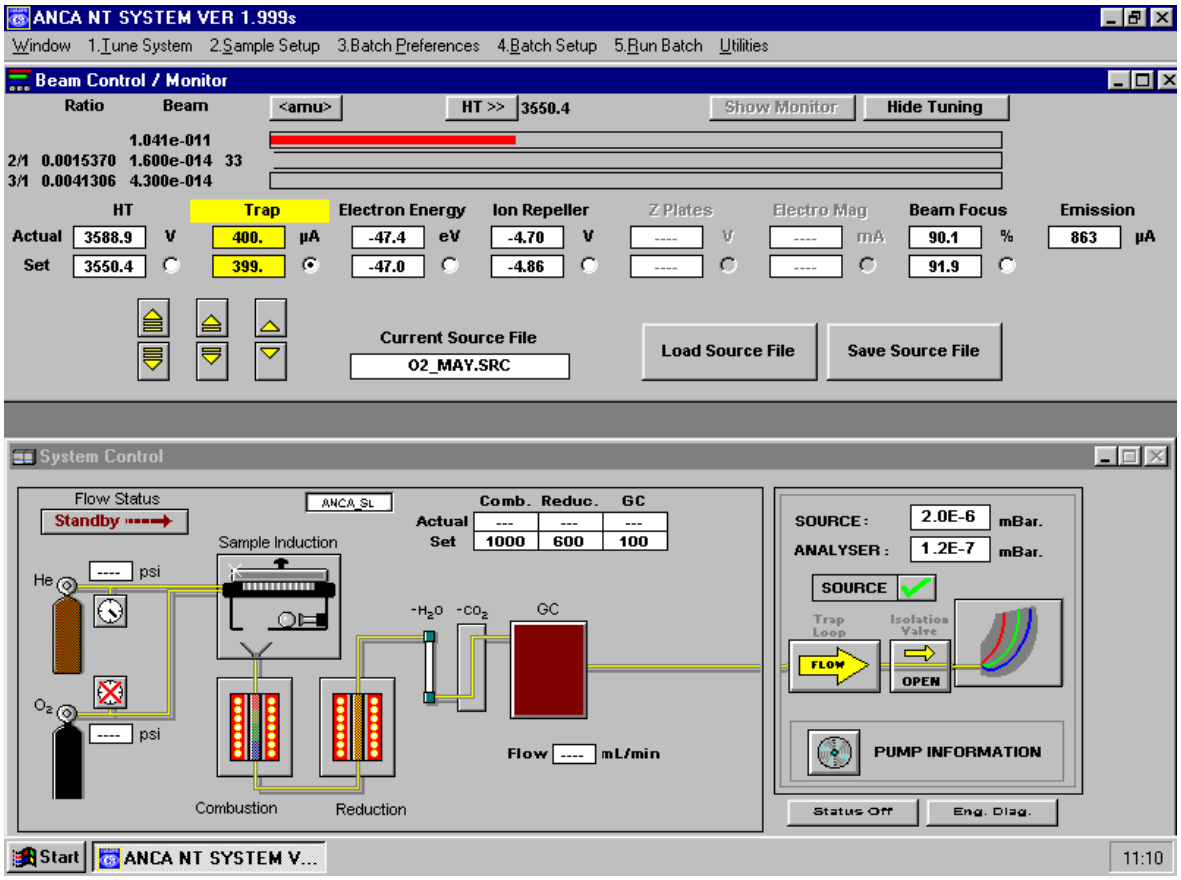

Figure 4.5: Screenshot of the *Anca NT* (vs. 1.999s) main window showing the settings of the mass spectrometer. The section to the top shows the acceleration voltage, trap current, electron energy, ion repeller tension, beam focus, and the emission current. The three bars to the top display the signals on the three detector cups. The bottom left section belongs to the elemental analyzer which is not connected to the laser system and thus is deactivated. The bottom right section is the source control window. The source is pumped down do 2×10^{-6} mbar and the analyzer region to 1.2×10^{-7} mbar.

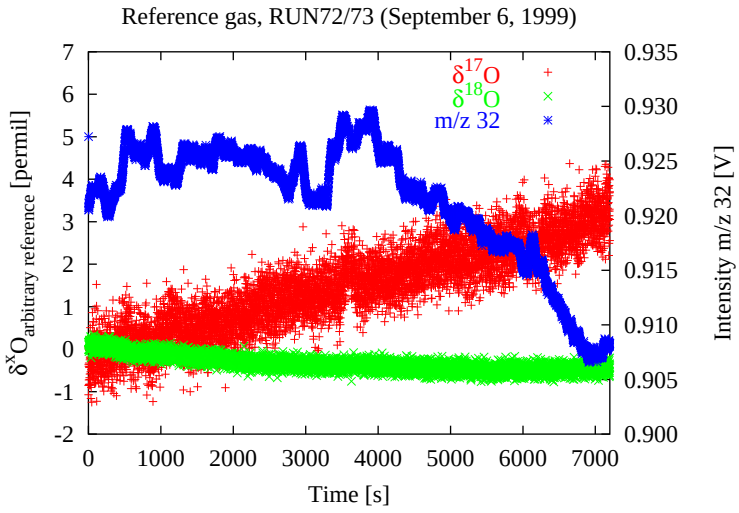

Figure 4.6: Drift of δ^{17}O and δ^{18}O and of the m/z 32 intensity plotted vs. the time in seconds. Note the, by factors, higher scatter of the δ^{17}O signal as compared to δ^{18}O.

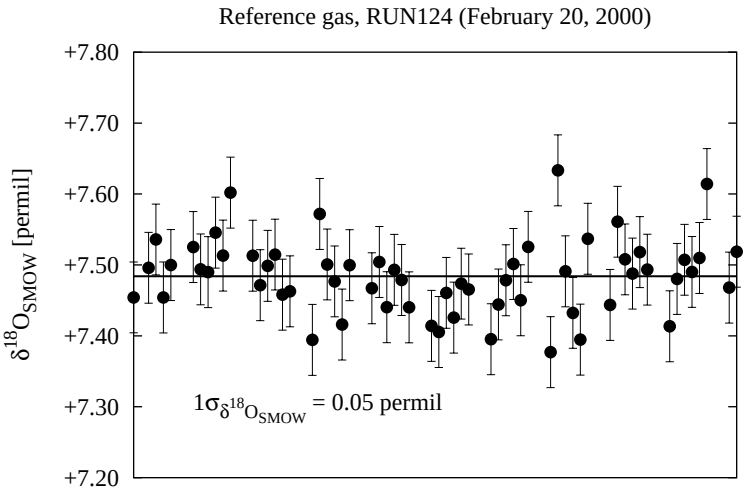

Figure 4.7: Plot of repeated measurements of reference gas. The 1σ standard deviation of the reference gas was ± 0.05 ‰. The data plotted were corrected for drift.

Accurracy and precision To check the accuracy and precision of the reference gas measurements (via *ConFlo-II*), bottle oxygen was repeatedly measured. It can be shown that both, accurracy and precision of the drift corrected reference gas measurements were within ± 0.05 ‰ ($1\,\sigma_{\delta^{18}\mathrm{O}}$, Fig. 4.7) with an accepted value of +7.48‰ for the house intern bottle oxygen reference gas (grade 5.5).

The precision in δ^{17}O seems to be limited by the mass spectrometer device itself rather than by the analytical procedure. Monitoring the ratio m/z 33/32 (2/1) which corresponds to the δ^{17}O values over an acceleration voltage interval (60 V) shows an assymmetrically shaped round 33/32 peak (Fig. 4.8). In contrast the 34/32 (3/1) peak shows a plateau developed flat topped over a wide range of acceleration voltage (Fig. 4.8).

Accurracy and precision of repeated standard measurements of a set of laboratory and international quartz standards (Lausanne Quartz: $\delta^{18}\mathrm{O} = +18.15$‰ (Sharp, 1999, pers. comm.), Campo Lungo Quartz: $\delta^{18}\mathrm{O} = +26.65$‰, GW-Quartz: $\delta^{18}\mathrm{O} = +12.45$‰, NBS-28: $\delta^{18}\mathrm{O} =$

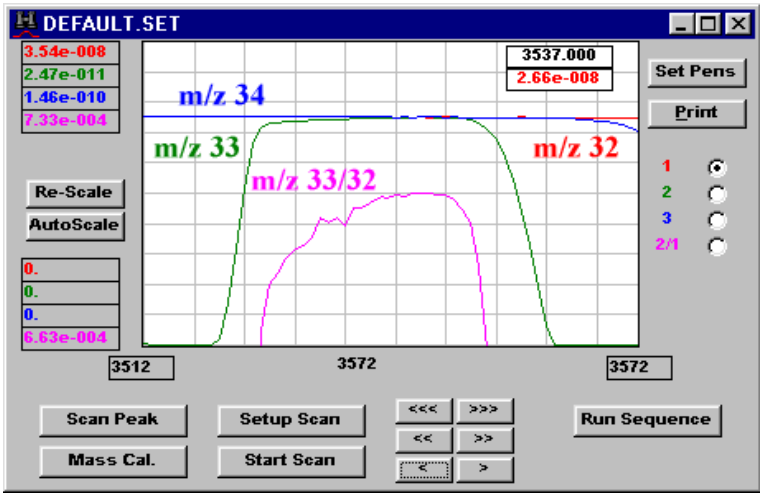

Figure 4.8: Plot of m/z 32, 33, 34, and of the ratio m/z 33/32 vs. the acceleration voltage as it is displayed by the Anca software. Note the round topped asymmetric m/z 33/32 ratio. In contrast to that, the ratio m/z 34/32 remains over a wide range absolutely constant. The absence of a flat top of the m/z 33/32 signal may be the reason for the scattering of the δ^{17}O values.

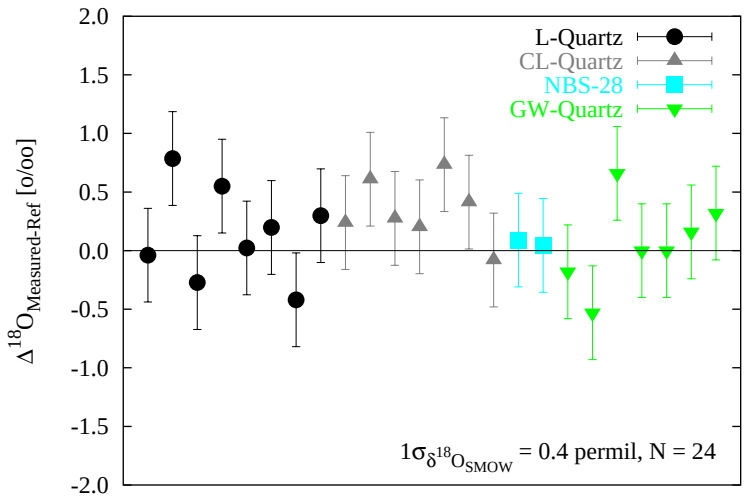

Figure 4.9: Plot of Δ^{18}O ($\Delta^{18}O = \delta^{18}O_{measured} - \delta^{18}O_{accepted}$) of 24 quartz standards.

+9.64‰) was found to be ±0.4‰ (1σ, Fig. 4.9).

Detection limits Merrit and Hayes (1994) and Young et al. (1998) introduced a method to estimate the theoretical detection limits of isotope-ratio-monitoring mass spectrometry (*irmMS*). The calculation is based on the *Poisson* distribution of the counting error ($1\sigma N = \sqrt{N}$) and the *Gaussian* law of error propagation.

$$\sigma^2_{\delta^{17}O} = \frac{2\times10^6(1+{}^{33}R_i)(1+{}^{33}R_i+{}^{34}R_i)}{{}^{33}R_i\times x_g\varepsilon\times n_{O_2}N_A} \quad (4.1)$$

$$\sigma^2_{\delta^{18}O} = \frac{2\times10^6(1+{}^{34}R_i)(1+{}^{33}R_i+{}^{34}R_i){}^{34}R_i}{\left({}^{34}R_i-\frac{{}^{33}R_i^2}{4}\right)^2 x_g\varepsilon\times n_{O_2}N_A} \quad (4.2)$$

x_g is the fraction of gas that enters the ion source, i. e. the split ratio of the open split valve. ε

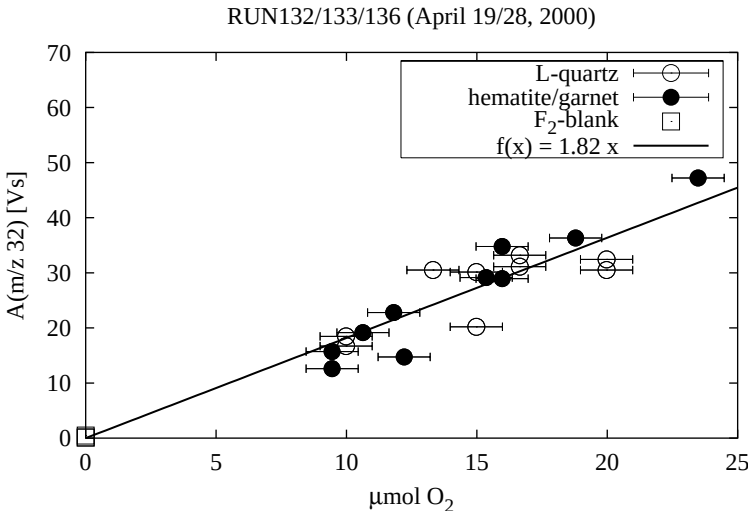

Figure 4.10: Plot of the integrated peak area A vs. the amount of O_2 in the sample. The horizontal error bars resulted from the estimated error of the balance used. The regression function is $A = 1.82 \times 10^6 n_{O_2}$

is the ionization efficency of the ion source and depends on geometry and parameter settings of the ion source. Values of 0.00414 for $^{34}R_i$ and 0.00075 for $^{33}R_i$, respectively, are suitable for most natural samples.

x_g and ε cannot be determined separately in a simple way. Thus, the effectivity coefficient E is introduced:

$$E = x_g \times \varepsilon = \frac{A}{n_{O_2} R_f q_e N_A} \tag{4.3}$$

where A is the integrated area of the measured peak in Vs, n the O_2 content of the sample in mol, R_f the resistance of the feedback resistor (for m/z 32 $R_f = 100\,\mathrm{M\Omega}$), q_e the charge of the electron (1.6×10^{-19} C) and N_A Avogardo's number ($6.022 \times 10^{23}\,\mathrm{mol}^{-1}$). The split ratio x_g correlates with the reciprocal He-flow rates as shown in Figure 4.11. E is determined by regression analysis of a set of n_{O_2} and A pairs (Fig. 4.10). n_{O_2} is assumed to be equal to $n_{^{32}O_2}$.

Using these data and equation 4.3 one can calculate E to $1.89 \times 10^{-7}\,\frac{\mathrm{Vs \times mol}}{\Omega \mathrm{C}}$. The split ratio x_g of the *ConFlo-II* interface at an He input of $80\,\mathrm{ml\,min}^{-1}$ is approximately 0.00625 assuming that $0.5\,\mathrm{ml \times min}^{-1}$ He enters the ion source. ε of the source of the *PDZ-Europa 20-20* mass spectrometer would then be approximately 3×10^{-5} ions/molecule. For CO_2, a value for ε higher than 1×10^{-3} ions/molecule is given (PDZ-Europa, 2000, http://www.europa-uk.com). Both, x_g and ε can be improved by changing the settings of the *ConFlo-II*[6] and the ion source.

Incorporation of E into equations 4.1 and 4.2 gives:

$$\sigma_{\delta^{17}O} = \sqrt{\frac{2.33 \cdot 10^{-8}}{n_{O_2}}} \tag{4.4}$$

[6]Reducing the He carrier gas flow from 80 to 20 ml/min, respectively, would increase the sensitivity by factor four (Fig. 4.11). Finnigan, however, recommended an input range between 80 and 180 ml/min. Reducing the flow to values less than 80 ml/min could lead to an increase of the background through air inlet.

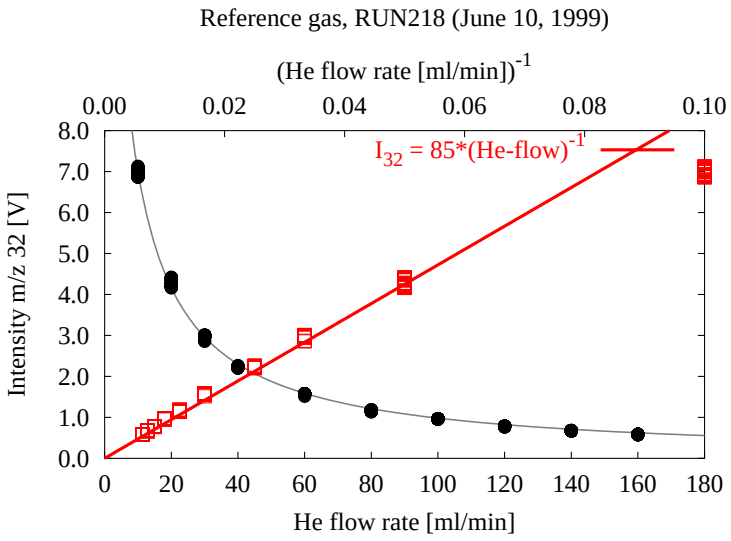

Figure 4.11: Plot of the intensity of the m/z 32 signal in V vs. the He-flow rate in ml/min (bottom axis) and the reciprocal He-flow rate (top axis).

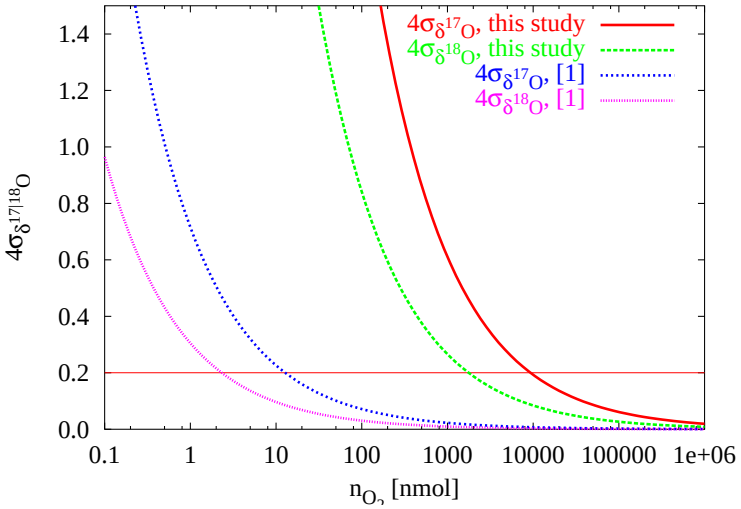

Figure 4.12: Estimated precision for $\delta^{17}O$ and $\delta^{18}O$ as a function of the sample size in nmol O_2. According to Young et al. (1998), a given 4σ corresponds to a realizable 2σ. A quantity of 2500 nmol which marks the estimated lower limit ($2\sigma \leq \pm 0.2‰$) corresponds to an amount of 0.15 mg quartz.

$$\sigma_{\delta^{18}O} = \sqrt{\frac{4.42 \cdot 10^{-9}}{n_{O_2}}} \tag{4.5}$$

Sample fluorination, gas handling and blank correction potentially limited the precision given in figure 4.12. The error in $\delta^{18}O$ of the measured samples (1 mg) was ±0.35‰ (Fig. 4.9) illustrating that the theoretical error did most probably not influence the precision achieved.

Fluorine consumption and blank intensity The amount of fluorine $p_{F_2}^{cons.}$ consumed by the entire decomposition of the sample is proportional to the mole fraction of oxygen in the sample and the amount of sample if all fluorine consumed resulted in liberation of oxygen. Fluorine pressures in the reaction chamber are measured using a pressure gauge with a reproducibility in the range of ±0.1 mbar. Excess fluorine is converted to Cl_2 which is collected

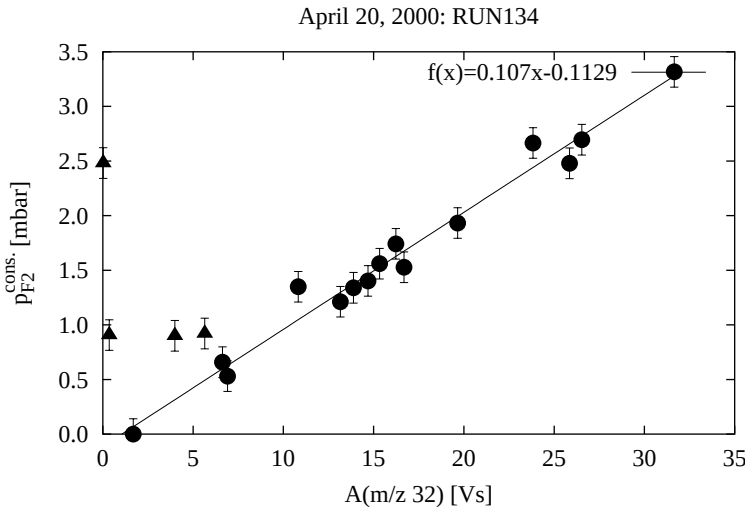

Figure 4.13: Plot of $p^{cons.}_{F_2}$ [mbar] vs. the peak area of the m/z 32 signal [Vs]. The samples with the filled triangle symbols where excluded from the regression calculation since they obviously consumed fluorine gas, but did not release equivalent amounts of oxygen. Contents of metallic iron, nitride or carbide would cause such an effect.

in the cooled 1/4" U-tube. The U-tube is heated between each sample to re-trap the Cl_2 in the glass cold trap.

The pressure of Cl_2 released from the U-tube is measured using a Pirani pressure gauge with arbitrary unit (au). The Pirani gauge is scaled using the fluorine blank (i. e. without fluorine consumption).

$$p_{Cl_2}[mbar] = k \cdot p^{Pirani}_{Cl_2}[au] \tag{4.6}$$

$$k = \frac{p^{chamber,blank}_{F_2}}{p^{Pirani,blank}_{Cl_2}} \left[\frac{mbar}{au}\right] \tag{4.7}$$

$$p^{cons.}_{F_2} = p^{chamber}_{F_2} - p_{Cl_2}[mbar] \tag{4.8}$$

It is expected that the Cl_2 pressure behaves proportional to the difference between the amounts of fluorine and sample oxygen since $n(Cl_2) = n(F_2) - n(O_2)$. In turn, the amount of sample oxygen is proportional to the peak area A of the m/z 32 peak.

Figure 4.13 illustrates the relation between the amount of F_2 consumed (ordinate) and the peak area of the m/z 32 signal (abscissa). Three samples which were excluded from the regression calculation, obviously contained components that reacted with fluorine, but did not release oxygen. Metallic iron, carbide or nitride would show such a behavior and, indeed, were present in the samples.

The abscissa axis intercept gives the value of the blank intensity which should be subtracted from the raw peak areas. Using this axis intercept, blank correction would be possible without blank measurements. This method, however, can only be applied when the sample amounts vary in a range that justifies regression analysis. Furthermore there should be no components in the sample that react with the fluorine without releasing oxygen. This condition is fulfilled for most geological samples. Of course, system settings should not be changed and the k-factor (Eqn. 4.7) must be determined.

Exhaustion of the KCl-column will be displayed recognized by a non-correlation be-

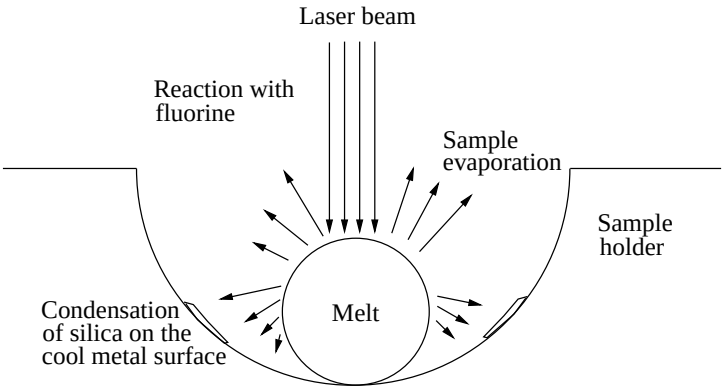

Figure 4.14: Sketch illustrating the evaporation and condensation of a silica droplet in the sample holder. The deposits are most probably highly enriched in ^{18}O relative to the sample. Consequently, loosing this deposits leads to too low $\delta^{18}O$ values.

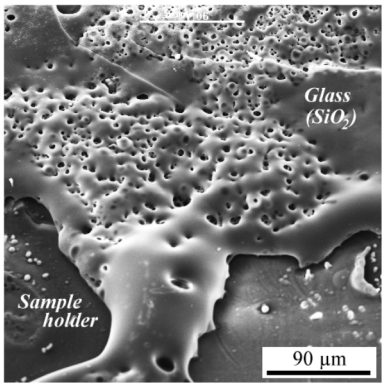

Figure 4.15: SEM image of glassy silica deposits remaining on a Pt plated sample trough after analyzing quartz.

tween F_2 consumption and peak area. Samples will fall in a field below the regression line since apparently more oxygen is produced and less fluorine consumed.

Sample fluorination After releasing 4–8 mbar F_2 to the chamber, samples are heated with the defocussed laser beam using the *Synrad* CO_2 gas laser ($\lambda = 10600$ nm). Pulse frequency is varied between 200 kHz and 2 MHz and pulse width between 0.2 μs and 2 μs. The energy is increased stepwise with a defocussed beam until the sample starts to melt and to react with the fluorine atmosphere. Maximum pulse intensities were in the range of 50% of the maximum laser power of 25 W. After fluorination of the major part of the sample, a focussed beam is used to fluorinate the rest of the sample. SiO_2-rich samples melt to a droplet and then slowly react with the fluorine. The reaction by-product is SiF_4 which is gaseous and thus does not disturb the reaction. In contrast, alumina-rich sample react violently under formation of solid AlF_3. Addition of LiF to the alumina-rich samples impedes the reaction and, furthermore, binds a part of the AlF_3 through formation of a fluoride melt.

A problem encountered especially when analyzing quartz is the condensation of SiO_2 vapor on the metal surface of the sample holder (Figs. 4.14, 4.15). This vitreous vapor deposits are difficult to bring back to reaction with the laser since the metal efficently leads off the heat. Plating the sample troughs with platinum did not solve that problem (see Fig. 4.15). Increasing the fluorine pressure, however, reduced the formation of condensates considerably.

The alumina-rich samples show a different behavior. These samples immediately react when slightly heated with the laser beam. The disintegration reaction of alumina to AlF_3 and oxygen is strongly exothermal and is, over short periods, self-preserving. Unlike most fluoride raction products, AlF_3 is solid even at elevated temperatures (sublimation temperature at 1260°C). If the lasering procedure is not controlled very carefully, sputtering of sample material and reaction products thoughout the chamber will occur through the violent

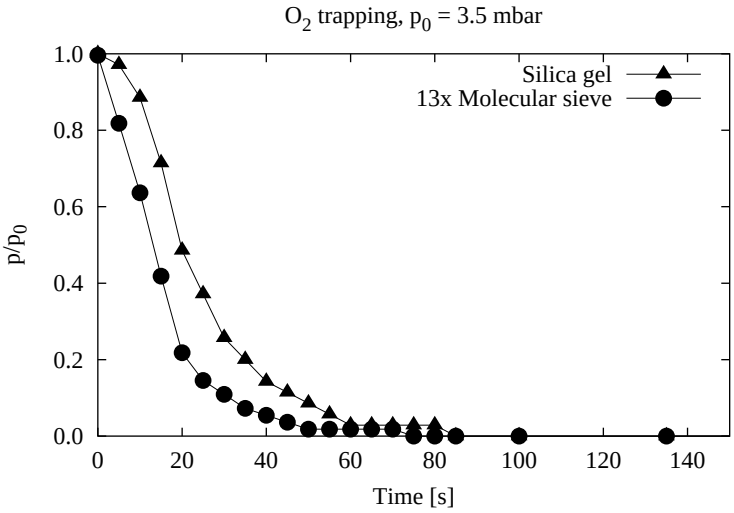

Figure 4.16: p/p_0 (O_2) measured in the sample chamber plotted vs. the trapping time.

reaction.

Sample handling A crucial step in the determination of the oxygen isotope composition is the sample gas handling. The entire sample should be fluorinated. Excess F_2 should be converted to Cl_2 which should be trapped in a cooled 1/4" U-tube. Then the purified sample oxygen is expected to be collected on a cooled molecular sieve or silica gel filled trap.

To determine the time necessary to transfer and trap the oxygen on the molecular sieve, the line[7] was filled with 3.5 mbar oxygen. The pressure was monitored using the pressure gauge attached to the chamber.

Figure 4.16 illustrates relation between the O_2-pressure in the chamber and the trapping time. After 100 s, apparently the entire oxygen is trapped on the silica gel or 13× molecular sieve. Thus a total trapping time of 360 s (6 min) is reasonable. This is applies to routine measurements, where the amount of oxygen is by one order of magnitude lower than in this experiment.

Contamination of the sample oxygen with excess fluorine may contribute to errors in measurement. Therefore the conversion of fluorine to chlorine in the KCl column was investigated in an experiment. Approximately 10 mbar F_2 was expanded from the chamber to the KCl-column and the Cl_2 cold trap[8]. Assuming that the freezing of Cl_2 is by magnitudes faster than the conversion of F_2 to Cl_2, this experimental setup is expected to give informations about the conversion velocity of F_2 to Cl_2 in the KCl column. Figure 4.17 illustrates that a conversion time of 2 min is reasonable to convert the entire excess fluorine to chlorine gas, also when considering that the amount of fluorine converted in the experiment is at least two times bigger than the amount converted during routine measurements.

[7]The entire line including chamber, KCl-column and Cl_2-trap was filled with oxygen. The oxygen trap was pre-cooled and time was started when the oxygen entered the trap. A decrease of pressure due to expansion of the gas into the horseshoe bend was determined (factor 0.83) and considered.

[8]The expansion lead to a pressure decrease being in the range of factor 0.45. This decrease was considered in the plot in Figure 4.17.

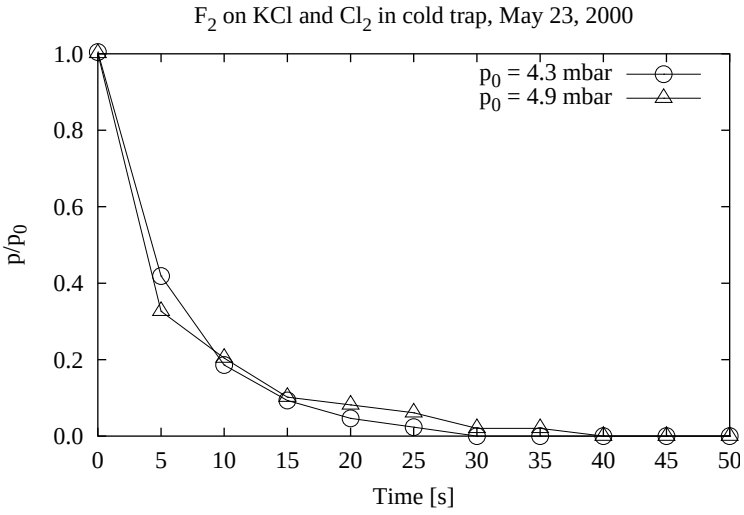

Figure 4.17: p/p_0 (F_2) measured in the sample chamber plotted vs. the time of conversion. A minimum conversion time of 2 min is recommendable to ensure the entire conversion of F_2 to Cl_2.

4.2 Standard analytical methods

4.2.1 XRF-analysis

Chemical whole rock analyses were performed at the Department of Mineralogy in Bonn using a *Philips PW1480* X-ray fluorescence spectrometer. Samples were crushed and iron metal was removed using a hand magnet. Especially the metal-rich clogging samples were difficult to separate from adjacent steel droplets. Since no hydrous phases were present in the clogging as well as in all other samples as indicated by XRD, the determination of loss of ignition was omitted for most samples.

The more or less iron metal free samples were milled using a *Siebtechnik* WC swingmill. The powdered samples were mixed 1:10 with lithium-tetra-borate and a spatula NH_3NO_4 to oxidize the traces of iron metal prior to fusion. 30 mm glass discs were prepared and automatically measured in the XRF machine. Precision, calibratedconcentration range and detection limits of the analyzed elements are reported on the website of the Department of Mineralogy in Bonn under http://www.min.uni-bonn.de.

4.2.2 XRD-analysis

The phase composition was determined by X-ray powder diffraction on powdered samples. Samples were measured using a *Siemens D-5000* X-ray diffractometer and side loading PVC-sample holders. The phases were identified with aid of the Siemens PC-based evaluation software package *EVA*.

Quantitative Rietveld analysis was performed on a set of selected samples using the *AXS WinRiet* software package (a full version was kindly made available by *AXS*). Since sample preparation technique including milling and sample loading are crucial steps for Rietveld analysis, the relative error of quantitative analyses lies in the range of 5–20 wt.%.

4.2.3 EPMA

Electronprobe microanalysis and back-scattered electron imaging were performed using a *Jeol JXA8900 RL* electron microprobe at the Department of Mineralogy and Geochemistry in Cologne. Calibration of elements was performed prior to each set of analyses using the settings as listed in Table 4.1.

Table 4.1: Settings for elemental calibration of the *Jeol JXA8900 RL* electronprobe used for microanalysis.

Elem.	Standard	X-ray	X-tal	U [kV]	I [nA]	λ [Å]	Peak [s]	B.g. [s]
Cr	Cr_2O_3	K_α	LIFH	15.0	15.0	2.28970	20	10
Mn	$MnSiO_3$	K_α	LIF	15.0	15.0	2.10182	40	20
Ti	TiO_2	K_α	PETJ	15.0	15.0	2.74851	30	15
Fe	Fe_2O_3	K_α	LIF	15.0	15.0	1.93604	20	10
Ca	$CaSiO_3$	K_α	PETJ	15.0	15.0	3.35839	20	10
Mg	MgO	K_α	TAP	15.0	15.0	9.89000	20	10
K	$KAlSi_3O_8$	K_α	PETJ	15.0	15.0	3.74140	5.0	2.5
Na	$NaAlSi_3O_8$	K_α	TAP	15.0	15.0	11.91010	10	5.0
Al	Al_2O_3	K_α	TAP	15.0	15.0	8.33934	20	10
Si	$CaMgSi_2O_6$	K_α	TAP	15.0	15.0	7.12542	20	10

4.2.4 Scanning electron microscopy

For electron microscopy a *Jeol 6400 F* scanning electron microscope equipped with field emission gun and a *Noran Voyager* energy disperse X-ray detector at the *Werkstoffzentrum Rheinbach GmbH* was used. To make the surface electrical conducting, samples were coated with carbon prior to electron microscopy. Spatial resolution was below 0.5 μm in imaging mode. Al_2O_3-rich fine-grained samples were difficult to study because they irritated the beam due to electrostatic charge effects. Chemical analyses were obtained using the energy dispersive X-ray detector without standardization. Therefore the analytical error of these measurements was assumed to be in the range of a few weight percent.

4.2.5 Transmitted electron microscopy

Transmitted electron microscopy was conducted at the Institute of Inorganic Chemistry (Bonn) using a *Philips CM 300 VT* equipped with a field emission gun and a Gatan imaging filter.

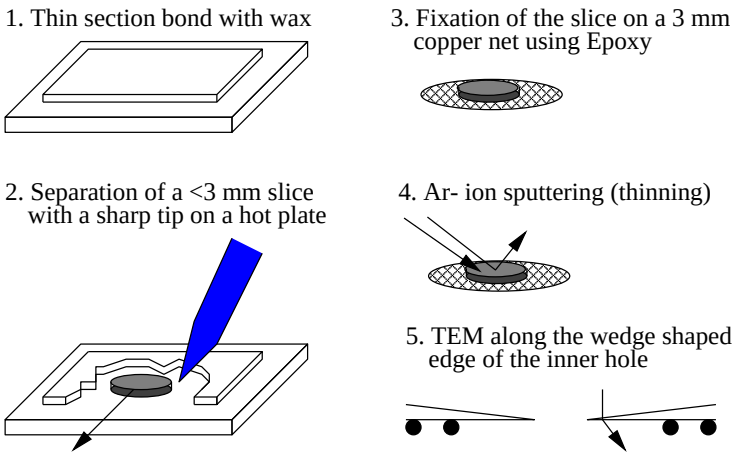

Figure 4.18: Sketch illustrating the sample preparation steps for transmission electron microscopy: 1) Preparation of a polished thin section, 2) Separation of a slice of the sample on a hot plate with the tip of a separation needle, 3) Transferring of the slice on a 3 mm copper net TEM sample holder, 4) Thinning of the sample with an Ar-ion beam, 5) Microscopy along the wegde shaped edge of the hole produced by the Ar-beam.

Sample preparation

A polished thin section ($\approx$30 μm) was prepared. But, instead of bonding the sample with Epoxy resin on the glass holder, it was glued with *Logitech LCON-286 wax concrete*. A 3 mm slice was isolated from the rest of the thin section by scratching it with the tip of a separation needle on a hot plate. The wax melts at 110–120°C so that the slice can easly be isolated and pushed on a copper net TEM sample holder.

The slice then is fixed with a thin film of Epoxy resin on the copper net. This compound was put in the Ar-ion sputtering machine. As a result of sputtering a hole was produced in the center of the sample. Along the wedge shaped edge of the whole TEM was possible. For most materials, a thickness up to 100 nm is electron transparent (Buseck, 1992).

Bright field imaging

In bright field imaging, only the undiffracted beam (000) is allowded to pass through the objective aperture into the imaging system. Differences in orientation between adjacent lattices are visible by their brightness contrast. For details, the reader is referred to Putnis (1992) or Buseck (1992).

Element analysis

Semiquantitative element analyses were performed by electron energy loss spectroscopy (EELS, standard 3-window method). Some of the incident electrons cause ionization of inner shell electrons. Those electrons suffer an energy loss which is characteristic for the inner shell electron bindings. Since the energy loss is proportional to the number of electrons in the transmitted volume and the TEM sample is wedge shaped, a thickness correction had to be performed. The thickness of the sample can be estimated by calculating the ratio of the

unfiltered and elastic bright field intensities. Si (Lα), O (Kα), Fe (Lα), and Mg (Kα) were analyzed by EELS in olivine and iron.

Chapter 5

Intefix–A numeric integration program

5.1 Introduction

After measuring the batch including blank, reference and sample, the *Ancrepro* software is started to calculate the actual δ^{17}O and δ^{18}O values of the samples.

A disadvantage of the *Ancrepro* software is the disability of calculating δ^{17}O and δ^{18}O with oxygen gas as analyte. Instead, it calculates δ^{17}O and δ^{18}O as if the analyte is CO_2 producing a deviation, depending on the δ^{18}O value, being in the decile rank on the ‰ scale. Furthermore, the Anca software lacks a proper documentation, especially concerning drift correction, making the user feeling somewhat uncomfortable since he or she does not really know what is going on.

Especially drift and blank corrections seemed to be somewhat arbitrary. The user has no control about the magnitude of the drift occurring. The output of peak areas does not correspond to the actual measured signal. But for the calculation of parameters like ionization efficiency of detection limit, it is essential to know the peak areas. Furthermore, an output of the results including all parameters used for drift and blank correction in a proper *Excel*- or *StarOffice*-sheet is not possible with the *Ancrepro* software.

Therefore, there was a need for a software which can read the raw data and calculate the peak areas and the resulting δ^{17}O and δ^{18}O values. The results should be written in a table which can be read with standard *Windows* based table calculation software.

The integration program *Intefix* is written in *C* on an *Intel Linux* platform (*SuSE Linux 6.1 and 6.4*). *C* was chosen because of its inter platform compatibility and of its high performance. Interpreter languages like *Perl* or *JavaScript* are also compatible with most organization systems but are by magnitudes slower and not as flexible as *C*. The *Linux* binaries are compiled with the open source *gcc* C-compiler (version 2.95.2-52, GPL). The binary for *Windows9x/NT* is compiled using the *Microsoft* C-compiler which is part of the *VisualStudio* (version 6.0) development package.

No system specific programming code or libraries were included to ensure the inter platform compatibility. A listing of the source code is added to the appendix and is contained on the attached CD-ROM.

5.2 Program documentation

The output of the *Ancrepro* software comprise of a text file with numbers listed in three columns. Each row represents an 1 s integration interval and each column one of the three masses monitored simultaneously. Integration of the peak areas of the three monitored masses is the first step in data evaluation. It proved to be very difficult, if not impossible, to find one or a combination of physical functions to fit the asymmetric sample peaks. Therefore, a numerical integration procedure is performed by *Intefix*.

The integration of the measured signal is a crucial step in isotope ratio monitoring. The peak areas are designated as I^{32}, I^{33}, and I^{34} and have the unit As. The ratios of the peak areas are calculated using equations 5.1 and 5.2.

$$R^{33} = \left(\frac{I^{33}}{I^{32}}\right) \tag{5.1}$$

$$R^{34} = \left(\frac{I^{34}}{I^{32}}\right) \tag{5.2}$$

The isotope ratios R^{17} and R^{18} are defined as:

$$R^{17} = \left(\frac{R^{33}}{2}\right) \tag{5.3}$$

$$R^{18} = \left(\frac{R^{34} - (R^{17})^2}{2}\right) \tag{5.4}$$

With R^{33} and R^{34} being the ratios of the monitored masses $^{33}O/^{32}O$ and $^{34}O^{32}O$. Equation 5.4 considers the possibility, although very unlikely, of an O_2 molecule with mass 34 constituted of two ^{17}O atoms. The $\delta^{18}O$-value relative to the measured reference is defined as:

$$\delta^{18}O_{Reference} = 1000 \times \left(\frac{R^{18}_{Sample}}{R^{18}_{Reference}} - 1\right) \tag{5.5}$$

$$\delta^{17}O_{Reference} = 1000 \times \left(\frac{R^{17}_{Sample}}{R^{17}_{Reference}} - 1\right) \tag{5.6}$$

On earth, with rare exceptions[1], all samples lie on the terrestial fractionation line defined by the relation $\delta^{17}O = 0.52 \times \delta^{18}O$ (Miller et al., 1999). Both, R^{17} and R^{18} calculated from the measured data are not the true ratios of the corresponding isotopes. However, the relative deviation of the calculated R-values from the true R-values which is in the range of only a few percent is equal for reference and sample and thus can be eliminated in equations 5.5 and 5.6.

For comparability, the $\delta^{18}O$-value is reported relative to an international accepted standard. In this study, all values are reported relative to the V-SMOW (*Vienna Standard Mean*

[1]Mesospheric and stratospheric ozone (O_3) and carbon dioxide may deviate from the terrestial mass fractionation line as shown by Thiemens et al. (1995) and Thiemens (1999).

Table 5.1: Example for a protocol created during a run. Date, username, and name of the file should also be noted.

No	Sample	Type	Begin peak	End peak	Annotations
1	Dummy	Dummy	20	100	—
2	Oxygen	Ref	20	100	—
3	Fluorine only	Blank	30	90	4 mbar F_2
4	GW-Quartz	Sample	30	150	0.9 mg, O. K., 4 mbar F_2
...	...	...	...	...	

Ocean Water) standard with $R^{17} = 3.73897 \times 10^{-4}$ and $R^{18} = 2.0052 \pm 0.00045 \times 10^{-3}$ (see Prosser, 1998).

$$\delta^{18}O^{Sample}_{SMOW} = \frac{\delta^{18}O^{Sample}_{Reference} + \delta^{18}O^{Reference}_{SMOW} + \left(\delta^{18}O^{Sample}_{Reference} \times \delta^{18}O^{Reference}_{SMOW}\right)}{1000} \quad (5.7)$$

5.3 User manual

5.3.1 Before one starts

If possible, all peaks should be set at the same position on the time scale (for instance the peak maximum should always be at 100 s). That means, that the oxygen should be liberated from the trap and sent to the mass spectrometer always at the same time (may be within ±5–10 s) and at the same temperature. The same is valid for the reference oxygen injected through the *ConFlo-II* interface. It is convenient and recommendable to note the positions (in s) of the peak beginnings and their ends. An example for a protocol table created during a run is given in the Table 5.1.

5.3.2 Export of the measured scan points

The *Ancrepro* software allows to export the scan points as text file in the *file* menu. The text file written has the same name as the file opened with Ancrepro with the ending *.txt* instead of *.bch*. The text file written contains data in three columns representing the data simultaneously collected on the three detector cups. Each row corresponds to an integrated time interval of 1 s. Each scan (corresponding to one sample, blank or reference) begins with a row of strings (Beam1 Beam2 Beam3:Scan *n*) with *n* being the number of scan (begins with $n = 0$).

The text file should be stored in the same directory where the *Intefix* binary (`intefix.exe` for Windows and `intefix.bin` for Linux) is stored. It is important to ensure write permission in the folder used since the program requires to write temporary files as well as the output file into this directory.

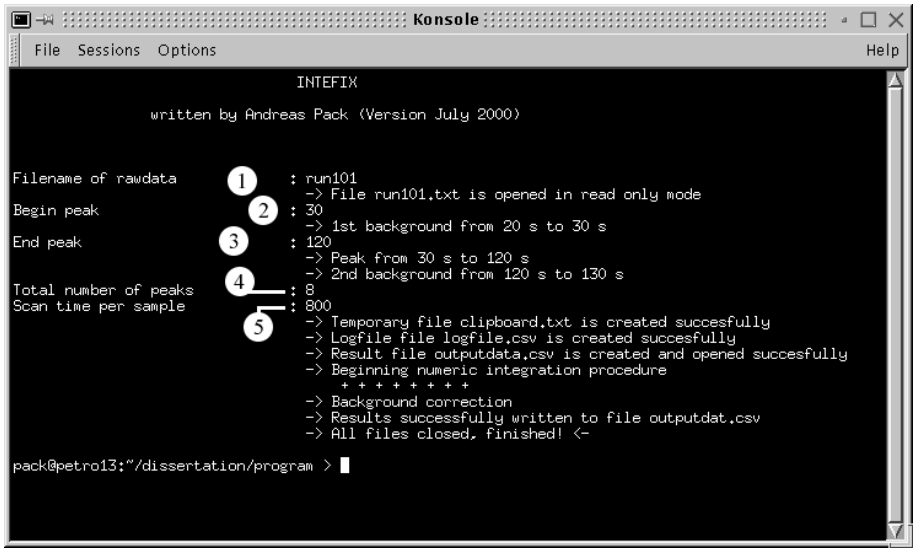

Figure 5.1: Screenshot of *Intefix* in a terminal window under *X11*. The appearance of the program is identical in a *DOS*-window under *Windows*. The five steps are described in the text.

5.3.3 Intefix step by step

Be sure that the *Intefix* binary and the text file with the data are in the same folder. Start the program by double clicking. A window as shown in Figure 5.1 will appear.

1. Type in the name of the raw data file *without* the ending (`.txt`), which is added automatically. Under Linux, it is distinguished between upper and lower case letters; always confirm with *ENTER*.

2. Type in the pre-peak position of the background

3. Type in the post-peak position of the background

4. Type in the total number of peaks (scans) of the individual batch, including dummy, blank and reference gas measurements

5. Type in the scan time per individual sample; confirm with *ENTER*

After typing in all the data required, *Intefix* opens the rawdata file and calculates the peak areas. The background is a linear interpolation between pre- and post-peak background (Fig. 5.2).

The peak areas of the three peaks of each individual peak are written in the file named *outputdata.csv* (*csv* is an abbreviation for comma separated values). This file can be opened in standard spread sheet software. The blank correction can be calculated manually. The blank corrected peak areas have to be written in the three columns termed *Beam1(BC)*, *Beam2(BC)*, *Beam3(BC)*. For reference gas injected via *Con-Flo* interface, of course, no blank correction

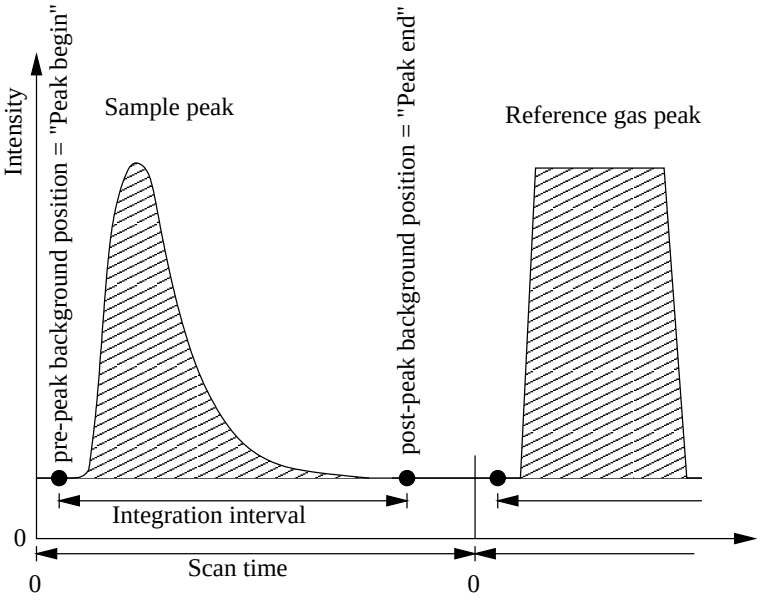

Figure 5.2: Drawing illustrating the positions of pre- (= ”Peak begin”) and post-peak (= ”Peak end”) background and the integration area. The background is calculated by linear interpolation between pre- and post-peak background and is subtracted from the calculated raw peak area.

has to be performed. The average 17R and 18R value must be inserted at the bottom of the columns termed 17R and 18R (using the =AVERAGE() function, the value must be inserted with one row left empty). The δ^{17}O and the δ^{18}O values of the reference gas used must be inserted (with one row left empty) to the bottom of columns D17O and D18O. The δ^{17}O and δ^{18}O values of all samples appears in the last two columns.

The user is free to calculate a drift correction or to leave out the blank correction. Since all δ^{17}O and δ^{18}O data, including those of the standards, are reported, the user has a good control about the drift or uncertainty of the line. For details see the example file on the CD-ROM.

Chapter 6

Petrography

6.1 Introduction

Calcium aluminate phases are widespread constituents of high-temperature refractory materials and cements. Since most of these phases are rare in natural systems, a short introduction is given here into the system of the calcium aluminates. Seven phases are known to occur in the binary system alumina-lime (Tab. 6.1, Fig. 6.1). The calcium aluminate phases are usually termed C_xA_y. The subscripts x and y denote the number of CaO and Al_2O_3 "molecules" in the mineral formula.

6.2 Ladle refractories

6.2.1 High alumina castables

Two samples of high-alumina castables were investigated by optical microscopy and BSE imaging. Sample 76a is composed of large porous grains and aggregates of corundum embedded in a fine-grained matrix. Only spinel and corundum could be identified microscopically. X-ray diffraction study indicated the presence of corundum and spinel with at least one additional, unidentified phase.

Sample 101 is a bauxite refractory castable with dark slag veinlets and adjacent slag (Fig. 9.1 , p. 91). As a result of reaction with the slag, the large porous grains of corundum of the refractory are surrounded by reaction rims composed of lath-shaped CA_6, subhedral isometric recrystallized grains of corundum and fine grained gehlenite as interstitial phase (Figs. 6.2 and 6.3).

Corundum vanishes towards the veinlet contact where the texture is solely represented by ophitic CA_6 and gehlenite, which is not observed to develop its own crystal habit. Adjacent to the reaction rim, massive CA_2 is observed which, in turn, is rimmed by CA. The veinlets are composed of an assemblage of Fe-rich spinel, gehlenite, CA, CA_2, wustite, metallic iron, and perovskite (Fig. 6.4). The amount of spinel increases towards the center of the veinlets. The spinel is euhedral with well developed $\{111\}$ (octahedral) crystal faces. Spinel appears

Table 6.1: Abbreviations, compositions and melting points of phases of the system CaO-Al_2O_3.

Mineral formula	Abbreviation	Melting point	Reference
CaO (lime)	CaO	2570°	Levin et al. (1964)
$Ca_3Al_2O_6$	C_3A	1535°C	Roth et al. (1982)
$Ca_{12}Al_{14}O_{33}$ (mayenite)	C_3A	1400°C	Roth et al. (1982)
$CaAl_2O_4$	CA	1600°C	Roth et al. (1982)
$CaAl_4O_7$	CA_2	1765°C	Roth et al. (1982)
$CaAl_{12}O_{19}$ (hibonite)	CA_6	1875°C	Roth et al. (1982)
Al_2O_3	cor	2020°C	Levin et al. (1964)

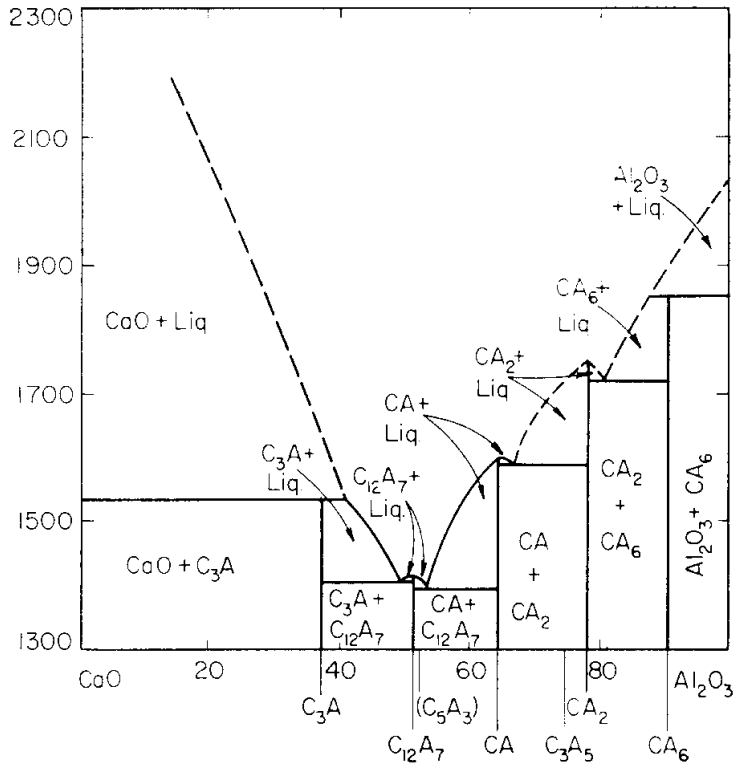

Figure 6.1: Binary system CaO-Al_2O_3 (from Levin et al., 1964).

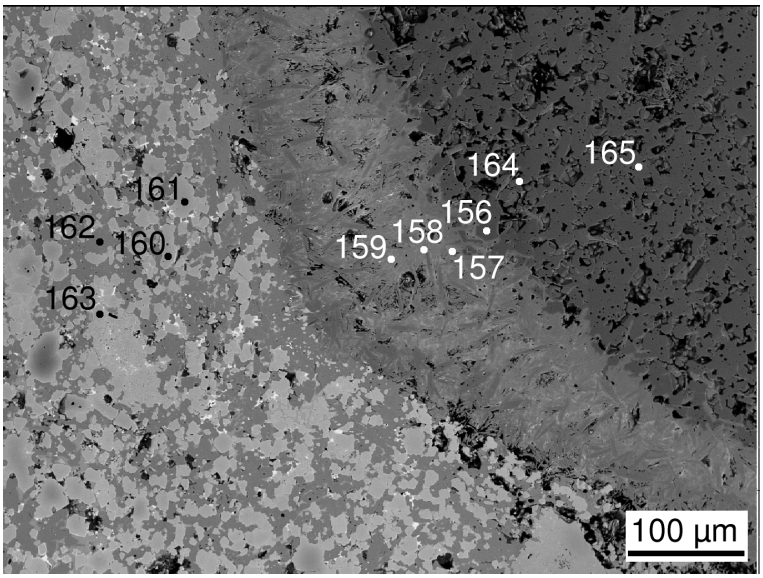

Figure 6.2: BSE image showing porous corundum surrounded by a reaction rim constituted of CA_6, corundum and gehlenite.

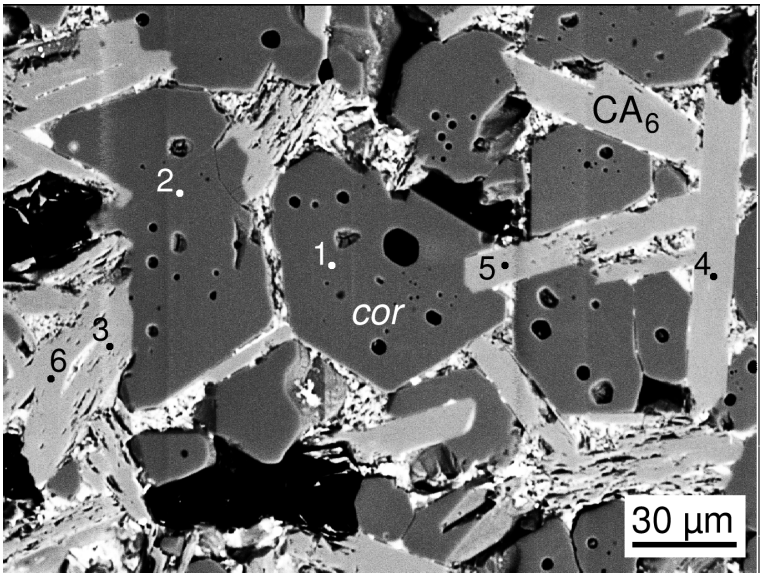

Figure 6.3: BSE image showing the reaction zone between corundum and the slag in veinlets. Corundum reacts with the melt to hibonite intergrown with corundum. Fine-grained gehlenite occurs as interstitial phase.

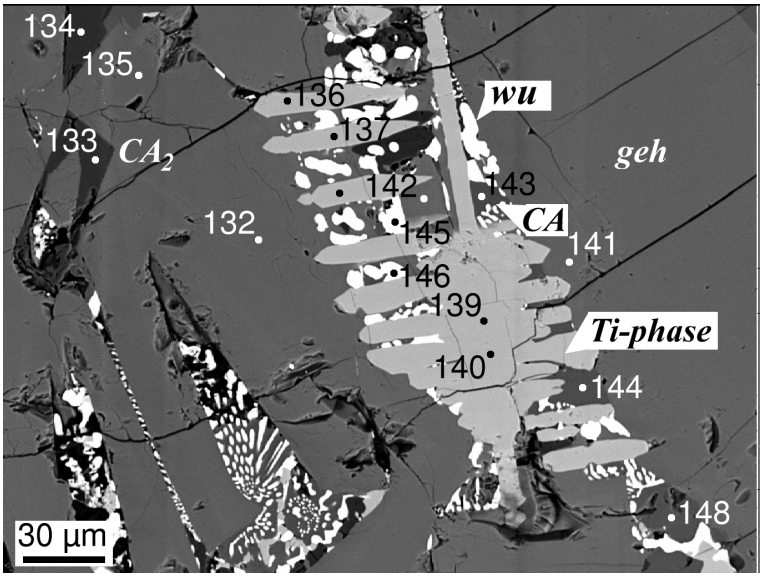

Figure 6.4: BSE image showing perovskite intimately intergrown with gehlenite in the melt veinlet. CA and CA_2 appear darker than gehlenite in back scattered electron images. The occurrence of wustite indicates oxygen partial pressures $\geq$IW.

dark green in transmitted light as typical of hercynite-rich spinel (Deer et al., 1966).

6.2.2 Basic refractory bricks

The basic refractory bricks are composed of large, brecciated aggregates of periclase embedded in an opaque C-rich matrix. Occasionally, aggregates develop pseudomorphs after magnesite.

In one sample (Sample 105), fluid inclusions were observed within grains of periclase (Fig. 6.5). The shape of the inclusions is controlled by the {100} cubic shape of periclase. The cubes appear to be aligned along the crystallographic axes. They originate, most probably, from the sintering process and have entrapped samples of the ambient atmosphere within the oven (Fig. 6.5).

6.3 Basic sprayed tundish lining

The sprayed tundish lining is composed of approximately 2/3 periclase and 1/3 olivine. Periclase occurs in large aggregates and as fine-grained constituent in the matrix. Olivine occurs as broken grain fragments embedded in the periclase-rich matrix.

Three zones are distinguished in the sprayed tundish lining (see Broß, 1995). These zones are distinct in a macroscopic as well as microscopic scale (Fig. 6.6).

The three zones are macroscopically denoted by their individual colors. The unaltered side is beige to brownish in color. The brownish color becomes more intense towards the dark brown intermediate zone which marks the reduction front that moves forward into the refractory during casting. The reduced melt contact zone is colorless with decreasing porosity towards the immediate melt contact.

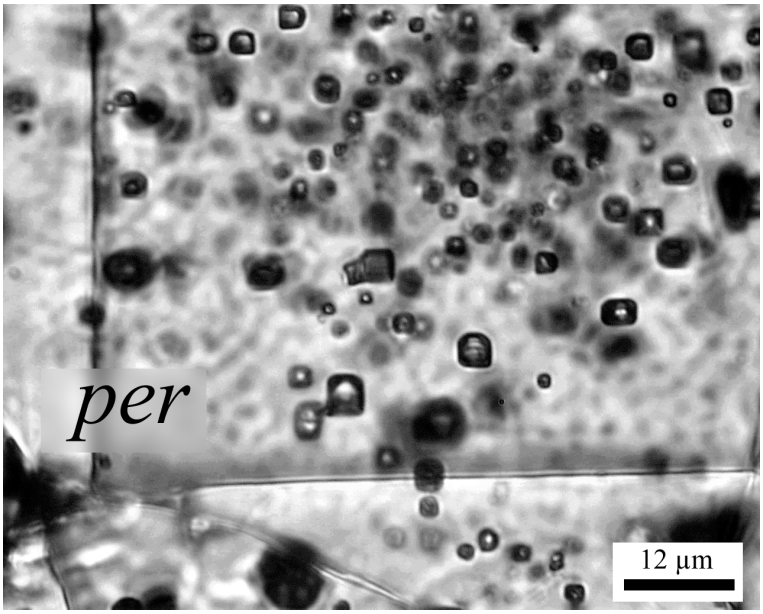

Figure 6.5: Transmitted light photomicrograph of fluid inclusions within a single grain from a large aggregate periclase (Sample 105). Note the cubic shape and the alignment along the outer edge of the grain.

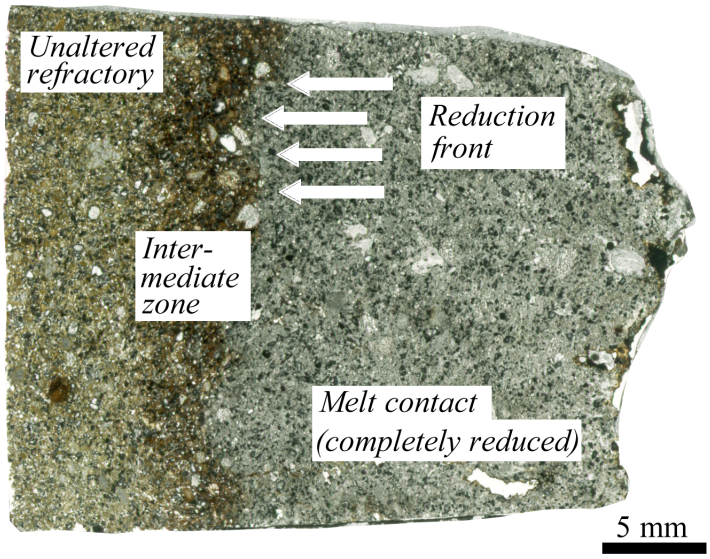

Figure 6.6: Photomicrograph of a thin section showing the three zones in the sprayed tundish lining. *left*: Unaltered beige to brownish refractory, *center*: Dark brown intermediate zone, *right*: Colorless reduced melt contact zone. The immediate melt contact is typically characterized by adjacent melt of the tundish slag and iron metal droplets (Sample 89).

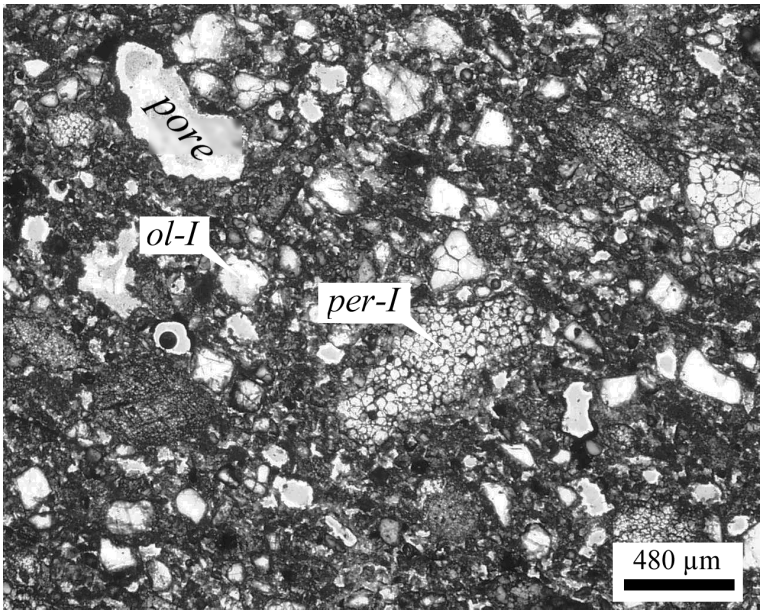

Figure 6.7: Overview of the texture of the unaltered basic tundish lining with the fine-grained brownish periclase matrix, olivine fragments, and aggregates of periclase (transmitted light photomicrograph, Sample 64).

The texture of the unaltered side is isotropic, hetero-granular with considerable porosity of up to 50 vol%. Periclase occurs as fine-grained fraction (Ø $\leq 30\,\mu$m, *per-II*) forming the intergranular matrix. Large aggregates of sintered periclase (Ø 200–1000 μm, *per-I*) and crushed angular olivine (Ø $\leq 300\,\mu$m, *ol-I*) occur within the periclase matrix. The periclase aggregates are constituted of rounded grains (Ø $20-50\,\mu$m) similar to those described in the basic refractory bricks.

Notable is the intense brown color of the rims of the large periclase aggregates and the matrix periclase (*per-II*). According to Broß (1995), this is due to stoichiometric substitution of Mg^{2+} by Fe^{2+} and minor amounts of Mn^{2+}. In contradiction, Konopicky (1957) and Trojer et al. (1981) report that periclase with minor contents of ferrous iron appears greenish in transmitted light, but admixture of magnesioferrite ($MgFe_2O_4$) would lead to a change in color from colorless to brownish. The generally highly reducing conditions in the sprayed tundish lining, buffered by the steel melt, however, rather point to ferrous iron than ferric iron in the periclase as pointed out by Broß (1995).

The rims of periclase in large aggregates are often brownish to yellow in colour, whereas the cores are always colorless (Fig. 6.8).

With progressing alteration, not only olivine, but also periclase becomes reduced. Unlike in olivine, no Fe metal exsolution was observed in periclase. The reduced olivine is occasionally overgrown by a second generation of colorless tephroitic olivine. Euhedral colorless spinel occurs in association with penetrating silicate melt of the tundish slag.

Figure 6.11 illustrates the changing mineralogy in the three different zones of the sprayed tundish lining. The reduction of olivine is accompanied by exsolution of tiny (Ø $<1\,\mu$m) blebs of metal (Figs. 6.8 and 6.12). Reduction proceeds from the rim to the core. The blebs are dispersed throughout the olivine grains causing a “dusty” opaque appearence in transmitted light. The exsolution blebs are often aligned along crystallographic orientations. The texture resembles very much that of “dusty” olivines known from some unequilibrated

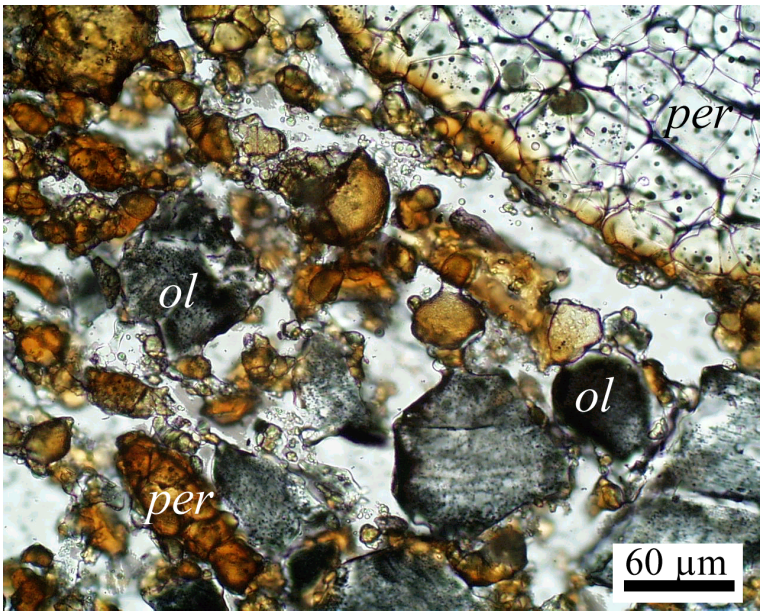

Figure 6.8: Reduced "dusty" olivine in association with FeO-rich matrix periclase in the intermediate zone (transmitted light photomicrograph, Sample 64). Note the FeO-rich brownish colored rim of the aggregates of periclase.

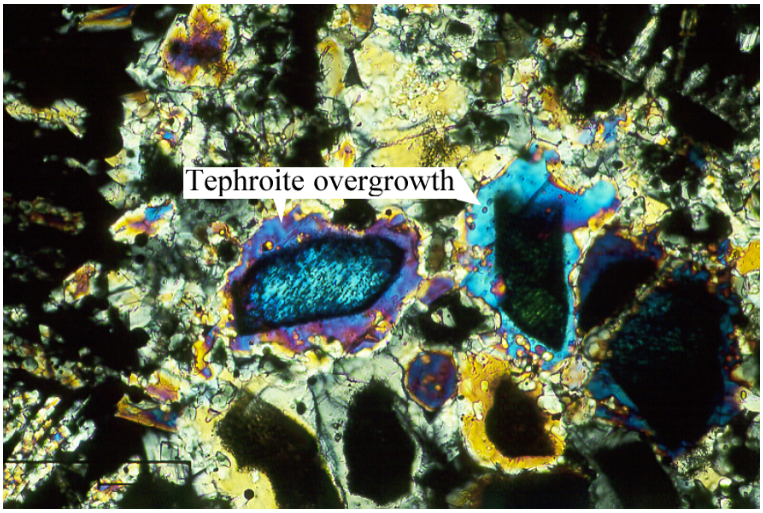

Figure 6.9: Photomicrograph (+N) of reduced olivine overgrown by colorless tephroitic olivine of the second generation (Sample 72).

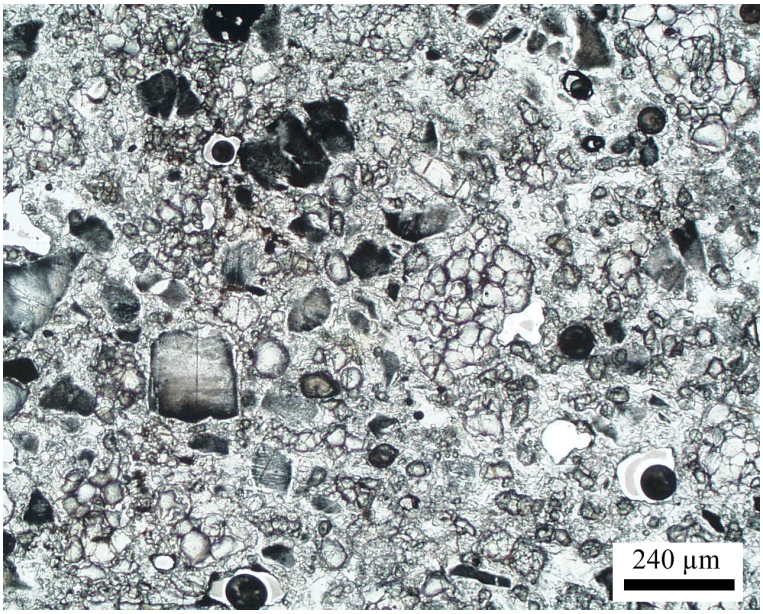

Figure 6.10: Photomicrograph (color) of the reduced side of the sprayed tundish lining with only reduced colorless phases. The reduced olivine fragments appear opaque (Sample 64).

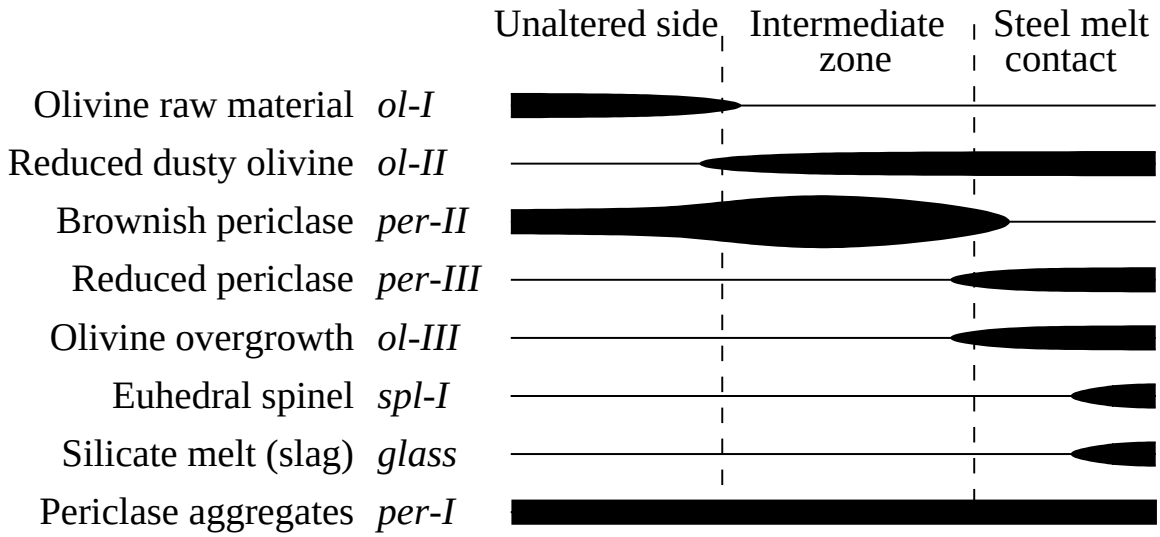

Figure 6.11: Sketch illustrating the mineralogical assambladges of the three zones of the sprayed tundish lining.

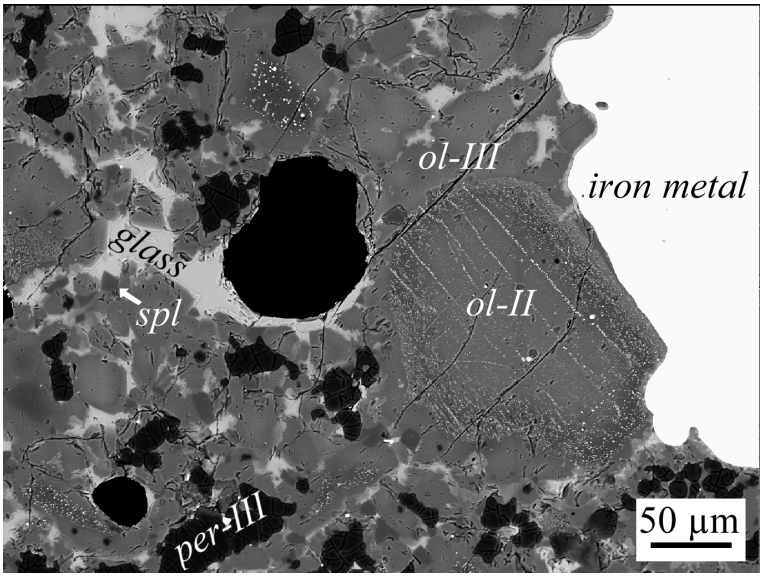

Figure 6.12: BSE image of a reduced olivine (*ol-II*) in the melt contact zone. Tiny droplets of iron metal exsolve from the olivine. Mn-rich olivine (*ol-III*) crystallizes from the silicate melt. Reduced periclase (*per-III*) appears dark due to its low molar mass. Spinel octahedra (*spl-I*) occasionally occur in association with the Mn-rich olivine and the glass (Sample 42).

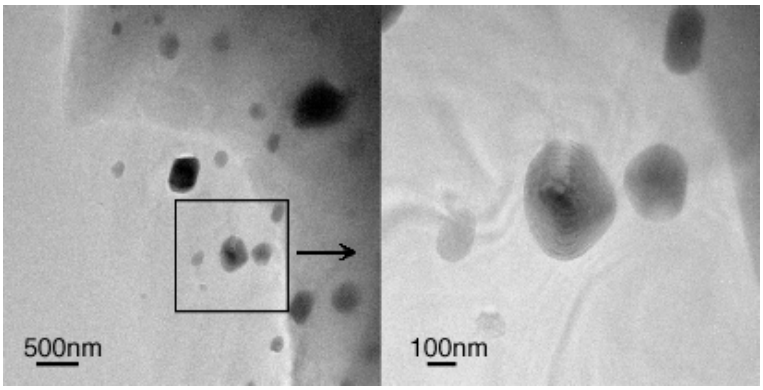

Figure 6.13: TEM bright field image of droplets of iron within the olivine host. Overview (*left*) and enlarged view (*right*) of a droplet of metal within its forsterite host. This image was taken in collaboration with T. Walther, Inst. of Inorg. Chemistry (Bonn). The olivine appears undisturbed even on nanometer scale.

meteorites as described by Jones and Danielson (1997). These olivines represent the products of solid state reduction of former FeO containing olivines. A similar process is responsible for the formation of the dusty olivine in the sprayed tundish lining.

Since the resolution of optical microscopy and the electron microprobe (BSE mode, Fig. 6.12) is not sufficient to resolve the fine structures in the olivine, transmitted electron microscopy was applied to study the exsolution features in more detail. No lattice disturbance of the olivine host could be detected along the immediate contact with the iron metal bleb (Fig. 6.13). Neither could the formation of a new phase like enstatite or glass be established by transmitted electron microscopy. The iron exsolutions range in diameter between $<$100 nm and 600 nm with a maximum at 150–200 nm (Figs. 6.13, 6.14). The aspect ratio was observed to vary between 1.0 and 1.9 with a maximum at 1.2–1.4 (Fig. 6.15).

It was observed by X-ray powder diffraction and Rietveld analysis, that the ratio fo/per increased dramatically from the unaltered zone ($fo/per \approx 0.5$) to the intermediate zone ($fo/per \approx 1.2$) towards the melt contact ($fo/per \approx 2$). The increase in the forsterite to

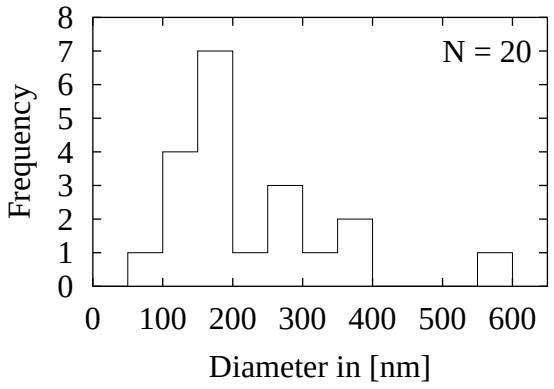

Figure 6.14: Plot of frequency vs. size of exsolution blebs or iron as measured by TEM ($N = 20$). Most grains vary in size between 150 and 200 nm.

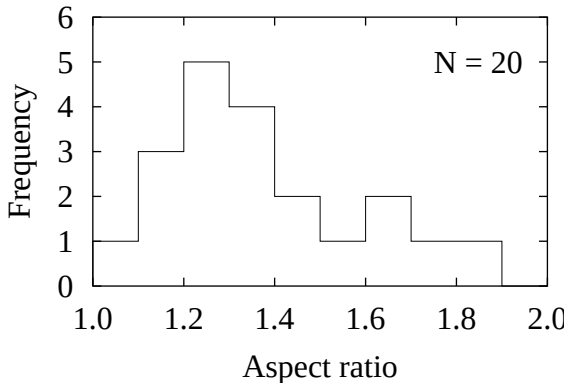

Figure 6.15: Plot of frequency vs. aspect ratio of exsolution blebs of iron as measured by TEM ($N = 20$). A distinct elongation of the blebs is observed with an aspect ratio mostly lying between 1.2 and 1.4.

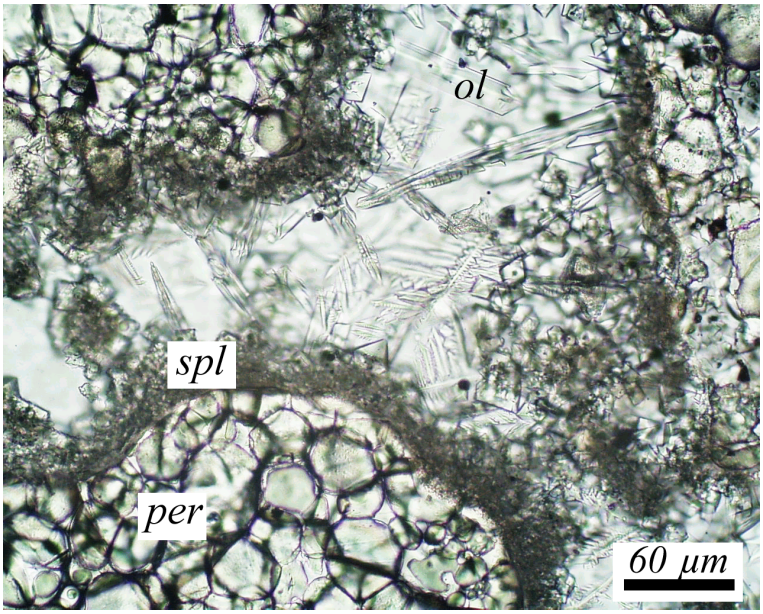

Figure 6.16: Transmitted light photomicrograph showing periclase in contact with the tundish slag. Periclase reacts with the melt to fine grained colorless spinel. Laths of colorless, quenced Mn-rich olivine occur isolated within the vitreous tundish slag (Sample 64). Melt infiltrates through the open porosity and along grain boundaries into the refractory.

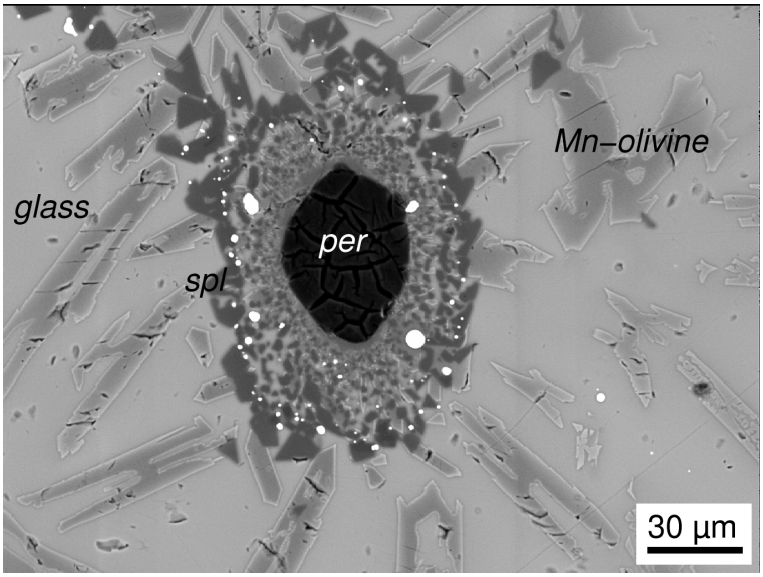

Figure 6.17: BSE image showing decomposition of periclase in contact with the silicate slag. Periclase is enclosed in a symplectitic reaction rim of glass, spinel, metallic iron, and Mn-rich olivine. Skeletal laths of Mn-rich olivine, typical for quenched phases, also occur isolated within the vitreous tundish slag (Sample 42).

Table 6.2: Average composition of alumina-rich clogging

Corundum	62 wt.%
Spinel (MA)	22 wt.%
Hibonite (CA_6)	13 wt.%
$Na_2Al_{22}O_{34}$	1 wt.%
Hematite	1 wt.%
Baddeleite (ZrO_2)	0.7 wt.%

periclase ratio is caused by the breakdown of periclase towards the contact with the steel melt.

The outermost few millimeters of the tundish lining are infiltrated by the vitreous tundish slag. Periclase reacted with the tundish slag melt to spinel (Figs. 6.16 and 6.17). Skeletal laths of Mn-rich olivine crystallized from the Mn-rich tundish slag.

6.4 Clogging

The clogging is generally very-fine grained and friable. The color varies between white and gray depending on the amount of tiny droplets of steel.

In most clogging samples, α-corundum was the predominant phase. Rietveld analysis was applied to estimate the relative proportions of the different phases (Table 6.2.

The spinel-rich samples 36 and 37 are composed of 85 wt.% spinel, 12 wt.% corundum, and 3 wt.% gehlenite.

In some individual cases, the occurence of CA, Fe_3C, and graphite is indicated by X-ray diffraction. C is introduced from the submerged entry nozzles. Baddeleite originates from zirconium-rich cement which is used to fix the SEN in the orifice of the tundish. Hematite is regarded as a secondary oxidation product of the adjacent metallic iron. Metallic iron was not identified by X-ray diffraction.

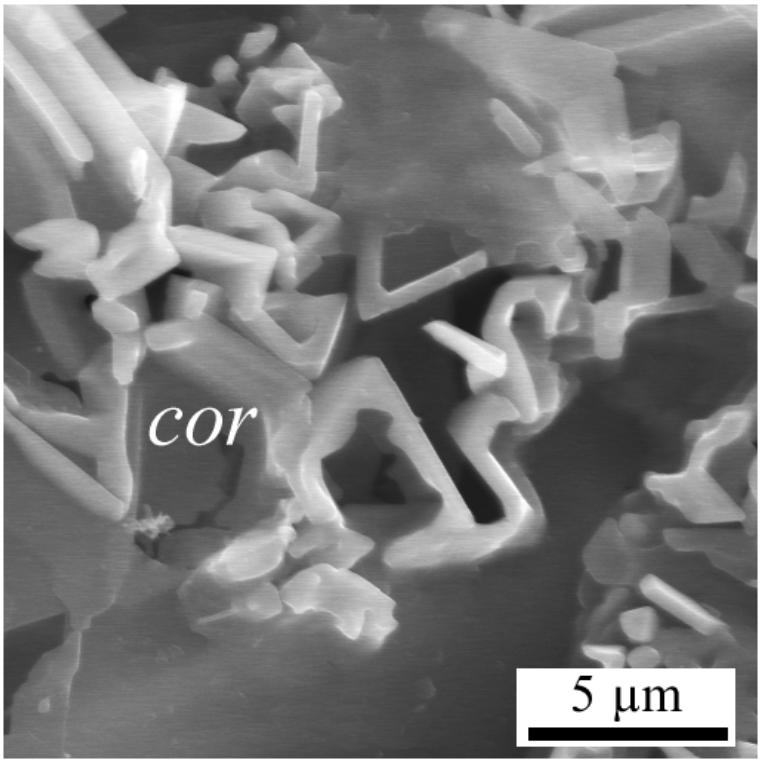

Figure 6.18: SEM image showing skeletal aggregates of corundum in clogging (Sample 58b).

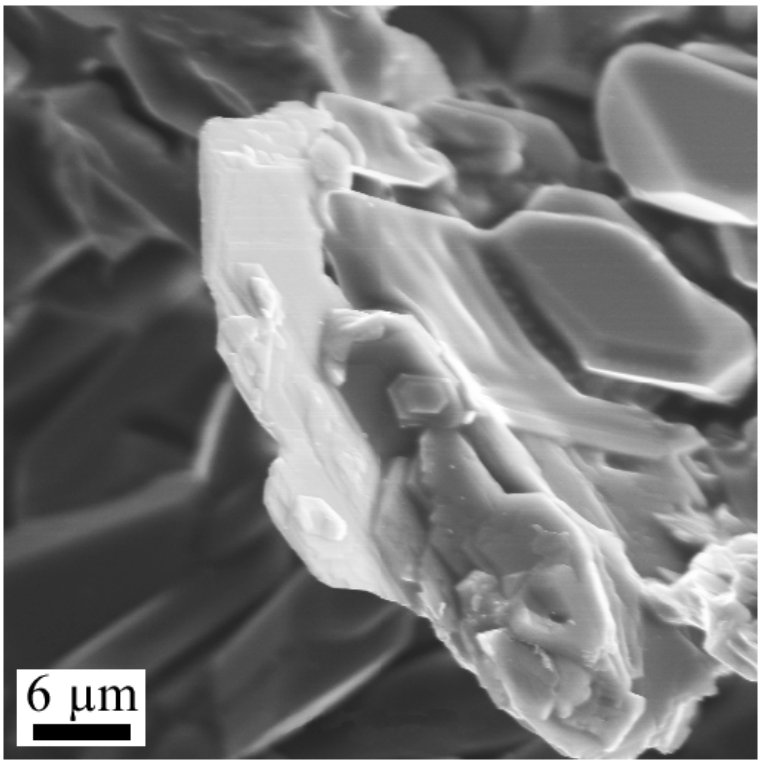

Figure 6.19: SEM image showing platy corundum. Note the hexagonal outline (Sample 58b).

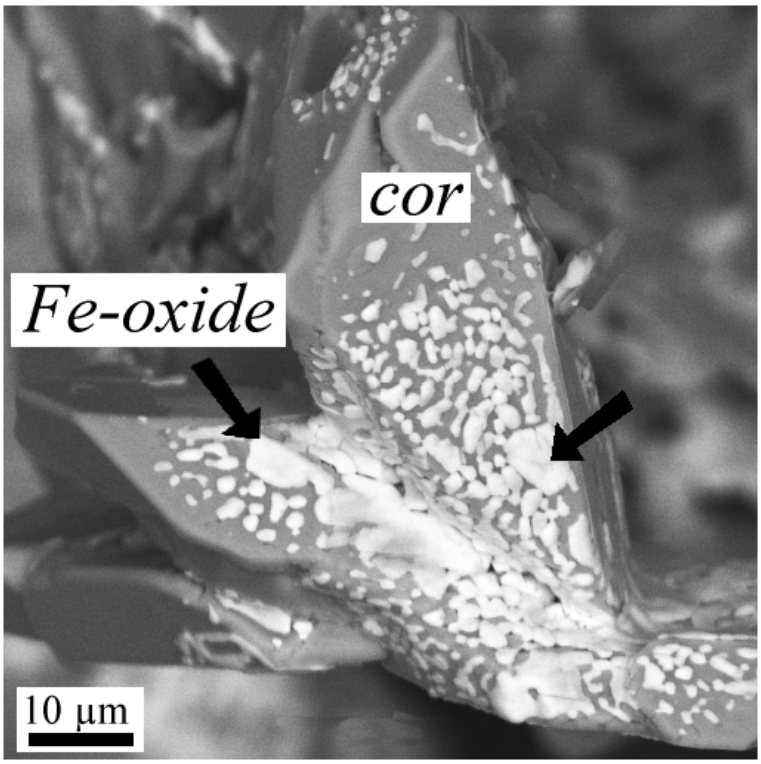

Figure 6.20: SEM showing euhedral corundum crystals. The bright spots on the crystal faces is secondary iron oxide (Sample 58b).

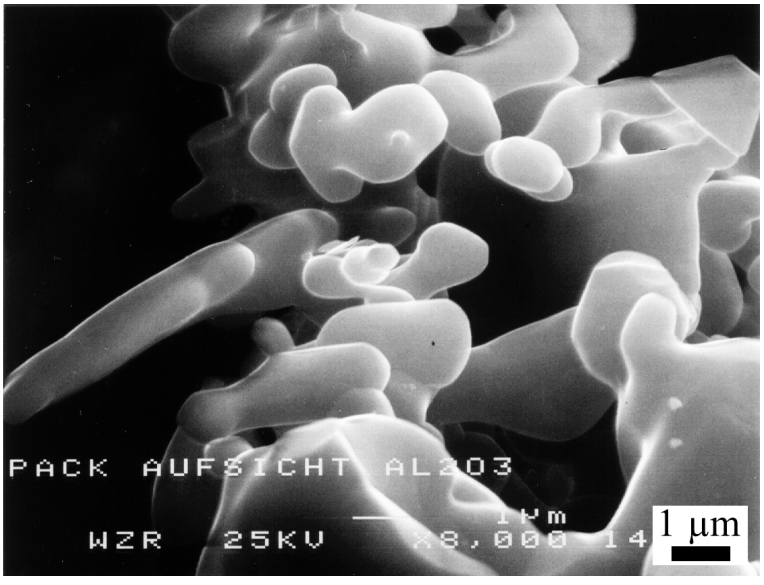

Figure 6.21: SEM image showing well rounded, spongy aggregates of corundum (SEM photomicrograph: *H. Grote*, Werkstoffzentrum Rheinbach GmbH, Sample 63).

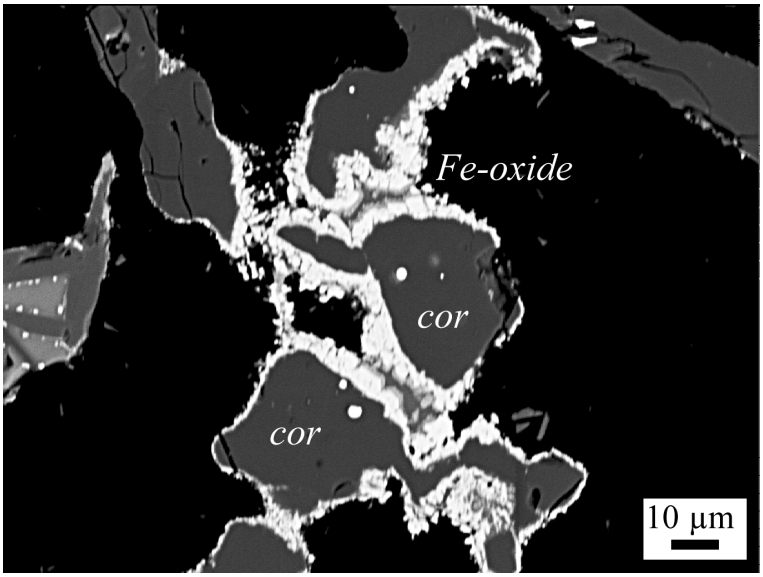

Figure 6.22: BSE image of corundum coverd with iron oxide crusts. These crusts formed during the cooling of the SEN under atmospheric (i. e. oxidizing) conditions (Sample 28).

Corundum occurs in different crystal habits with grain sizes always $<50\,\mu$m. SEM resolved four crystal habits of corundum in the clogging material:

- Skeletal alumina with a structure resembling the outline of medieval citadels (Fig. 6.18)
- Platy alumina (Fig. 6.19)
- Euhedral alumina crystals (Fig. 6.20)
- Spongy aggregates of well rounded alumina grains (Fig.6.21)

Steinmetz et al. (1977) suggested that the habit of oxide inclusion particles can be correlated with the oxygen partial pressure and the concentration of deoxydation metal. At high p_{O_2} and low a_{metal}, small spherules will form. With increasing a_{metal} and decreasing p_{O_2}, dendritic particles predominate the habit. At high a_{metal} and low p_{O_2}, euhedral crystals are expected to form (Steinmetz et al., 1977). McPherson and McLean (1995), however, report the formation of dendritic inclusions in Al-killed steels with oxygen in excess (through reoxidation).

Corundum, displayed in Figure 6.20 would correspond to a milieu of formation enriched in alloyed Al and depleted in oxygen, typical towards the end of the deoxidation process. The rounded alumina particles in Figure 6.21 would have formed at high oxygen partial pressure and low Al-concentration (i. e. at the beginning of the deoxidation process). The schemes suggested by Steinmetz et al. (1977) and McPherson and McLean (1995), however, are valid for inclusions and may not be applicable to the clogging. McPherson and McLean (1995) report that skeletal aggregates of sintered small alumina particles, resembling those displayed in Figure 6.21 are typical for built ups in the bore of the submerged entry nozzles. It is generally accepted that these aggregates form as a result of high temperature sintering of small alumina particles (McPherson and McLean, 1995).

Crusts of iron oxide on the faces of grains of euhedral corundum have probably developed from iron films during cooling under atmospheric conditions (Figs. 6.22, 6.20). In

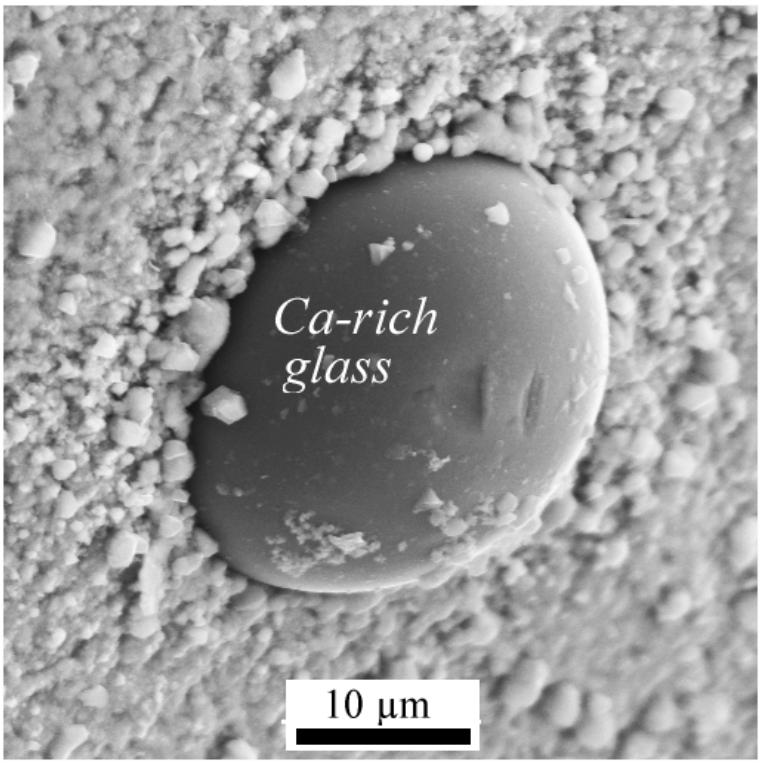

Figure 6.23: SEM image showing Ca-rich glass exsolving out from a droplet of metallic iron (Sample 36).

Table 6.3: Major and minor element composition of a calcium-aluminate-rich glass exsolving out from an iron droplet (Fig. 6.23, EDS analysis, Sample 36)

	wt.%
SiO_2	20
Al_2O_3	30
FeO	6
MnO	3
CaO	37
K_2O	0.4
Na_2O	1.5

Sample 36, CaO-SiO_2-Al_2O_3 glass was observed to exsolve from an iron droplet (Fig. 6.23). The chemical composition of the sphere is listed in Table 6.3.

Spinel occurs exclusively as euhedral grains (octahedra) embedded within a Ca-rich vitreous matrix (Figs. 6.24). It can be easily identified by its ponounced relief caused by the high hardness contrast with the calcium-aluminate-rich matrix. The relief is a product of sample preparation.

Hibonite could not be identified in the clogging samples although X-ray diffraction indicated its occurrence. X-ray maps of clogging, rich in calcium-aluminate matrix, revealed the matrix to be heterogeneous in micrometer scale. It is inferred that the apparent vitreous calcium and aluminium-rich phase contains submicroscopic calcium aluminate phases and gehlenite. Occasionally, skeletal crystals were detected in the calcium-aluminate-rich matrix (Fig. 6.25). These crystals are composed of CaO, Al_2O_3, and SiO_2 in descending order of

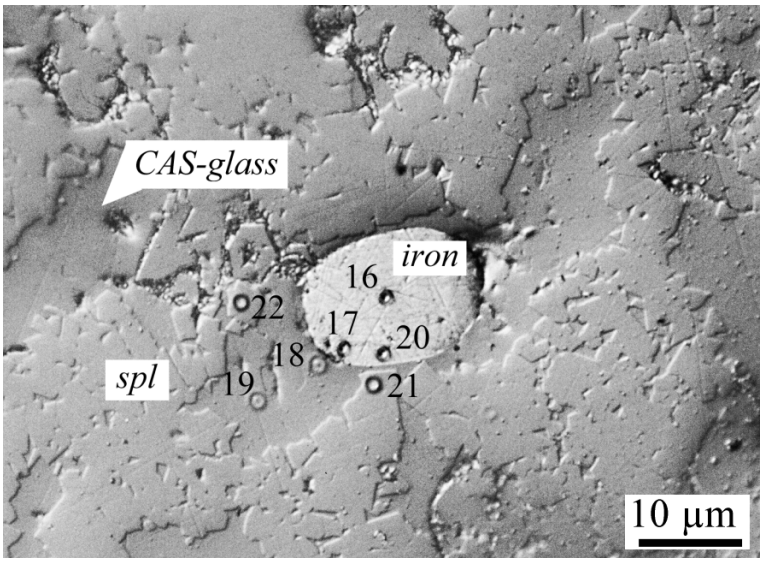

Figure 6.24: Reflected light photomicrograph of spinel sticking out in the calcium-aluminate-rich matrix (Sample 36). Spinel always developed its own habitus (octahedron).

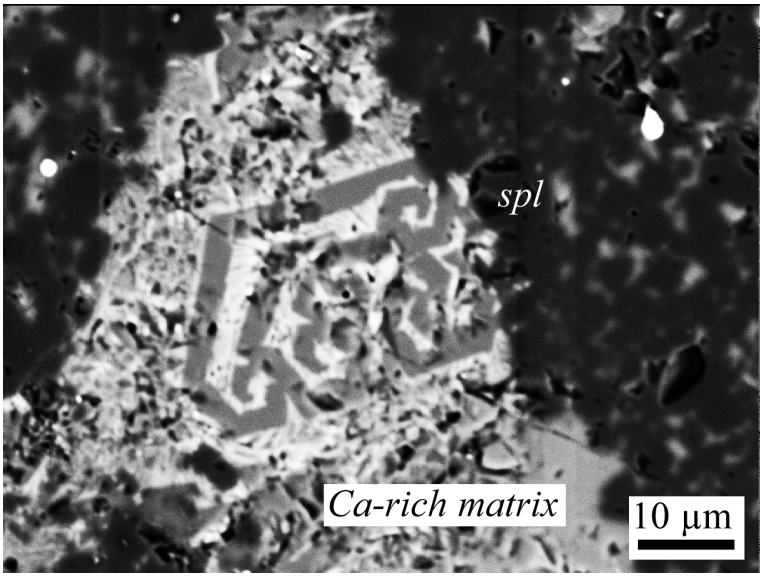

Figure 6.25: BSE image of a skeletal Ca-rich phase crystallizing in the Ca-rich matrix. Spinel appears dark in the image (Sample 48).

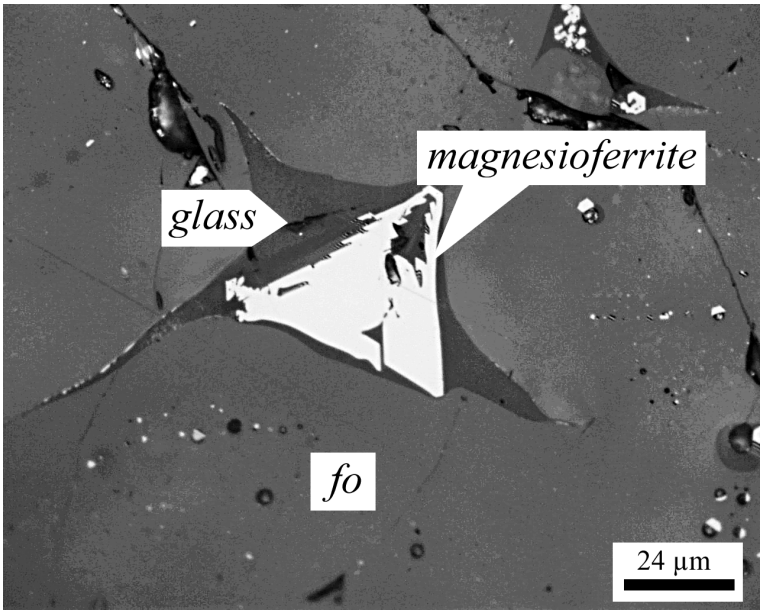

Figure 6.26: BSE image of oxidized olivine (1600°C, 4 h) with segregation of interstitial glass associated with bright magnesioferrite.

concentrations.

6.5 Olivine of the oxidation experiment

Olivine of the raw material used in the tundish lining was heated by Broß (1998, pers. comm.) to temperatures of 800°C and 1600°C, respectively, for 4 h each in a laboratory furnace (atmospheric oxygen partial pressure). Ferrous iron of the olivine is oxidized to ferric iron due to the high oxygen potential in the furnace.

At a firing temperature of 800°C, no major change in the texture of the olivine was observed. The surface of the sample turned in color from greenish to brown due to partial oxidation of ferrous to ferric iron. Microscopically, however, no exsolution of trivalent iron containing minerals was observed and the composition of the olivine was found to be identical with the raw material.

The olivine turned in color from initially greenish through dark brown to black after firing at 1600°C for 4 h. Skeletal magnesioferrite ($MgFe_2^{3+}O_4$) forms and occurs embedded in a glassy phase preferentially along grain boundaries and as interstitial phase (Figs. 6.26, 6.27). The facetted magnesioferrite crystals are up to 50 μm in diameter and their occurence is restricted to the glass. The forsterite host appears homogeneous without any magnesioferrite exsolutions.

The formation of a vitreous phase in the olivine during firing is responsible for a considerable decrease of its mechanical stability at elevated temperatures as described by Koltermann et al. (1985).

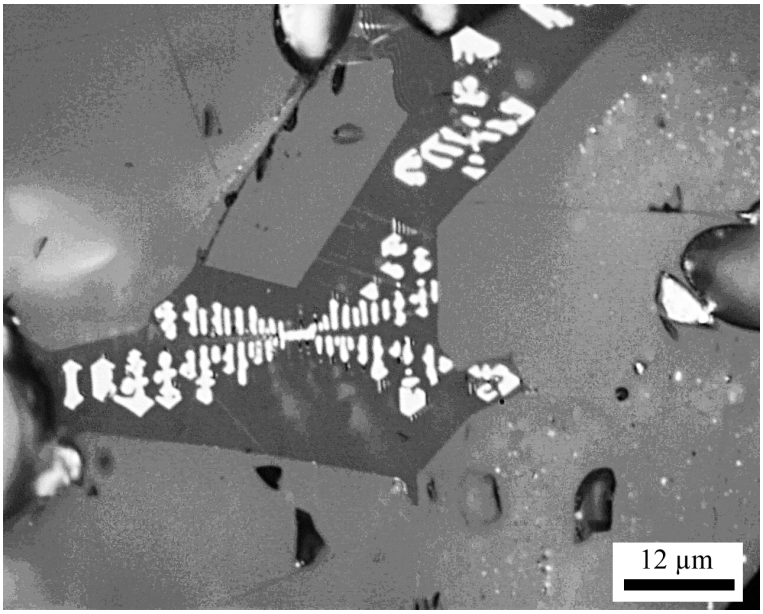

Figure 6.27: BSE image of skeletal magnesioferrite grown in an intersitial glassy matrix.

6.5.1 Andalusite bricks

Three samples of unused andalusite bricks were investigated. Andalusite is used as a raw material for neutral refractories. It is not stable at high temperatures and disintegrates into a submicroscopic composite of mullite and SiO_2.

"Andalusite" brick, sample 116

The disintegration of andalusite is incomplete in sample 116. Small andalusite crystals decomposed entirely to mullite and SiO_2. Large grains, however, are rimmed by the mullite-SiO_2 composite with andalusite being preserved in the core.

Hülsmans et al. (2000a) showed in a detailed TEM study that the transformation of andalusite to mullite starts at the (001) surface and proceeds rapidly along the c-axis of the andalusite. This is shown in Fig. 6.29. The transformation $\|c_{and}$ is by orders of magnitude faster than $\perp c_{and}$. Hülsmans et al. (2000a,b) showed that the reaction product at 1500–1600°C is mullite and non-crystalline silica. Electron diffraction studies showed the following topotactical orientation relationship between the andalusite educt (A) and mullite product (M): $[100]_A \| [010]_M; [010]_A \| [100]_M; [001]_A \| [001]_M$.

"Andalusite" brick, samples 117 and 118

These bricks are composed of angular grains of mullite submicroscopically intergrown with SiO_2 forming pseudomorphs after the former andalusite crystals. The grain size spectrum ranges from a few μm up to greater than 1500 μm. The matrix is composed of very fine-grained mullite intergrown with quartz or vitreous SiO_2. No relicts of andalusite were detected in thin sections of this type of refractory bricks.

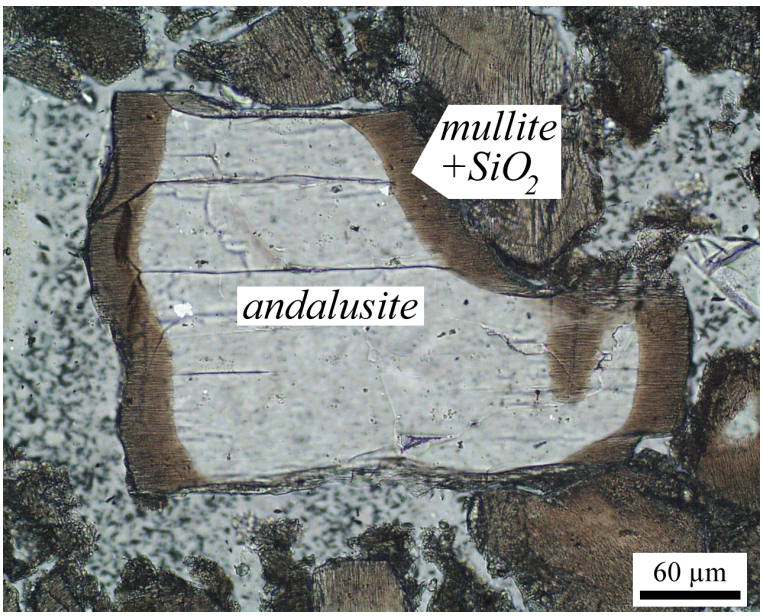

Figure 6.28: Andalusite crystal rimmed with fine grained mullite and SiO_2 (transmitted light photomicrograph, sample 116). Smaller grains are entirely decomposed, whereas large grains show preserve andalusite in the core.

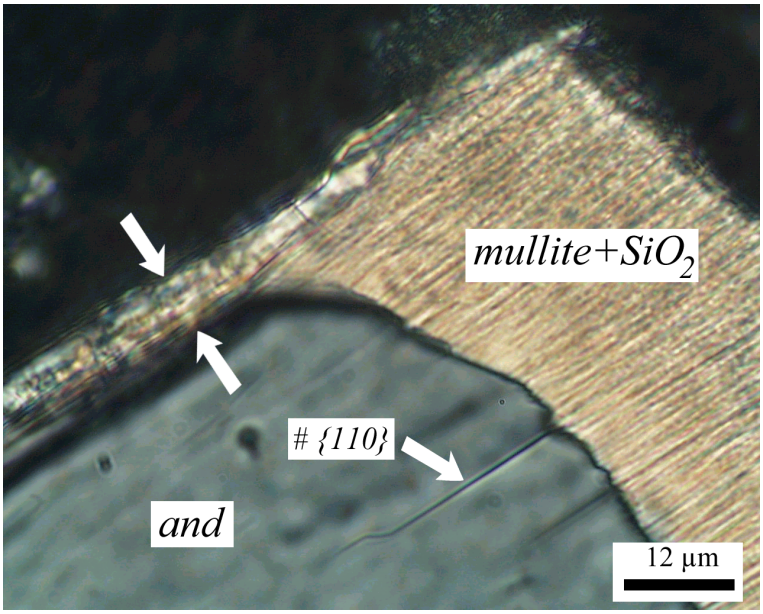

Figure 6.29: Detailed view on the reaction rim (transmitted light photomicrograph, sample 116). The cleavage #{110} is oriented perpendicular to the sections surface.

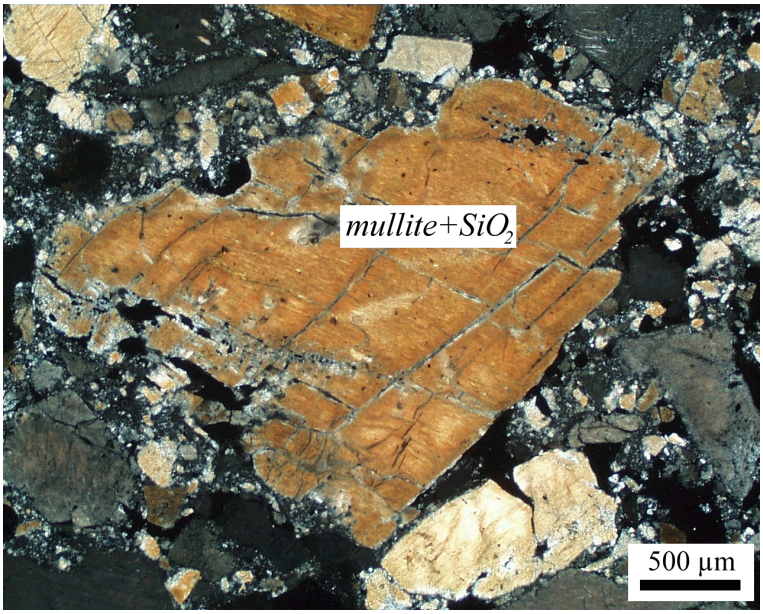

Figure 6.30: Submicroscopic fine-grained mullite and SiO_2 forming pseudomorphs after andalusite (transmitted light photomicrograph, +N, sample 118).

The andalusite brick with remains of andalusite can be regarded to be of lower quality compared to the entirely mullitized refractory bricks.

Chapter 7

Chemistry

7.1 Raw material composition

7.1.1 Raw materials used in the sprayed tundish lining

Olivine

The olivine used in the sprayed tundish lining is a forsterite with 6–8 mol% fayalite component. The chemical composition of the olivine raw material is listed in Table 7.1 (data from Koltermann et al., 1985). The olivine originates from the Åheim dunite deposit.

Table 7.1: Average chemical composition of the olivine raw material (data from Koltermann et al., 1985)

	SiO_2 wt.%	Al_2O_3 wt.%	FeO wt.%	CaO wt.%	MgO wt.%	L.O.I. wt.%	Total wt.%	Mn ppm	Cr ppm	Ni ppm
Olivine	42	0.7	6.4	0.06	49	0.9	98.96	≈1000	≈5900	≈1000

Periclase

The composition of one sample (109) of periclase which has been used as a raw material in the sprayed tundish lining is listed in Table D.1 (p. 143). It is produced from natural magnesite imported from China. The MgO content is 92.95 wt.%. Impurities of SiO_2 (4.77 wt.%), CaO (1.22 wt.%), Al_2O_3 (0.80 wt.%), and Fe_2O_3 (0.76 wt.%) exist. Trace element concentrations are generally very low in the periclase. Notable are contents of ≈200 ppm Cu in all samples of periclase analyzed. The FeO impurity is mainly a result of mining and subsequent production processs (Broß, 1995).

7.1.2 Other periclase raw materials

The chemical compositions of a set of other periclase raw materials used for production of refractory materials were analyzed. Major and trace element compositions are listed in Table D.1 (p. 143). The MgO content varies between 93 and 98 wt.%, respectively. The largest amount of impurities were observed in a Brazilian periclase with 2.34 wt.% Fe_2O_3 and 2.20 wt.% SiO_2. The composition is reflected in the gray color of the sintered pellets.

Sample 110 is a periclase which is produced from brucite precipitated from sea water. It is a periclase product containing 98.34 wt.% MgO and only small amounts of SiO_2 and Fe_2O_3. The trace element concentrations are not distinguishable from that of the periclase which is produced from magnesite.

7.2 Steel composition

The melts casted during sampling (steel pant A) were low alloyed, Al-killed steels. The samples were taken from the ladle during secondary metallurgical treatment. The major, minor and trace element compositions were determined by sparc spectroscopy in steel plant A.

Major alloying components are Mn (0.1–1.3 wt.%), Si (0.01–0.2 wt.%), and C (<0.01–0.2 wt.%). The concentration of Al varies only in a narrow range close to 0.04 wt.%. Figure 7.1 is a ternary plot showing the relative proportions of Si, C, and Mn in the steel melt. The proportions vary only in a relatively narrow range. Figures 7.2 and 7.3 illustrate the relationship between the contents of Mn and C and between Mn and Si, respectively. A tentative correlation between C and Mn, and Si and Mn is indicated. The plots include data obtained during the refinement process.

Based on the chemical composition, two distinct melt types can be distinguished:

- Steel with 0.2–0.4 wt.% Mn
- Steel with 1.2–1.4 wt.% Mn

7.3 Ladle lining

7.3.1 High-alumina castables

One sample of a spinel-forming ladle castable was chemically analyzed (Sample 76a, Tab. D.2, p. 144). It contains 88 wt.% Al_2O_3, 4.9 wt.% MgO, 2.7 wt.% Fe_2O_3 and 2.3 wt.% SiO_2. Trace element contents are generally low.

7.3.2 Basic refractory bricks

Two samples of MgO bricks (74, 100) were analyzed. Annealing of the powdered samples result in a considerable weight loss (11.38 wt.%, Sample 74) corresponding to the amount of

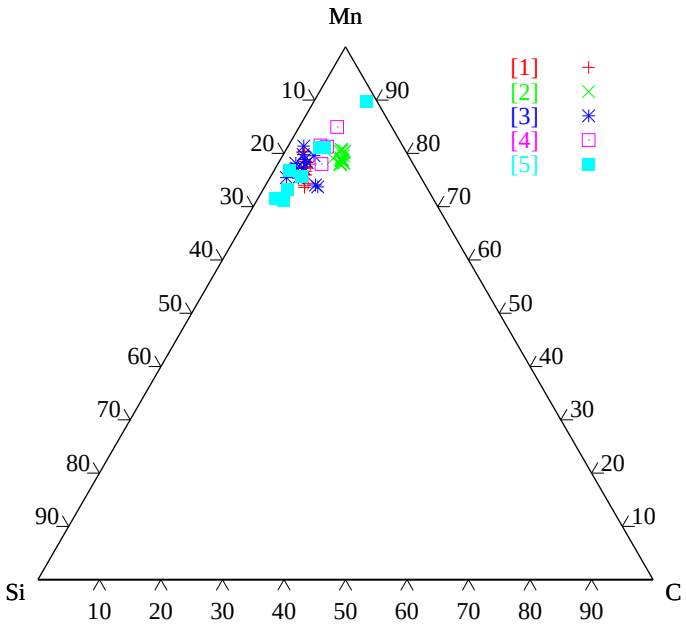

Figure 7.1: Ternary plot illustrating the relative amounts of Si, C, and Mn in weight units. The plot includes data obtained during the refinement process. The samples corresponding to the steel compositions (denoted by the numbers) are listed in Table B.7 (Appendix, p. 140).

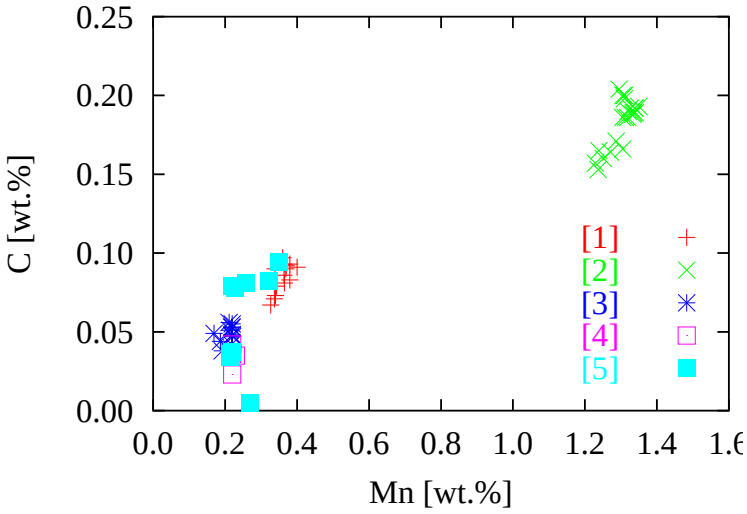

Figure 7.2: Plot of C vs. Mn of steel compositions. High concentrations of Mn correlate with high contents of C. The plot includes data obtained during casting.

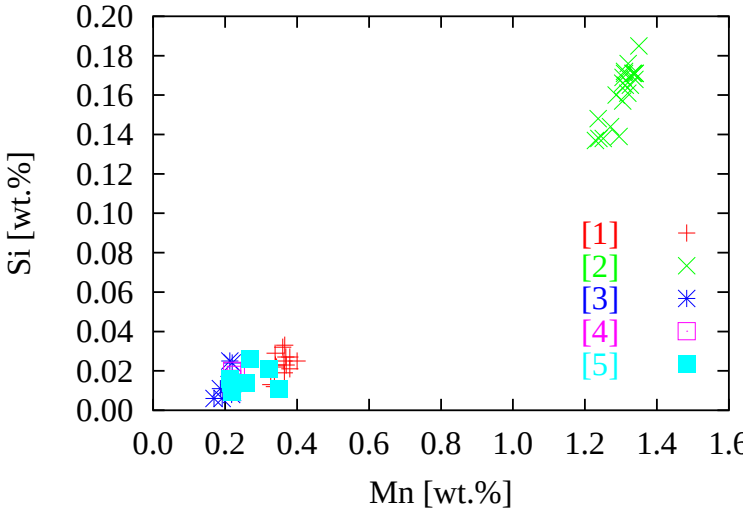

Figure 7.3: Plot of Si vs. Mn of steel compositions. A positive correlation between Si and Mn is indicated. The plot includes data obtained during casting.

C. The composition of the oxide part of the bricks is listed in Table D.3 (p. 144). The MgO content was found to be 95–97 wt.%, respectively. The compositions resemble the compositions of the analyzed periclase raw materials with generally low concentrations of trace elements. One sample of an unused “dolomite” from a different steel plant was analyzed. Apart from CaO and MgO, it contains only a small amounts of SiO_2 (1.4 wt.%, Tab. D.3).

7.4 Ladle slag

The compositions of a set of reduced ladle slag samples were determined by XRF on pressed powder pellets. The preparation of powder pellets was necessary because of considerable content of fluorine. Fluorine is introduced to the slag in the form of CaF_2 as flux. The initial composition of the slag includes notable amounts of Fe (16 wt.% FeO) and Mn (2 wt.% MnO). During steel refinement, reduction of the siderophile elements leads to the loss of these elements to the steel melt. Lithophile elements like Al become enriched in the slag (Fig. 7.4).

The depletion in Fe and Mn, which corresponds to the grade of reduction, appears to be much more pronounced in the slag used in basic ladles than used in neutral lined ladles. The outstanding difference in color (neutral lining: dark colored slag, basic lining: white slag) of the used slag reflects the difference in the amount of Fe and Mn.

The ten times increase in alumina content of the slag is a result of the absorption of up-floating alumina deoxidation particels. MgO is introduced through erosion and corrosion of the basic repair lining.

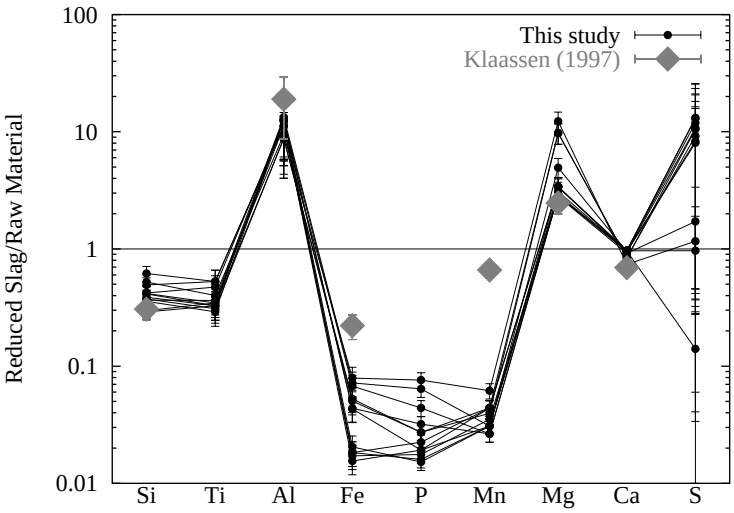

Figure 7.4: Plot illustrating the relative proportions of Si, Ti, Al, Fe, P, Mn, Mg, and Ca compared to the average composition of the slag raw material. Only slag used in basic ladles were sampled. The error bars result from variations in the initial composition of the slag raw material. For comparison, data from Klaassen (1997) for slag used in neutral ladles are plotted.

7.5 Sprayed tundish lining

The bulk chemical composition of the unused sprayed tundish lining is approximately: 18 wt.% SiO_2, 3 wt.% FeO, 75 wt.% MgO, 2 wt.% Al_2O_3 and 1.5 wt.% CaO. The data correspond to the data given by Broß (1995) for the bulk composition of the raw material of the tundish lining (therein referred as *S1*).

The bulk composition of the tundish lining changes towards the contact with the steel melt. Figure 7.5 illustrates the composition of the tundish lining in the ternary diagram SiO_2-Al_2O_3-MgO. The composition of the tundish lining shifts towards the composition field of the tundish slag. This agrees with the observation of slag infiltrating the melt contact of the tundish lining. Any major influence of clogging material on the chemical composition of the ladle lining could not be observed. The chemical composition of the tundish slag, however, is influenced by absorption of inclusion material and material of the tundish lining in the approximate proportion of 2:1.

Pronounced are the enrichments in Al and Mn by factors of 5–7 and 20–70, respectively. Figure 7.6 illustrates the enrichment of compounds of the sprayed tundish lining relative to the composition of the unaltered side.

To prove the hypothesis that the change in composition is the result of admixture of tundish slag with tundish lining, as indicated by microscopy, the model compositions of tundish linings containing 1–50 wt.% of slag components were calculated. The composition of the model slag corresponds to the average composition of the used tundish slag[1].

The compositions of the model linings are plotted relative to the composition of the average unaltered tundish lining (Fig. 7.7). The pattern obtained from analyses of the used tundish lining can be related to admixture of 20–50 wt.% of tundish slag with the tundish lining. This is in good agreement with the results discussed above, which are displayed in Figure 7.5. A maximum degree of contamination is estimated, based on Figure 7.5, to 40%

[1]Due to its extraordinary high TiO_2 concentration, Sample 33 was excluded from the calculation of the average.

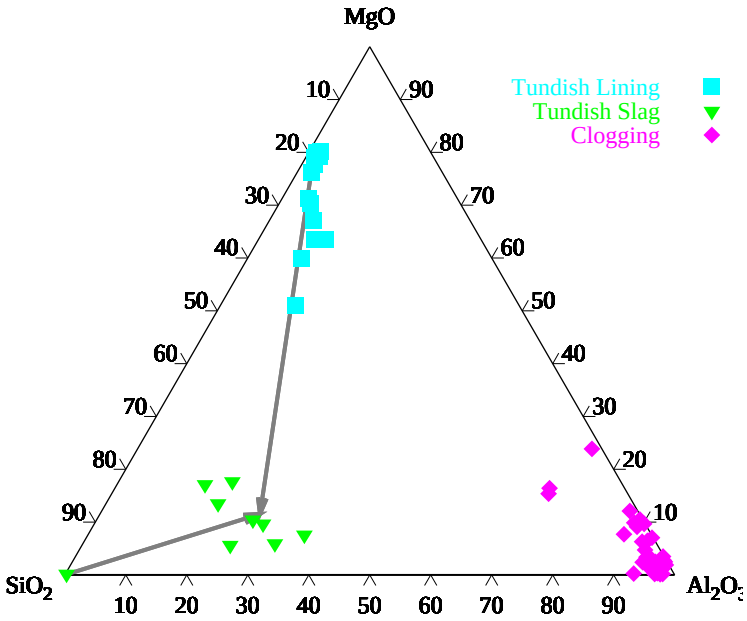

Figure 7.5: Ternary diagram of SiO_2, Al_2O_3, and MgO illustrating the composition of tundish lining, tundish slag, and clogging. The change in composition of the tundish lining is clearly related to admixture with tundish slag. The contribution of oxide inclusions, represented by clogging analyses, is only very small or even absent. The change in composition of the tundish slag, however, may be related to assimilation of oxide inclusion particles and to a minor extent of eroded tundish refractories.

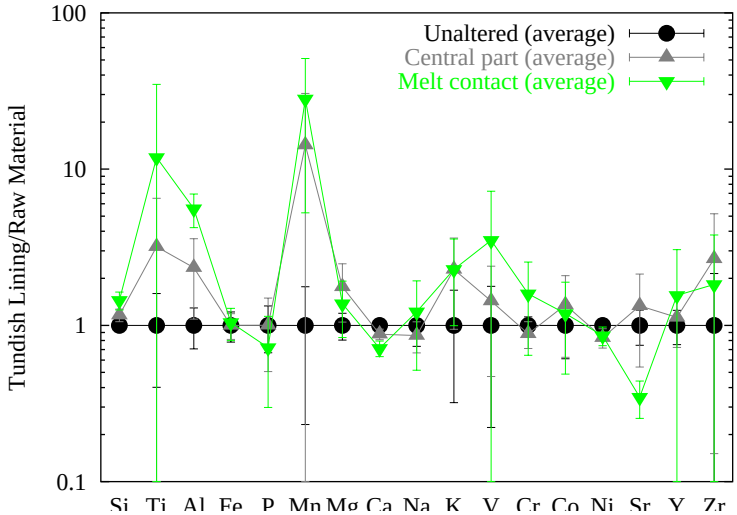

Figure 7.6: Spider diagram illustrating the relative enrichment and depletion of the sprayed tundish lining in various chemical components. The analyses were normalized to the average of the composition of the unaltered side. The largest changes were observed in the melt contact zone.

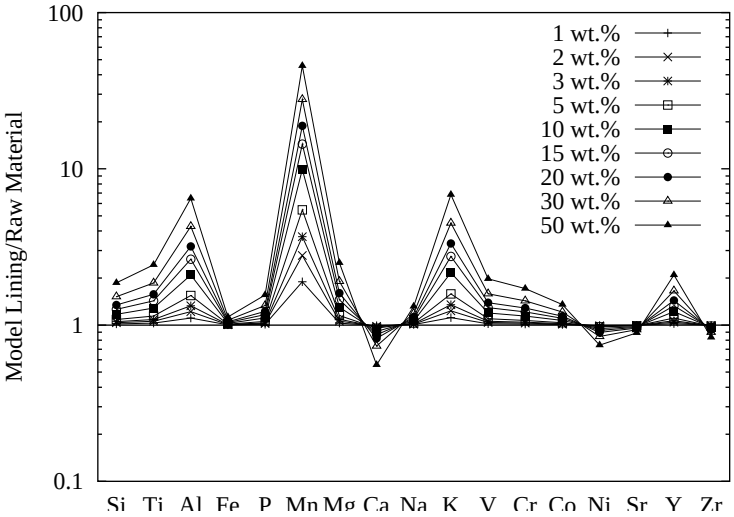

Figure 7.7: Diagram illustrating the composition of a model slag-tundish-lining mixture relative to the average unaltered sprayed tundish lining. The mixture was calculated from data of the average tundish lining (excluding the extremely TiO_2-rich Sample 33) and that of the average unaltered tundish lining.

slag.

No evidence for major elemental exchange between steel melt and tundish lining could be observed since the admixture of the melt covers possible mass transfer between melt and refractory. Microscopic studies support this conclusion. No mass transfer reaction between the steel melt and the basic tundish lining, with the exception of the olivine reduction, was observed.

7.6 Tundish slag

The composition of the raw material used for the tundish slag is nearly pure SiO_2 with 2 wt.% K_2O and 4.8 wt.% C. This composition, however, changes dramatically during casting. Figure 7.8 is a variation diagram to illustrate the relative enrichment of 18 selected chemical components compared to the composition the raw material (Sample 06). The composition undergoes a major change during casting as a result of take up of TiO_2, Al_2O_3, MnO, CaO, MgO, and Na_2O. Some trace elements including V, Cr, Co, Ni, Sr, and Y are also enriched relative to the starting material.

The tundish slag is a mixture of different components. A part of the slag was transferred from the ladle to the tundish. Especially, contents of up to 11 wt.% CaO are attributed to the contribution from ladle slag to the system, since CaO is absent in all parts of the tundish. Alumina is also introduced through transfer from the ladle into the tundish slag. The ratio CaO/Al_2O_3 in the tundish slag varies between 0.21 and 0.82 which is remarkably lower than that in the ladle slag (1–2). This is a strong evidence in favour of assimilation of considerable amounts of alumina particles from the steel melt. Alumina could also be introduced through reduction of components of the slag by alloyed Al.

The ratios of $CaO/(Fe_2O_3 + MnO)$ are in the range of 0.24–1.36. $CaO/(Fe_2O_3 + MnO)$ varies in the ladle slags in the range of $>$5–70, depending on the degree of reduction. This indicates that large amounts of Fe and Mn are released from the steel melt to the tundish

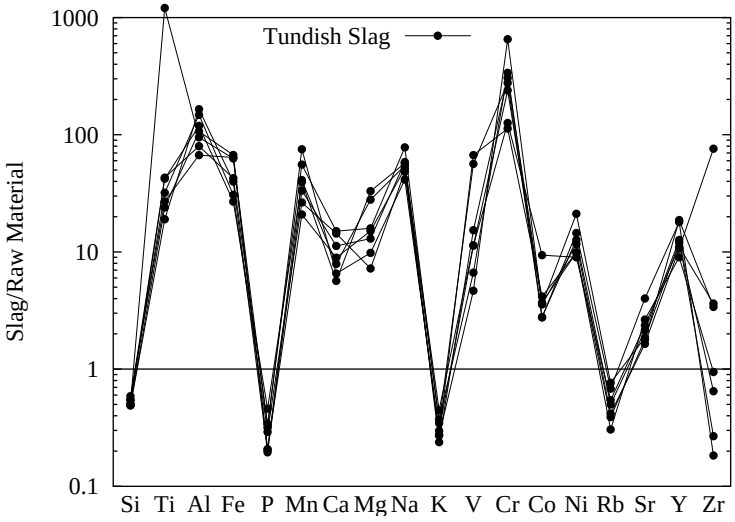

Figure 7.8: Plot of the major element chemistry of the tundish slag samples normalized to the composition of the raw material (Sample 06).

slag. MgO originates from the sprayed tundish lining.

7.7 Clogging

A set of 31 sample of clogging was chemically analyzed. Iron metal was separated from the oxide fraction using a hand magnet. Fine-grained iron metal particles were oxidized during preparation of the fused beads and have been consequently reported as Fe_2O_3. The amount of Fe_2O_3 varies between as much as 60 wt.% and 2.6 wt.%. To make the data more comparable, Fe_2O_3 was subtracted from the analyses and the totals of the oxides were normalized to 100 wt%. Since no phases containing water, sulphur or carbonate occur in the deposits, loss of ignition can be assumed to be zero. Neither were nitrides or carbides indentified. Due to highly reducing conditions, it is inferred that $Fe \gg Fe^{2+} > Fe^{3+}$.

Major compounds are Al_2O_3, MgO, CaO, SiO_2, and Na_2O with minor TiO_2, MnO and ZrO_2. Alumina is the predominant compound in all samples with concentrations varying between 59 and 95 wt.% with most of the samples having alumina contents exceeding 82 wt.%. MgO concentrations vary considerably between <0.5 and 13 wt.% with one exception containing 21 wt.% (Sample 87/2). The variable concentrations of MgO reflect the amount of spinel present in the sample.

CaO contents vary between <0.5 and 14 wt% with most of the samples containing not more than 5 wt.%. Notable are Na_2O concentrations varying between 0.4 and 4 wt%. MnO concentrations never exceed 1.5 wt.%, but are mostly less than 0.6 wt.%.

The composition of clogging can be illustrated in the ternary system Al_2O_3–MgO–SiO_2 (see Fig. 7.5, p. 71). Alumina is the predominant component. Only spinel rich samples are outlined by their high MgO content.

Figures 7.9 and 7.10 are variation diagrams illustrating the relation between major chemical components and Al_2O_3. The data from the bottom side precipitates and from within the inner part of the SEN follow two distinct trend lines in the MgO vs. Al_2O_3 diagram. The

slopes of the trend lines correspond to the MgO/Al_2O_3 ratio in spinel. The intercept at x_0 is a measure for the amount C_i of components other than spinel and corundum ($C_i = 100 - x_i$). However, not all samples follow this trend.

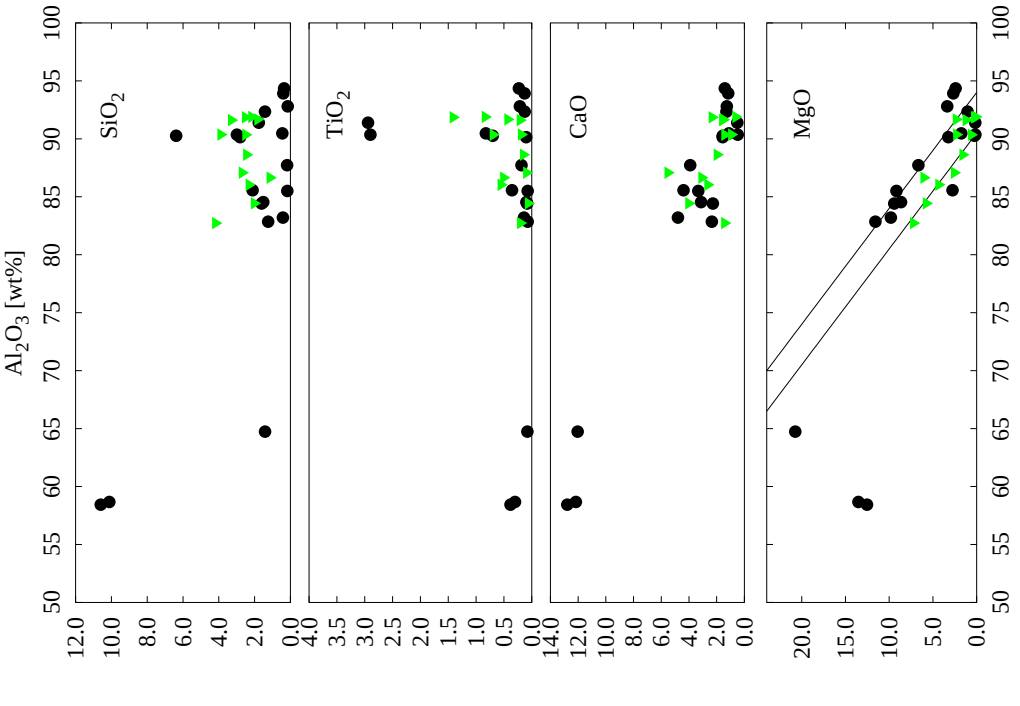

Figure 7.9: Variation diagram of major components (SiO_2, TiO_2, CaO, MgO) plotted vs. Al_2O_3 of clogging samples taken from steel plant A. The concentration of alumina varies between 57 and 95 wt.%. MgO correlates with Al_2O_3 along two distinct trend lines. Triangels: Bottom side precipitates; filled circles: Clogging from the inner part of the SEN.

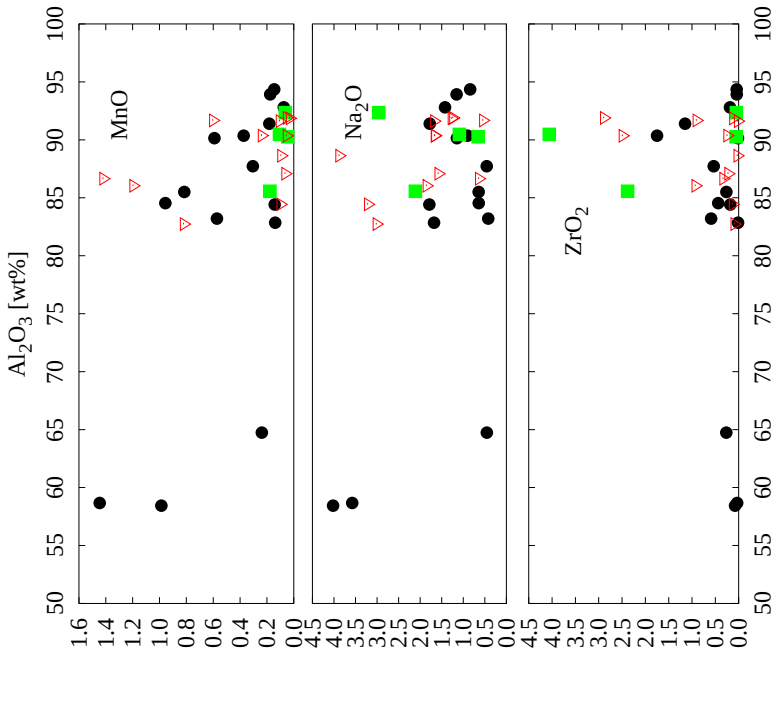

Figure 7.10: Variation diagram of MnO, Na_2O, and ZrO_2 plotted vs. Al_2O_3 from clogging samples from inside the SEN (filled circles) and of bottom side precipitates (triangels). No correlation is indicated.

Chapter 8

Mineral Chemistry

8.1 Ladle refractories

8.1.1 Neutral ladle refractories

Corundum is part of all high alumina refractories. No particular chemical feature were observed. Only MgO ($\leq$0.22 wt.%) and Na_2O ($\leq$0.11 wt.%) were detected in notable amounts. Fe and Cr contents were always below the detection limit of the EPMA.

The spinel analyzed in the high alumina ladle refractories varies in a wide range. The spinel is a *spl-herc* solid solution with $<$1 mol% (Sample 76a), and $<$8 mol% (Sample 101) galaxite component, respectively (Fig. 8.1). The amount of Fe is remarkable and the result of a relatively low degree of reduction in the system refractory-slag in the high-alumina lined ladles[1].

The variations within a single sample are inferred to be a result of local differences in FeO activity reflected in the close association of hercynite and wustite. Consequently, spinel adjacent to or enclosed in calcium aluminates and gehlenite exhibit lower FeO concentrations. The scale of this local heterogeneities is in the range of millimeter to centimeter. The content of galaxite component is generally low and varies between $<$1 mol% and 8 mol%. Cr contents are always in the range of the lower limit of detection of the EPMA. The content of TiO_2 correlates with the concentration of FeO and attains a maximum value of 0.81 wt.% TiO_2.

Calculation of the spinel formula is based on the scheme published by Droop (1987). The presence of ferric iron in the spinel is indicated in the Fe-rich spinel. The maximum ferric iron content was calculated to 0.1 c.p.f. corresponding to 5 mol% magnetite component. A decrease of Fe^{3+}/Fe^{2+} is observed with decreasing Fe content indicating an only negliglible amount of ferric iron in the Fe-poor spinel (Fig. 8.2).

Spinel is closely associated with CA, gehlenite, perovskite and wustite. The compositions of the calcium aluminate phases and perovskite are close to their endmember compositions. Gehlenite in the ladle lining contains Al in excess. Up to 0.25 c.p.f. of Si+(Fe+Mg+Mn)

[1] In case of highly reduced slags, as used in basic ladles, only very little ($<$1 wt.% FeO and $<$0.1 wt.% MnO) amounts of ferrous iron and divalent manganese are present in the slag.

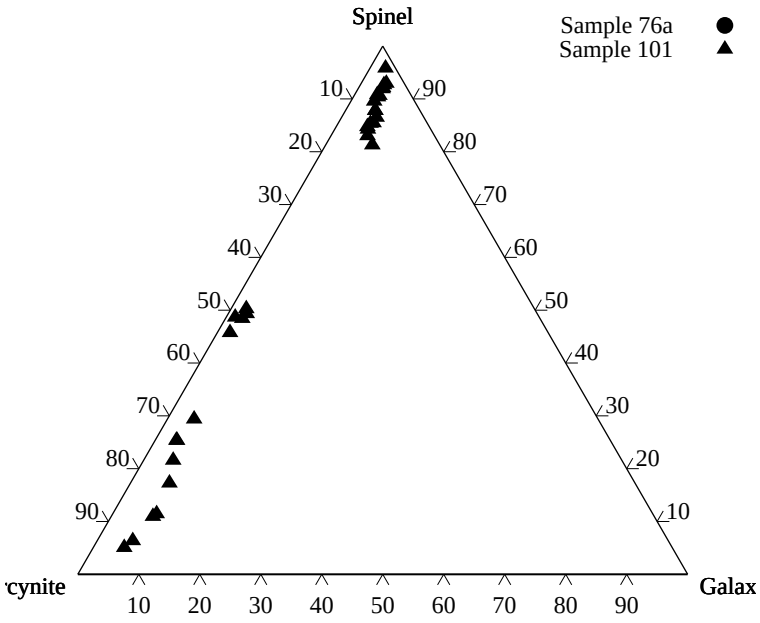

Figure 8.1: Composition of spinel occurring in association with neutral ladle refractories. The composition varies from nearly pure spinel to nearly pure hercynite. Galaxite contents are, in all samples, below 8 mol%. The differences in Fe contents reflect different redox conditions.

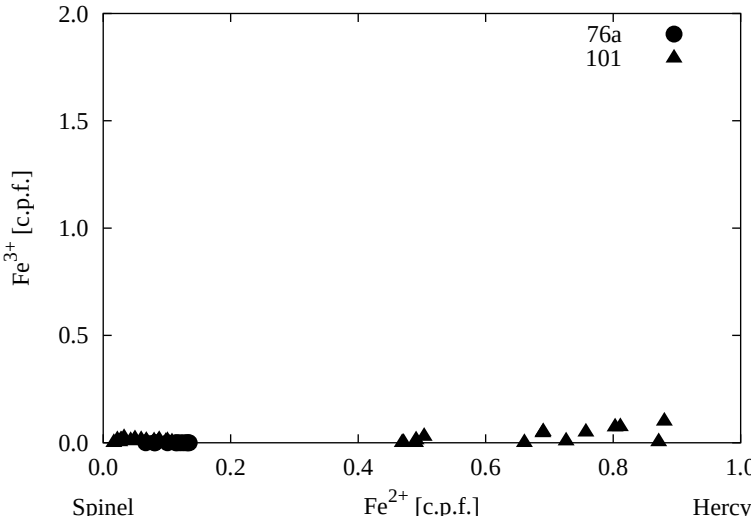

Figure 8.2: Plot of ferric vs. ferrous iron in spinel of the ladle lining indicating the composition of spinel in the system spinel, hercynite, magnetite, and magnesioferrite. An increase of the amount of ferric iron is observed with increasing amount of iron.

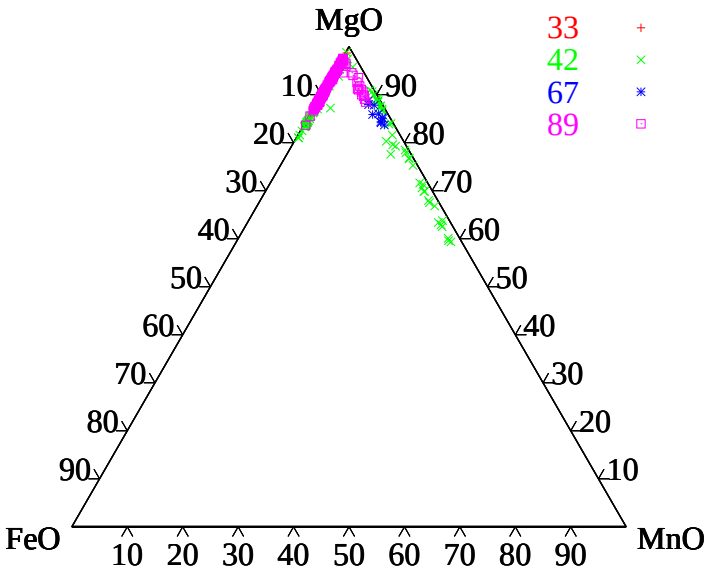

Figure 8.3: Compositional range of olivine in the sprayed tundish lining (Samples 33, 42, and 89) illustrated in the ternary system FeO-MgO-MnO [mol%]. Two exchange pathways can be distinguished: a) Mg_x–Fe_{1-x}, and b) Mg_{1-y}–Mn_y. Analyses with apparent fayalite contents exceeding that of the raw material (6–8 mol%) are interpreted as mixed analyses of olivine and iron metal. All analyses with totals exceeding 101 wt.% were excluded from the data set.

are substituted by 2 Al cations. The average formula of the gehlenite is $Si_{0.80}Ti_{0.06}Al_{2.14}(Fe,Mn,Mg)_{0.14}O_7$. The average formula of wustite is $Fe_{0.87}Mn_{0.05}Mg_{0.03}O$.

8.2 Sprayed tundish lining

8.2.1 Olivine

Three different generations of olivine are to be distinguished in the sprayed tundish lining

- Forsterite of the raw material (colorless, *ol-I*)
- Reduced forsterite (dusty olivine, *ol-II*)
- Tephroitic olivine (*ol-III*)

The olivine of the raw material used in the sprayed tundish lining is forsterite (fa_{4-6}) (Broß, 1995) with only negligible amounts of tephroite ($\leq$0.1 wt.% MnO). Al_2O_3, CaO, and TiO_2 contents were below the detection limits of the EPMA.

During casting, the iron content in the olivine decreases due to reduction of the fayalite component down to values less than 1.5 wt.% FeO (Fig. 8.3). The fayalite reduction is accompanied by exsolution of tiny blebs of iron metal. These exsolution particles are very small in size ($< 1\,\mu$m) and cause a dusty appearance of the olivine in transmitted light.

Because of the dispersed particels of metal, the measurement of the composition of the silicate between the blebs was difficult due to mixed analyses of silicate and metal on micrometer scale using EPMA. Therefore, analyses with totals of the oxides exceeding

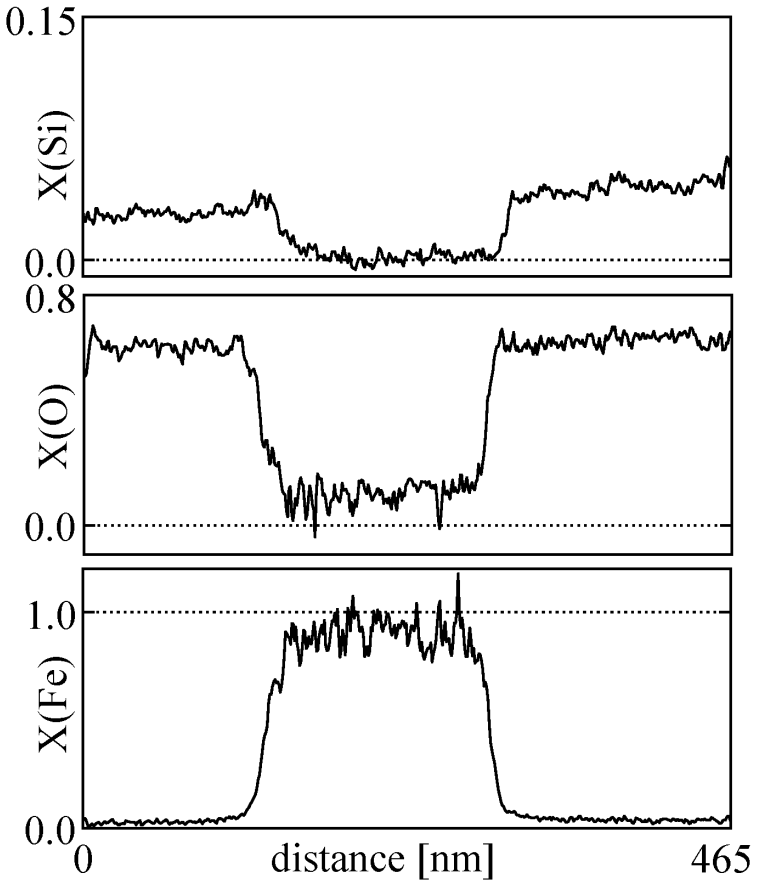

Figure 8.4: TEM EELS profile of Si, Fe, and O measured across an iron metal exsolution bleb.

101 wt.% were excluded from the dataset. Overlapping analyses of olivine host and iron metal, however, cannot be excluded. Figure 8.3 is a ternary diagram illustrating the composition of three olivine generations. The occurrence of an olivine with up to 20 mol% fayalite component is indicated. It is inferred that the high FeO concentrations are an artefact of mixed analyses of forsterite and Fe metal.

TEM EEL-spectroscopy was applied to study the distribution of Fe, Si, and O of a 465 nm profile across an iron metal bleb and the surrounding olivine host (Fig. 8.4). No changes in composition of the olivine towards the contact to the iron metal bleb could be detected. This confirms the observation made by TEM imaging mode that the olivine appears to be undisturbed with regard to lattice defects and chemical composition.

A second generation of olivine is a forsterite-tephroite solid solution with fayalite contents less than 3 mol%. Maximum tephroite contents reach up to 60 mol% (Fig. 8.3). This olivine generation occurs as colorless rims surrounding existing dusty olivine of the first generation, but it also occurs as skeltetal crystals in the glassy slag matrix. It is inferred that the occurrence of the Mn-rich olivine overgrowth is closely related to infiltration of the sprayed tundish lining by tundish slag melt. Concentrations up to 17.5 wt.% of MnO were measured using EPMA in slag which has penetrated the sprayed tundish lining.

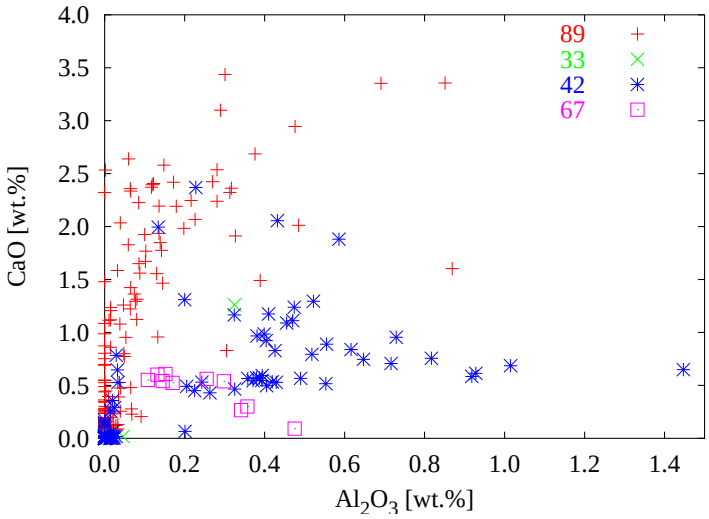

Figure 8.5: Minor element variation plot of CaO vs. Al_2O_3 of olivine in the sprayed tundish lining. Remarkably high concentrations of CaO of up to 3.5 wt.% were detected. Al_2O_3 is generally below 1.0 wt.%. Low concentrations of CaO coincide with low contents of Al_2O_3. No distinct correlation between CaO and Al_2O_3 was observed.

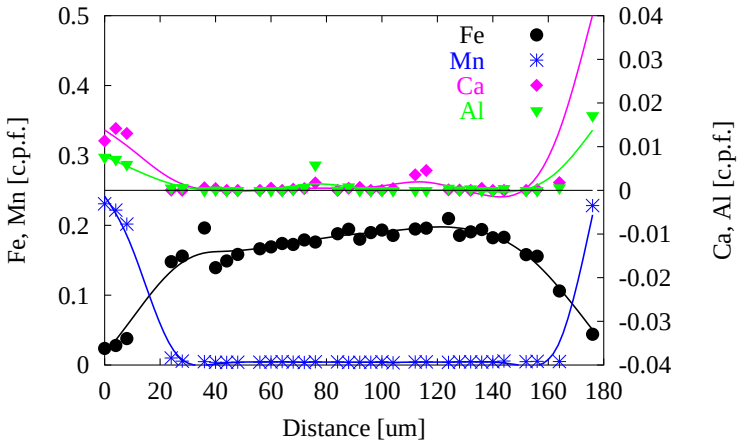

Figure 8.6: Compositional zoning profile across an olivine grain of Fe, Mn, Ca, and Al (Sample 42). The olivine is rimmed by a Mn-rich overgrowth and is, to the right hand, in contact with a steel droplet.

During casting, an increase in contents of refractory components like CaO and Al_2O_3 can be observed in the olivine. CaO varies between zero and 3.5 wt.% and Al_2O_3 between zero and 1.5 wt.%, respectively (Fig. 8.5). Low CaO contents coincide with low Al_2O_3 concentrations, but no systematic correlation between CaO and Al_2O_3 was observed. TiO_2 and Cr_2O_3 concentrations were generally in the range or even below the detection limit of the EPMA (<0.01 wt.%).

Element zonation profiles were measured in different grains of dusty olivine. Figures 8.6 and 8.7 show the distribution of Fe, Mn, Al, and Ca in two different grains of reduced olivine. The grains are rimmed by a Mn-rich olivine overgrowth. In both cases a decrease in Fe is observed towards the Mn-rich overgrowth, whereas the concentrations of Mn and the refractory components (Ca, Al) increase towards the rim. The grain which composition is displayed in Figure 8.6 is less reduced than that which composition is displayed in Figure 8.7. Depending on the degree of reduction, the core reflects the composition of the raw material

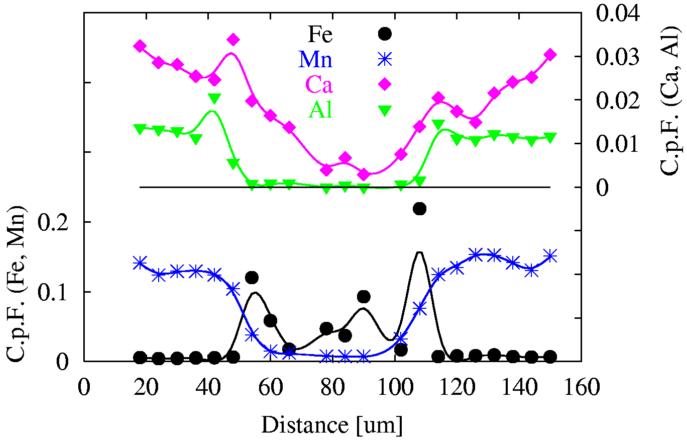

Figure 8.7: Electron microprobe profiles of Ca, Al, Fe, and Mn across the olivine grain (Sample 42). The core is poor in Mn, Ca and Al, whereas the rim is enriched in these elements. The scatter of Fe in the core is caused by mixed analyses of olivine and metal droplets. The lowest values of Fe are in the range of 0.02 c.p.f. (Fo_{99}).

(Fig. 8.6) or depletion in Fe due to reduction of the fayalite component (Fig. 8.7).

8.2.2 Spinel

One single population of spinel was observed in and adjacent to the sprayed tundish lining. It is a binary solid solution between spinel and galaxite ($MnAl_2O_4$) with galaxite contents varying between <2 and 20 mol%, respectively (Fig. 8.8). Fe was assumed to be only in reduced divalent state. FeO-contents between 0.3 and 1.6 wt.%, respectively, were too low to estimate the Fe^{3+}/Fe^{2+} ratio based on EPM-analyses alone using the methods described by Droop (1987).

The hercynite content of the spinel is generally very low and never exceeds 3.5 mol%. The compositional variation of the spinel is less than observed in the newly formed olivine, but follows the same trend on the tie line between the Mg and the Mn end member. This, however, is not surprising because both occur closely associated within a Mn-rich glass matrix. Both, olivine and spinel, have in common low concentrations of iron as a result of strongly reducing conditions. Concentrations of Cr_2O_3 measured in the spinel vary in the range of 0.1–4 wt.%.

8.2.3 Periclase

Periclase is very sensitive to hydration during preparation of polished sections. The option of preparing the polished sections using petroleum instead of water was abandoned. A number of analyses of periclase from an identical refractory altered under the same conditions were published by Broß (1995)[2].

Periclase becomes enriched in Fe and Mn during casting. This increase is displayed by a change in color from colorless to reddish brown. Broß (1995) has measured a profile from

[2]The refractory is therein termed *S1*

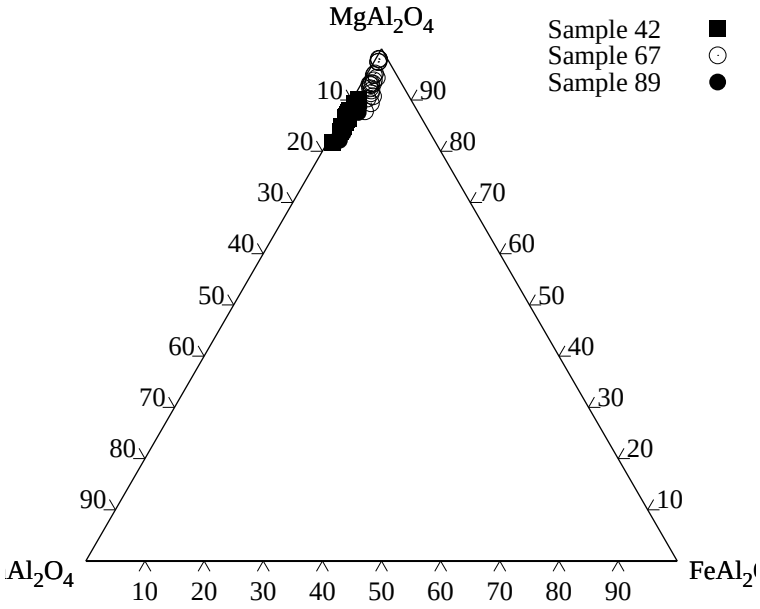

Figure 8.8: Compositional range of spinel in the tundish lining plotted in the ternary system *spl–herc–galax*.

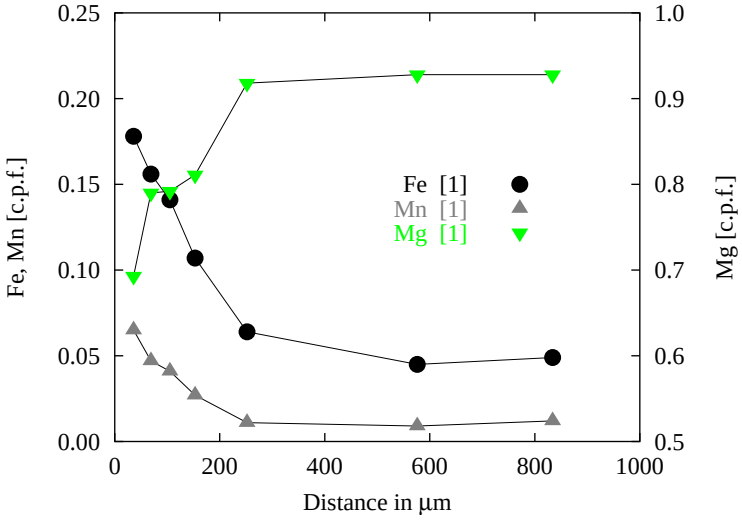

Figure 8.9: Plot of Fe and Mn (c.p.f.) vs. the distance from the rim of a large periclase aggregate in the intermediate zone (data from Broß, 1995). Fe and Mn increase towards the rim accompanied by a parallel decrease of Mg. Maximum values for the Fe and Mn content can be estimated by extrapolation the profile to the outer rim to 0.2 and 0.075 c.p.f., respectively.

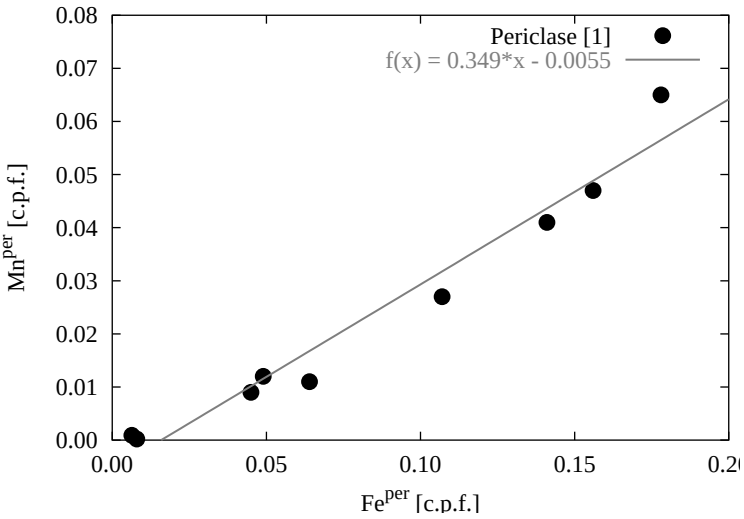

Figure 8.10: Plot of Mn vs. Fe (c.p.f.) of periclase analyses (data from Broß, 1995, 1). The average Mn/Fe ratio is calculated by linear regression analysis to 0.35 ± 0.03.

the core to the rim of a large periclase aggregate in the intermediate zone of the sprayed tundish lining. Both, Fe and Mn increase towards the rim and replace Mg (Fig. 8.9). The shape of the profile indicates a diffusive exchange. The molar Fe/Mn ratio remains, however, constant (0.35 ± 0.03) during that cation exchange (Fig 8.10). Notable is the coexistence of Fe and Mn rich periclase with Fe poor forsterite in the intermediate zone. Maximum values of 0.18 c.p.f. and 0.06 c.p.f. Fe^{2+} and Mn^{2+}, respectively, were measured by Broß (1995).

8.2.4 Glass

Infiltration of glass of the tundish slag was observed in all samples of the sprayed tundish lining. The glass is composed of a variety of oxides including (in descending order) SiO_2 (38–55 wt.%), Al_2O_3 (18–25 wt.%), MnO (6–18 wt.%), CaO (8–17 wt.%), and MgO (2–12 wt.%). Remarkable are the high concentrations of MnO in the tundish slag. The composition of the vitreous slag is quite heterogeneous on millimeter scale as consequence of the schlieren texture.

8.3 Clogging

8.3.1 Corundum

Only a minor substitution of Al by other cations was observed. Figure 8.11 shows the small extent of substitution of Al by foreign cations with a maximum less than 0.1 c.p.f. of ($Si + Ti + Cr + Fe + Mn + Ca + Mg$). Although the extent of substitution is very small, a distinct trend can be outlined (Fig. 8.11).

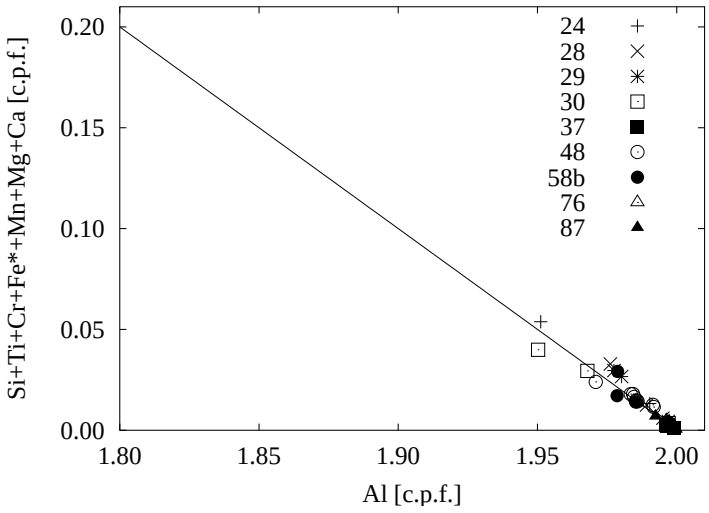

Figure 8.11: Diagram of (Si + Ti + Cr + Fe + Mn + Ca + Mg) (c.p.f.) plotted vs. Al (c.p.f.) of corundum EPM-analyses in clogging. Although the extent of substitution is very small, a distinct trend was observed. The calculation of the Fe^{2+}/Fe^{3+} ratio in the corundum failed most probably due to the uncertainty of the EPMA. The line marks a hypothetical 1:1 substitutional trend line.

8.3.2 Spinel

The spinel in the clogging is essentially a ternary solid solution of spinel, hercynite (<1–80 mol%), and galaxite (<1–20 mol%). Figure 8.12 is a ternary plot (*spl*, *herc*, *galax*) illustrating the end member composition of spinel in the clogging. The majority of the analyzed grains of spinel are close to the composition of MA-spinel. The concentration of Cr_2O_3 was generally below 0.08 wt.%.

The calculation with only ferrous iron in the structure leads to deficits on the position occupied by trivalent cations and an excess of divalent cations. Calculation of the ferrous to ferric iron ratio after Droop (1987) results in amounts of ferric iron up to 0.4 c.p.f. (Fig. 8.13). Secondary oxidation processes may be responsible for the presence of ferric iron clogging. Sample 48 contains notable amounts of hematite, which is clearly a product of secondary oxidation during cooling of the SEN on air.

8.3.3 CAS matrix

In most of the clogging samples a non-stoichiometric phase composed of SiO_2 (12–35 wt.%), Al_2O_3 (3–52 wt.%), CaO (12–56 wt.%), Na_2O (<1–10 wt.%), and MgO (<0.5–6 wt.%) was observed. The composition is illustrated in the ternary system CaO-Al_2O_3-SiO_2 (Fig. 8.14). With exception of two analyzed points (sample 48), all analyzed compositions are liquid at temperatures of 1600°C. The calculation of a mineral formula on basis of different oxygen numbers failed since the CAS matrix represents a quenched melt. Only one analyzed point (sample 88) was identified to be CA_2.

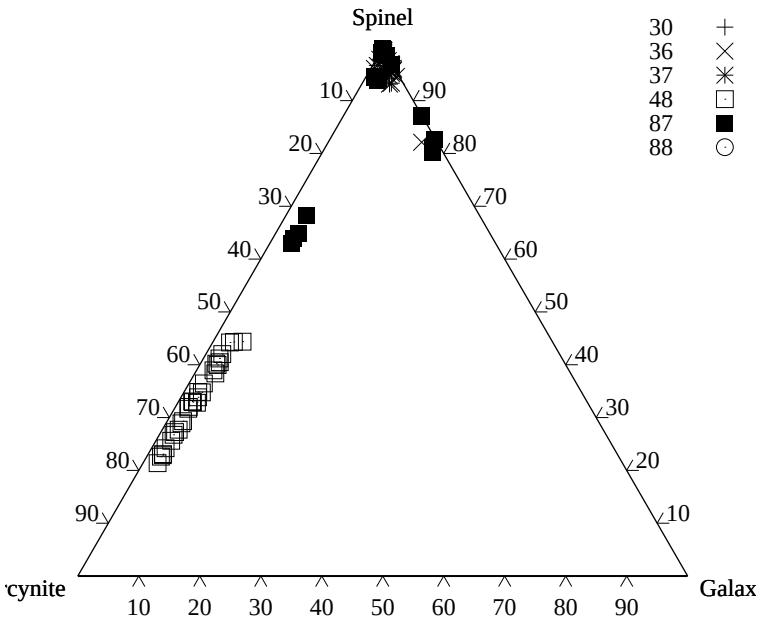

Figure 8.12: Composition of spinel in clogging illustrated in the ternary diagram *herc-galax-spl*. Note the highly variable contents of hercynite in some of the spinels.

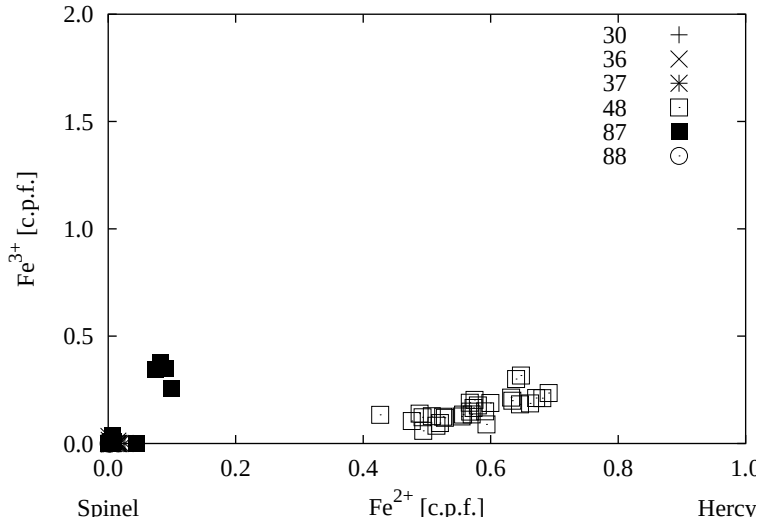

Figure 8.13: Plot of Fe^{3+} (c.p.f.) vs. Fe^{2+} (c.p.f.) of spinel analyses of clogging samples. The majority of the analysed samples contain relatively pure Mg-Al spinel with minor amounts of galaxite component (Fig. 8.12). Notable are contents of up to 70 mol% hercynite (Sample 48) and up to 20 mol% magnesioferrite (Sample 87).

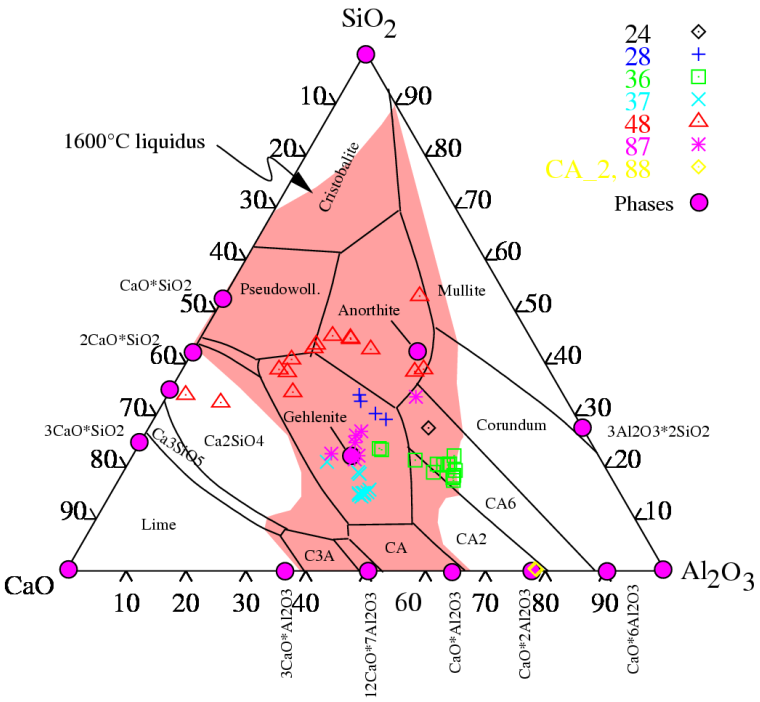

Figure 8.14: Ternary diagram illustrating the composition of the CAS-phase. The diagram shows that, with exception of two analyzed points (sample 48), all analyzed compositions are liquid at 1600°C. The data points fall into the primary fields of gehlenite, anorthite, CA_2 and CA_6. Only one analyzed point (sample 88) was identified to be CA_2 (phase diagram from Levin et al., 1964).

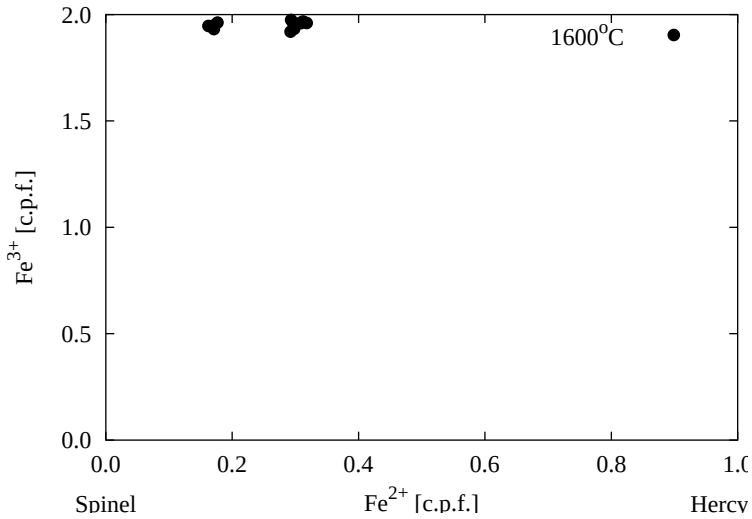

Figure 8.15: Plot of ferric vs. ferrous iron (c.p.f.) of magnesioferrite analyses of the oxidized olivine raw material (1600°C, 4 h).

8.4 Oxidized olivine

The Åheim olivine raw material was fired by R. Broß to study the high temperature behavior of olivine, especially the oxidation process. One sample was fired in an electrical furnace for 4 h at a temperature of 800°C and a second sample for the same time at 1600°C. The atmosphere was in both experiments was oxidizing ($p_{O_2} = 0.21$ bar, air). The olivine samples fired at 800°C did not exhibit any changes in composition.

At a firing temperature of 1600°C, the olivine underwent major compositional and textural changes. The ferrous iron in the olivine was oxidized to ferric iron forming a magnesioferrite-magnetite solid solution and glass. The fayalite content in the olivine dropped due to oxidation of the ferrous iron from initially 6–8 mol% to concentrations between 1.3 and 3.9 mol%.

The composition of the magnesioferrite is illustrated in Fig. 8.15. The glass is strongly enriched in, with respect to olivine incompatible oxides like Al_2O_3 (5.6 wt.%), CaO (5.2 wt.%), TiO_2 (0.15 wt.%), and Na_2O and K_2O (3.8 wt.%).

Chapter 9

Stable oxygen isotope chemistry

9.1 Steel plant A and B

9.1.1 Atmospheric oxygen

The earth's atmosphere is composed of 78.10 vol.% N_2, 20.93 vol.% O_2, 0.93 vol.% Ar and 0.03 vol.% CO_2. The $\delta^{18}O$ value of atmospheric oxygen can be regarded to be world-wide +23.5‰ (Dole et al., 1954).

9.2 Basic oxygen furnace process (BOF) oxygen

Huge amounts of oxygen are consumed in the basic oxygen furnace process to remove carbon from the raw iron. Therefore, an oxygen plant is usually part of each steel plant. One sample of BOF oxygen was taken in the oxygen plant of steel pant A and one sample was available from steel plant B. The oxygen was converted to CO_2 over hot graphite. The CO_2 was analyzed conventionally in a dual inlet gas mass spectrometer.

A $\delta^{18}O$ value of +24.3‰ was obtained from steel plant A and of +25.5‰ from steel plant B.

Oxygen gas is produced from air with the Linde air liquefaction process. The difference in $\delta^{18}O$ between atmospheric oxygen and the BOF process oxygen can be due to two reasons:

1. Atmospheric oxygen is not 100% liquefied. As a result of mass dependent fractionation during the liquefaction process, the $\delta^{18}O$ value of the final oxygen product differs from that of atmospheric oxygen.

2. The entire air oxygen is liquefied but a part of the oxygen is sold as bottle oxygen to laboratories or for welding. Oxygen grade 5.5 (*Air Products*) which is used as laboratory gas reference has a $\delta^{18}O$ of +7.48‰. Assuming that a fraction of isotopically "light" oxygen is sold in bottles, an enrichment of the BOF process oxygen in ^{18}O relative to air oxygen is conclusive.

Table 9.1: Oxygen isotope composition of the periclase raw material used in the sprayed tundish lining

A-325	+14.2‰
A-329	+13.3‰
A-334	+13.7‰
Average	+13.7‰

The small difference in $\delta^{18}O$ of $\leq$1‰ between atmospheric and BOF process oxygen will prevent distiction between these two possible oxygen sources.

9.2.1 Olivine of the sprayed tundish lining

The oxygen isotopic composition of the mantle olivine, which is used as raw material in the tundish lining can be regarded as uniform. Mattey et al. (1994) found a value of +5.2‰ and Wiechert et al. (1996) +5.41$\pm$0.18‰ in olivine of upper mantle rocks. Larger variations found in previous works can be largely attributed to analytical problems rather than to actual heterogeneities (Hoefs, 1996). A value of +5.3‰ is reasonable for the olivine raw material.

Heating of the olivine raw material to temperatures of 800°C and 1600°C (4 h) resulted in oxidation of a part of the fayalite component. An increase in $\delta^{18}O$ in the olivine was observed. At 800°C only a little shift in $\delta^{18}O$ of +0.7‰ was observed. At 1600°C extensive reaction of the olivine to forsterite, magnesioferrite and glass is mirrored in a shift in $\delta^{18}O$ in the order of +3.3‰ to +8.6‰.

9.2.2 Periclase of the sprayed tundish lining

Three samples of the periclase raw material used in the sprayed tundish lining were isotopically characterized. The results are listed in Table 9.1.

The variation of 0.9‰ between samples A-325 and A-334 may be attributed to heterogeneities in the raw material. Contribution of analytical errors, however, cannot be excluded. For the periclase raw material used in the tundish lining, a value of +13.7‰ seems reasonable.

9.2.3 "Bulk" sprayed tundish lining

11 oxygen isotope analyses were conducted on bulk samples of the sprayed tundish lining of the three different zones. The unaltered side is uniform in composition with a mean value of +12.0‰. The $\delta^{18}O$ value increases towards the steel melt contact zone to values up to 16.0‰. The increase is most probably related to infiltration of "heavy" slag component, as indicated by the chemical composition. Mass balance calculation based on the isotope data of the raw material (olivine: +5.3‰, periclase: +13.7‰) indicates that the unaltered side of the tundish lining appears to be slightly enriched in ^{18}O ($\Delta^{18}O_{observed-calculated}$ = +1.2‰) compared to the calculated model composition of the lining (Eqn. 9.1).

$$\delta^{18}O_{Model} = 0.33 \times 5.3 + 0.66 \times 13.7 = +10.8 \; permil \tag{9.1}$$

The difference between calculated (+10.8‰) and measured δ^{18}O value (+12.0‰) is only very small and is within the uncertainty of the measurement. It will be shown that periclase is not isotopically homogeneous. Thus heterogeneities of the periclase and/or contribution of not measured additional components (binder) are most probably responsible for the difference between calculated and measured δ^{18}O value of the unaltered tundish lining.

9.3 Steel plant A

9.3.1 Ladle refractories

Corundum refractories

Due to difficulties during sampling, only a few and most probably not representative hand specimens were taken from ladle refractories. Two types of refractories are to be distinguished:

- Neutral refractories composed of raw materials of the system andalusite, bauxite, corundum, and spinel
- Basic refractories of the system periclase, lime, and carbon

A single sample of a high-alumina neutral tundish lining was investigated in detail with respect to its oxygen isotopic composition. The sample comprises large grains of corundum embedded in a white fine-grained matrix. Dark veinlets and a dark zone along the steel melt contact outline the interaction between steel melt and tundish slag. A set of 13 samples was taken from a single hand specimen using a micro core drill (Ø1 mm i. d., Fig. 9.1). In Table 9.2, the isotope analyses are listed. Apart of the samples indicated in Figure 9.1, two additional samples separated from sample 101 were isotopically characterized. These samples are denoted 101/14 and 101/15. The oxygen isotopic composition of these two samples is also listed in Table 9.2.

Only a small variation in δ^{18}O between +18.1‰ and 20.3‰ is observed for different corundum grains. The dark veinlet infill and the dark contact zone is characterized by slightly lower δ^{18}O varying between +17.8‰ and +18.6‰. A value of +18.6±0.8‰ can be taken as an average for this type of ladle refractory.

Basic ladle linings

Only a single sample of a MgO-C brick was taken during the sampling campaign (Sample 74/1). Periclase was separated and a δ^{18}O value of +17.3‰ was obtained.

9.3.2 Slag

Tundish slag

The tundish slag used at steel plant A is the ash of rice pealing. Silica and carbon are the major constituents. Silica was separated from adjacent carbon and was measured to have

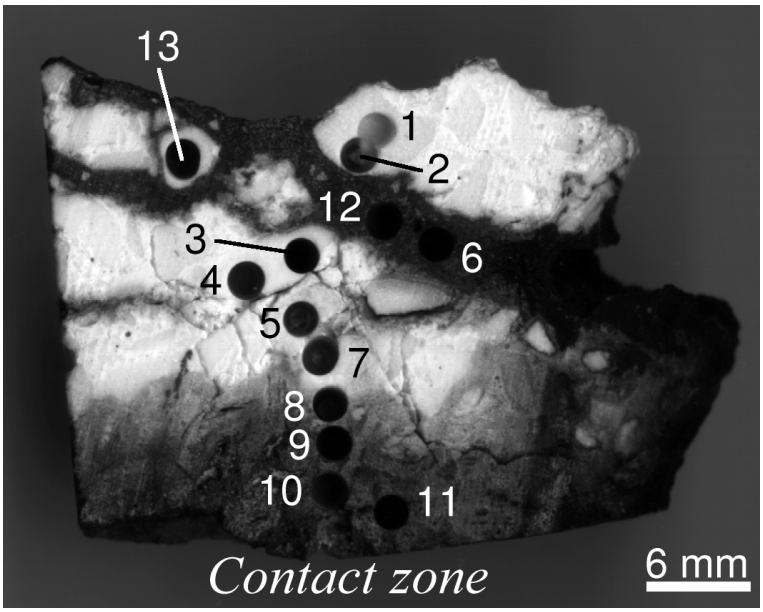

Figure 9.1: Photograph of a hand specimen of a neutral ladle lining taken at the refractory to melt contact. The dark zones outline the corrosion of the refractory during use. 13 samples were taken for oxygen isotope analysis using a micro core drill.

Table 9.2: Oxygen isotope composition of micro core samples taken from specimen 101.

Sample	Description	δ^{18}O
101/1	corundum	+19.5‰
101/2	corundum	+19.8‰
101/3	corundum	+20.3‰
101/4	corundum	+19.6‰
101/5	corundum	+19.2‰
101/6	dark veinlet infill	+17.9‰
101/7	corundum	+18.1‰
101/8	contact zone	+18.0‰
101/9	contact zone	+18.2‰
101/10	contact zone	+18.6‰
101/11	contact zone	+18.0‰
101/12	dark veinlet infill	+17.8‰
101/13	corundum	+18.1‰
101/14	corundum	+18.6‰
101/15	dark veinlet infill	+18.1‰

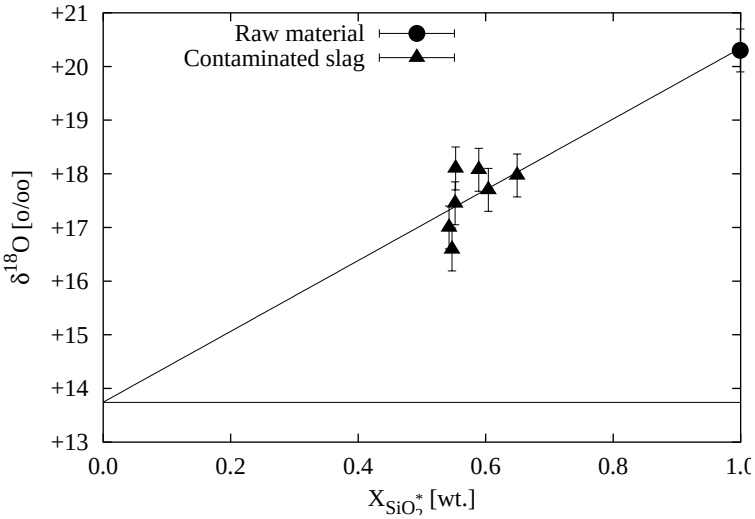

Figure 9.2: Plot of δ^{18}O of the tundish slag vs. the reduced $X_{SiO_2^*}$ of the tundish slag. The diagram indicates contamination by foreign components with an average δ^{18}O value of +13.8‰.

δ^{18}O of +20.3‰. During casting, the slag is contaminated with several components. Isotope exchange with the atmosphere is not very likely because of the steep temperature gradient in the tundish slag. The top side appears to be relatively cool and is not molten. Only at the interface between the slag and steel melt a film of silica melt forms.

The decrease in SiO_2 content of the tundish slag can be taken as measure for the degree of contamination. Figure 9.2 illustrates the relation between δ^{18}O and the degree of contamination. $X_{SiO_2^*}$ shall be termed the reduced SiO_2 fraction in the tundish slag. The tundish slag raw material has per definition $X_{SiO_2^*} = 1$. Assimilation of components like Al_2O_3 or MgO consequently reduce $X_{SiO_2^*}$ to values < 1. Alumina probably was introduced from floated oxide inclusions, CaO may be attributed to contamination by ladle slag and MgO points to assimilation of tundish slag. Assuming this, $X_{SiO_2^*}$ is calculated as follows:

$$X_{SiO_2^*} = 1 - \frac{SiO_2^0 - SiO_2 + 0.22 \times (MgO - MgO^0)}{100} \tag{9.2}$$

SiO_2^0 is the initial concentration of silica in the tundish slag raw material (92.04 wt.%, Sample 6). MgO^0 is the initial magnesia concentration (0.50 wt.%, Sample 6). SiO_2 and MgO denote the concentrations in the altered tundish slag. 0.22 is the ratio SiO_2/MgO of the unaltered sprayed tundish lining. This factor considers the contribution of not only MgO but, to a certain amount, also of SiO_2 through assimilation of tundish lining.

Including the the maximum and minimum δ^{18}O value of the group of samples, a variational width in δ^{18}O of the assimilated material of +12–15.5‰ is calculated. The assimilated material, however, is, with respect to chemical and isotopic composition, a mixture of different components.

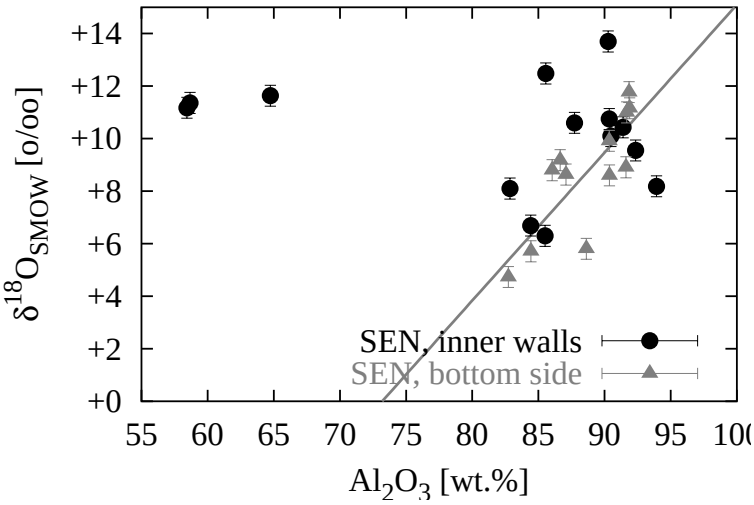

Figure 9.3: Plot of $\delta^{18}O$ vs. Al_2O_3 of clogging samples from inside the SEN (solid circles) and the bottom side of the SEN (triangles). No correlation between the Al_2O_3 content and $\delta^{18}O$ can be made out for inner wall samples. A weak positive correlation between $\delta^{18}O$ and the Al_2O_3 content is indicated in the deposits of the bottom side.

9.3.3 Ladle slag

Two samples of white ladle slag were isotopically characterized (Sample 75b/1: +18.2‰; Sample 78/1, +17.6‰). No samples of dark Fe and Mn rich slag are available. Indirectly, the slag adjacent to and within the dark veinlets of sample 101 may give a hint of the isotopic composition of the dark ladle slag. Values of +17.8 to +18.0‰ (sample 101: 6, 10, 11, 12) were determined (see Table 9.1 on page 91).

Independent of type, a $\delta^{18}O$ value in the range of +17 to +18‰ is reasonable for the tundish slag. However, it should be noted that these are the first oxygen isotope measurements on materials of the system of refractories and slags. Therefore there is still some uncertainty weather the data obtained are representative for the typical composition of these materials.

9.3.4 Clogging

A set of clogging samples from steel plant A was isotopically analyzed. The average of 26 analyzed samples is +9.4‰ with a standard deviation (1σ) of $\pm$2.4‰. A minimum value of +4.7‰ and a maximum value of +13.7‰ were measured. The samples are to be divided into two general groups:

- Oxide deposits along the inner wall of the SEN
- Samples taken from a crust along the bottom side of the SEN.

No distinct correlation between chemical composition and $\delta^{18}O$ is observed for the samples taken from the inner wall of the SEN (Fig. 9.3, 9.4). In the case of samples from the bottom side of the SEN, a negative correlation between the molar MgO/Al_2O_3 ratio and the $\delta^{18}O$ value is indicated. The correlation, however, is not very well defined.

Most remarkable is the isotopic zonation observed in the bottom side precipitates. The $\delta^{18}O$ values of samples 56, 58b, and 60 decrease towards the steel melt contact from +9 to

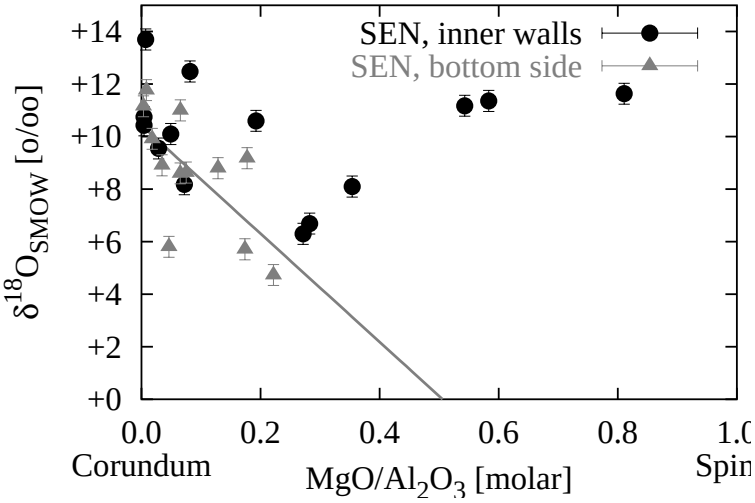

Figure 9.4: Plot of $\delta^{18}O$ vs. the molar MgO/Al_2O_3 ratio of clogging samples from inside the SEN (solid circles) and the bottom side of the SEN (triangles). The gray line was calculated by linear regression from data points of the bottom side precipitate. A negative correlation between $\delta^{18}O$ and the relative amount of "spinel" component is indicated.

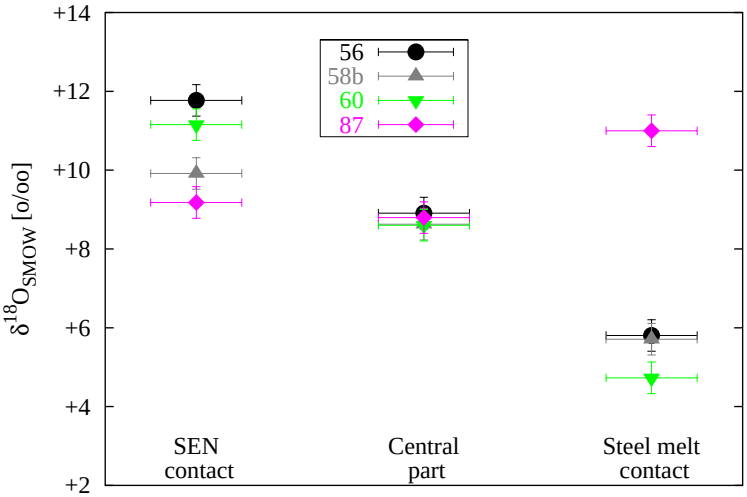

Figure 9.5: Plot of $\delta^{18}O$ vs. the position in the SEN bottom side precipitate. Note the decrease in $\delta^{18}O$ towards the steel melt contact by approximately -5‰ (Samples 56, 58b, 60). Sample 87 does not follow this trend and is enriched in ^{18}O at the steel melt contact relative to the central part. The values in the central part vary in a narrow range of +8.3 to +9.1‰.

+12‰ at the SEN contact from +5 to +6‰ at the steel melt contact (Fig. 9.5). Sample 87, however, breaks this trend by having a value of +11‰ at the steel melt contact.

A well-preserved "sedimentary bedding" can be observed in the bottom side precipitates. These deposits may bear a record of the "inclusion history" during casting. The early precipitates thus would have $\delta^{18}O$ of +9–12‰. Towards the end of casting, the $\delta^{18}O$ values of the precipitates decrease to values of +5–6‰.

Unlike the deposits from the SEN inner side, mould powder may contribute to the formation of the crust along the bottom side of the SEN. Addition of mould powder component to the deposits may thus disturb the record.

Table 9.3: Oxygen isotope composition of separates of three different andalusite refractory bricks.

Sample	Description	$\delta^{18}O$
116	colorless, clear andalusite	+10.8‰
116	mullite-SiO_2 intergrowth	+11.6‰
117	mullite-SiO_2 intergrowth	+15.1‰
117	mullite-SiO_2 intergrowth	+12.8‰
117	Fe-oxide	+16.4‰
118	mullite-SiO_2 intergrowth	+15.5‰
118	mullite-SiO_2 intergrowth	+14.2‰
118	mullite-SiO_2 intergrowth	+15.2‰
118	Fe-oxide	+18.1‰

9.4 Steel plant B

9.4.1 Ladle refractories

Andalusite refractory bricks

Three samples of unused andalusite bricks, which were, beside neutral linings, used in the ladle of steel pant B were isotopically investigated. Microscopy revealed sample 116 to be composed of andalusite and submicroscopic intergrowths of mullite-SiO_2 pseudomorphing andalusite. Large andalusite grains are not entirely mullitized and andalusite remained in the cores. Two samples were separated from this brick: one colorless transparent separate of unaltered andalusite and one sample of mullitized andalusite.

The andalusite in brick sample 117 is entirely disintegrated to mullite and SiO_2. Two aggregates of mullite-SiO_2 intergrowth were separated from the brick and isotopically analyzed. One reddish-brown iron oxide inclusion was also separated and analyzed. The results are shown in Table 9.3. Sample 118 is a brick very similar in appearance to sample 117. Three samples of the mullite-SiO_2 intergrowth and one sample of the iron oxide were separated and analyzed.

Sample 116, which contains remains of andalusite is notably depleted in ^{18}O relative to the two other studied andalusite samples. A value of +10.8‰ resembles $\delta^{18}O$ values typically found in natural alumosilicates (see Sharp, 1995). The mullite-SiO_2 intergrowth in sample 116 is slightly enriched relative to the andalusite educt.

Samples 117 and 118 are entirely composed of the submicroscopically intergrown reaction products. The $\delta^{18}O$ values of the reaction products are varying between +12.8‰ and +15.5‰ with an average of +14.6‰. Iron oxide inclusions in samples 117 and 118 are enriched in ^{18}O compared to the mullite-SiO_2 intergrowth by approximately 3‰. The iron oxide with its relatively high $\delta^{18}O$ is not in isotope equilibrium with the mullite. The enrichment in ^{18}O reflects oxygen isotope exchange with the oven atmosphere.

The andalusite bricks ($\delta^{18}O$ of +13.6±1.9‰) are depleted in ^{18}O relative to the investigated corundum ladle lining by 5‰. However, more detailed analyses of the different types of ladle lining are necessary. Yet, this reconnaissance data may give a first information about the oxygen isotopic composition of neutral ladle refractories.

Table 9.4: Oxygen isotope composition of clogging samples from steel plant B. Notable are the very low values obtained from this steel plant as compared to the values measured in steel plant A.

Sample	Type	δ^{18}O
HO-1	alumina-rich clogging	+2.5‰
HO-2	alumina-rich clogging	+1.4‰
SEN-1	alumina-rich clogging	+3.3‰
SEN-6	alumina-rich clogging	+5.8‰
TN-3	alumina-rich clogging	+2.1‰
TN-4	alumina-rich clogging	+2.1‰
TN-5	alumina-rich clogging	+1.6‰
Average		+2.7±1.5‰

9.4.2 Clogging

A set of only seven samples of clogging was available from steel plant B. The oxygen isotopic compositions of the samples are listed in Table 9.4. The δ^{18}O of the samples varies between +1.4‰ (HO-02) and +5.8‰ (SEN-6) with an average of +2.7±1.7‰.

The samples were macroscopically indistinguishable from the clogging observed at steel plant A. Low sample amounts prevented the preparation of fused beads for XRF chemical analysis. The behavior of the samples during exposition to the laser beam, however, was very similar to that of the alumina-rich samples from steel plant A. The steel quality casted at plant B was also very similar (low alloyed, Al-killed, 0.04–0.05 wt.% Al) to that in steel plant A. Therefore it is reasonable to assume that these samples are similar in chemical composition to the clogging samples from steel plant A.

Apart of the andalusite bricks, no samples of refractories and slags were available from steel plant B. The refractories and slags used in the tundish, however, were identical to those used in steel plant A.

The raw material of the tundish lining is mixed with drinking water[1] in order to obtain a sprayable suspension. The fine-grained fraction of the periclase may undergo hydration at low temperatures during spraying and drying of the moist disposable lining. At high temperatures during the drying process (the tundish lining is pre-heated to temperatures up to 1250°C), brucite breaks down and periclase is formed (with negligible or only low oxygen isotope fractionation).

Hydration of periclase at low temperatures and dehydration of the resultant brucite at high temperatures can be a possible mechanism to produce isotopically “light” periclase. Such periclase may contribute to the formation of precipitates with δ^{18}O of +2.7‰.

Hydration of periclase at temperatures between 25°C and 100°C would result in the formation of brucite with δ^{18}O of +2‰ and -2.5‰, respectively (Fig. 9.6).

Dehydration of the brucite at elevated temperatures may be result in formation of periclase which is isotopically depleted compared to the periclase raw material. The assumption that the water/rock ratio is large, however, is not correct. In fact, the water to rock ratio is $<$0.1 which potentially limits the formation of isotopically “light” periclase (law of mass conservation).The periclase raw material used in steel plant B is the same as used in steel

[1] Mid-European drinking water has a mean δ^{18}O in the range of -8‰.

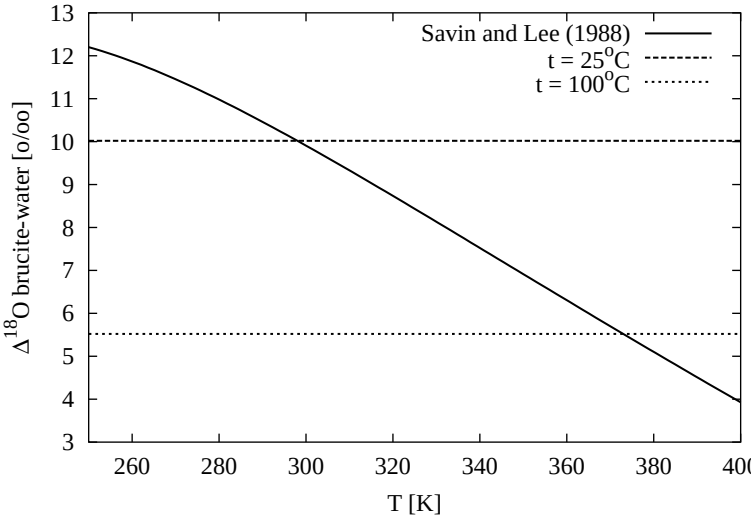

Figure 9.6: Oxygen isotope partitioning between brucite and water Savin and Lee (1988). At a formation temperature of 25–100°C, drinking water (-8‰) should coexist with brucite having δ^{18}O of +2‰ and -2.5‰, respectively (assuming a water/rock ratio $\gg$1).

plant A. Thus a δ^{18}O value of +13.7‰ is assumed for the periclase raw material. Hydration of the periclase at 25°C by reaction with drinking water (-8‰) and a W/R ratio of 0.1, brucite with δ^{18}O of +12.5‰. This calculation shows that hydration of periclase may result in formation of brucite, which is isotopically depleted in ^{18}O relative to the periclase educt, but a low W/R ratio considerably limits the degree of depletion to only a few ‰. Assuming a W/R ratio of 0.1, no brucite with δ^{18}O in the range of +2.7‰ can be produced.

Equilibrium evaporation of a fraction of the water from the moist tundish lining would, in addition, account for an enrichment in ^{18}O in the residual moisture. At 25°C, the fractionation between water and vapor is $1000 \ln \alpha_{\mathrm{l-v}}(^{18}\mathrm{O}) = +9.2‰$ (Horita and Wesolowski, 1994). Assuming that the vapor leaves the system, a considerable increase in δ^{18}O following a *Rayleigh* type fractionation process would be observable (Eqn. 9.3).

$$\frac{R_\ell}{R_\ell^0} = f^{\left(\frac{1}{\alpha}-1\right)} \tag{9.3}$$

Equation 9.3 expressed in terms of δ^{18}O values is

$$\delta^{18}\mathrm{O}_\ell - \delta^{18}\mathrm{O}_\ell^0 = \left(\frac{R_\ell}{R_\ell^0} - 1\right) \times 1000 \tag{9.4}$$

$$\delta^{18}\mathrm{O}_\ell - \delta^{18}\mathrm{O}_\ell^0 = \left(f^{\frac{1}{\alpha_{\mathrm{v}-\ell}}-1} - 1\right) \times 1000 \tag{9.5}$$

The subscript ℓ denotes the liquid. The superscript ^{0} indicates the composition of the initial liquid without loss of vapor. ^{18}R is the ratio $^{18}\mathrm{O}/^{16}\mathrm{O}$, α is the oxygen isotope fractionation coefficient and f the fraction of remaining water $\delta^{18}\mathrm{O}_\ell - \delta^{18}\mathrm{O}_\ell^0$ is also expressed as $\Delta^{18}\mathrm{O}_{\mathrm{v}-\ell}$.

Depending on the fraction of remaining liquid, a strong increase in δ^{18}O of the liquid can be obtained by evaporation. If the remaining fraction reacts with the periclase to brucite,

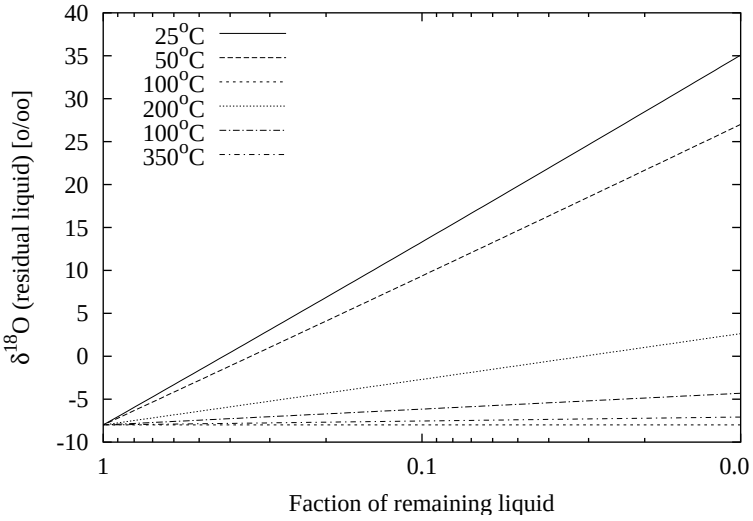

Figure 9.7: Plot of $\delta^{18}O$ of the remaining liquid (initial liquid $\delta^{18}O^{0}_{\ell} = -8‰$) vs. the fraction of liquid remaining. The vapor is assumed to leave the system (*Rayleigh* distillation). Fractionation coefficients $\alpha_{v-\ell}(^{18}O)_T$ from Horita and Wesolowski (1994).

a brucite even richer in ^{18}O than the periclase educt could possibly be produced. With decreasing fraction of remaining water, however, also the water/rock ratio will decrease. With lower W/R ratio, the influence of the water on the isotope composition of the brucite reaction product will decrease.

In summary it is stated that hydration of periclase in the tundish lining could result in an isotopic shift towards slightly lower $\delta^{18}O$ values of only a few ‰. A low W/R ratio and evaporation of a fraction of the water from the tundish lining, however, will prevent the formation of an isotopically “light” brucite in the tundish lining.

It is inferred that kinetic effects may play a role in the oxidation of alloyed Al in steel plant B. However, a more detailed oxygen isotope study is necessary to trace the origin of isotopically “light” oxide precipitates in steel plant B.

9.5 Other periclase raw materials

9.5.1 Periclase imported from China

Caustic periclase is pressed to pellets prior to sintering. A $\delta^{18}O$ profile of 12 single analyses was measured over a sintered periclase pellet (Sample 108, Fig. 9.8). The individual samples were taken using a micro core drill with an internal diameter of 1 mm. The pellet shows a strong zonation in $\delta^{18}O$ (Fig. 9.9). +7‰ was measured in the core and values up to +15‰ at the outer margin.

The profile clearly illustrates that the periclase raw material is isotopically heterogeneous on mm-scale. The variations within a single sintered pellet are related to the sintering process. An increase in $\delta^{18}O$ due to high temperature sintering of periclase was observed by Herbrich et al. (1990). Two processes can be responsible for the enrichment in ^{18}O during sintering:

1. Recrystallization of caustic periclase causes an increase in $\delta^{18}O$ through isotope ex-

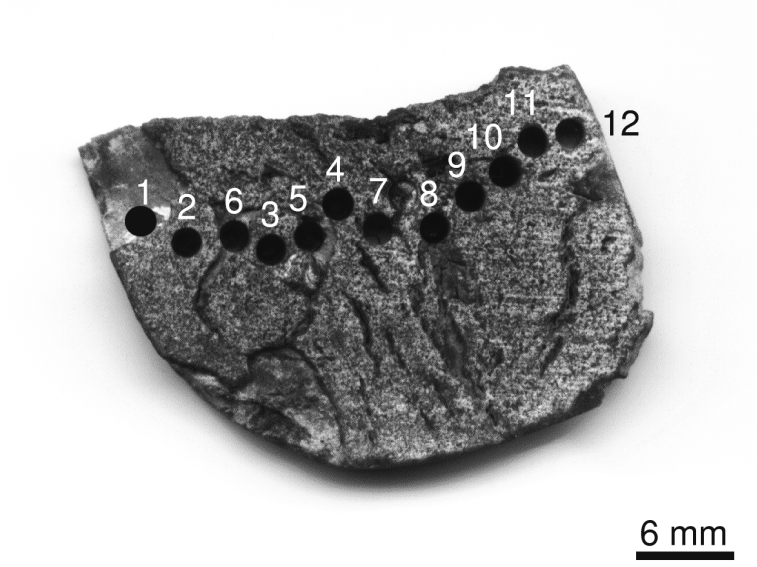

Figure 9.8: Photography showing a cross section through a nut-shaped sinter pellet of periclase from China (Sample 108). Samples for oxygen isotope analyses were taken using a 1 mm (i. d.) micro core drill. The corresponding analyses are ploted in Figure 9.9.

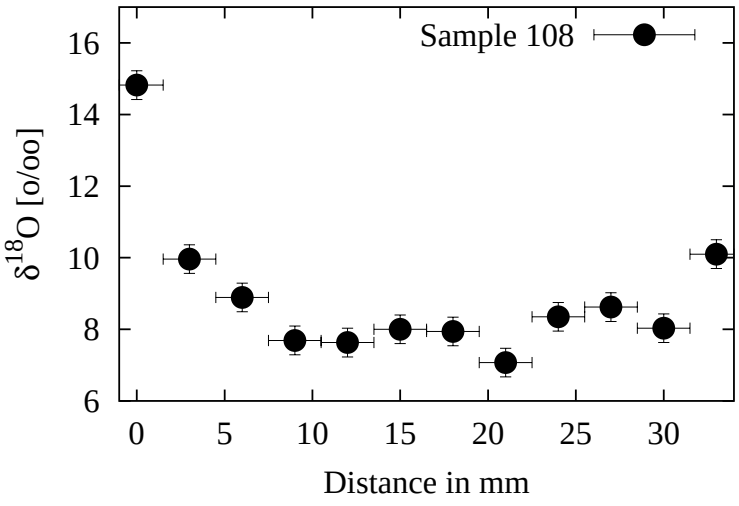

Figure 9.9: $\delta^{18}O$ plotted vs. the distance across a periclase sinter pellet (Fig.9.8). The $\delta^{18}O$ increases from +7‰ in the center up to +15‰ towards the rims of the pellet.

change with the oven atmosphere. Equilibrium between periclase and atmosphere will not be attained (especially in the cores of the sintered pellets).

2. Evaporation and re-precipitation of periclase on the pellets surfaces. The periclase precipitates are in isotope equilibrium with the atmosphere in the oven and have $\delta^{18}O$ close to +23.5‰ (Herbrich et al., 1990).

Both processes may contribute to the enrichment in $\delta^{18}O$ towards the outer margins of the sintered pellet. No investigation was made on the large scale variations in $\delta^{18}O$ between different charges. On large scale, however, the variation will probably be less prominent.

9.5.2 "Sea water magnesite"

"Sea water magnesite" represents a type of periclase which is produced by dehydration of brucite precipitated from sea water (Birch and Wicken, 1949; Konopicky, 1957, Eqn. 9.6).

$$Mg^{2+}_{aq} + Ca(OH)_2 \rightleftharpoons Mg(OH)_2 + Ca^{2+}_{aq} \tag{9.6}$$

Sea water contains about 4 g/l $MgCl_2$ (at San Francisco, USA, Birch and Wicken, 1949). The calcium hydroxide necessary as precipitation agent can be extracted from oyster shells which may be available as by-products of sea fishing.

Sample 110 is a periclase produced in the Unites States from precipitated $MgOH_2$ (Broß, 1998, pers. comm.). Two values were obtained from fragments of a sintered pellet: $\delta^{18}O = +9.8‰$ and $\delta^{18}O = +16.3‰$. The variation is attributed to heterogeneities within the pellet as was also observed in sample 108 (see Fig. 9.9).

Savin and Lee (1988) published data about the temperature dependence of the oxygen isotope fractionation between brucite and coexisting water. Brucite is chemically precipitated from sea water ($\delta^{18}O \approx 0$) and should be in equilibrium with the water. Temperatures of precipitation will certainly be between 0 and 100°C, but most probably somewhere in the range of 25°C. Using the thermometer of Savin and Lee (1988), the $\delta^{18}O$ of precipitated brucite is calculated to +10.01‰.

The composition of the final periclase product, however, changes as a result of dehydration and sintering processes as indicated by the oxygen isotope analyses.

9.5.3 De-carbonatization experiment of natural magnesite

Two natural magnesite samples (02, 03) were decarbonatized under controlled conditions in order to study the change in isotopic composition during periclase formation. Sample 2 is coarse-grained and sample 3 is fine-grained magnesite, respectively. The oxygen isotopic composition of the carbonates was determined by decomposition in concentrated phosphoric acid following a procedure described by Cornides and Kusakabe (1977). Liberated CO_2 was analyzed in a conventional dual inlet mass spectrometer. The magnesite samples were heated by Broß (1998, pers. comm.) under atmospheric conditions at temperatures 800°C and 1600°C for 4 h each. The periclase reaction products were isotopically characterized (Tab. 9.5.3).

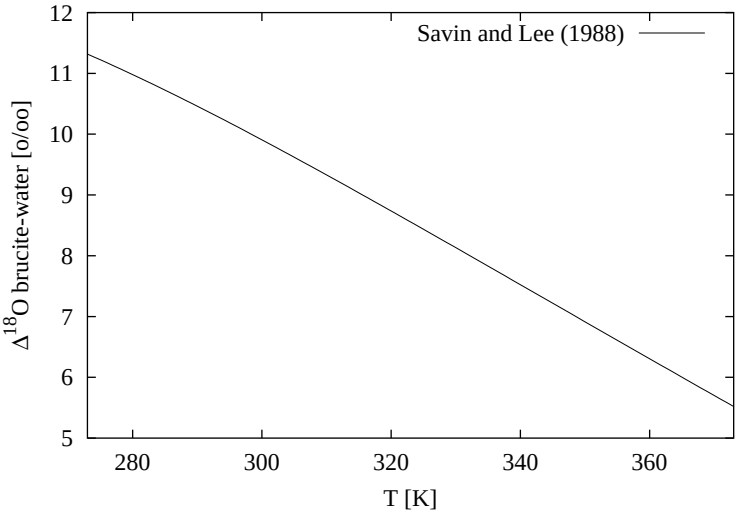

Figure 9.10: Plot of $\Delta^{18}O_{brucite-water}$ vs. temperature in Kelvin (data from Savin and Lee, 1988). At a precipitation temperature of 298 K (25°C), the brucite is expected to have a δ^{18}O value of +10.01‰ assuming that sea water is 0‰.

Table 9.5: Oxygen isotope composition of two magnesite samples before and after firing at 800°C and 1600°C

Sample	Description	δ^{18}O, Magnesite	δ^{18}O, 800°C	δ^{18}O, 1600°C
02	Fine grained	+10.5‰	+6.9‰	+12.0‰
03	Coarse XX	+11.7‰	+6.5‰	+11.9‰

Notable are the very similar δ^{18}O-values obtained after de-carbonatization of the magnesite samples at 800°C and at 1600°C. These values could give the impression that isotope equilibrium with atmospheric oxygen was reached. However, as pointed out by Herbrich et al. (1990), oxygen isotope partitioning between atmospheric oxygen and periclase is approaching zero at temperatures as high as 1600°C. The values measured would, in contrast, indicate a fractionation of $\Delta^{18}O^{1873\,K}_{AO-per} = +12.5‰$[2].

An oxygen isotope fractionation of at least -3‰ is observed between magnesite (+11‰) and liberated CO_2 and periclase (+6.7‰). The oxygen isotope fractionation between calcite and CO_2 at 300°C, which is the estimated lower temperature limit of decomposition, was reported to be -10.2‰ (Bottinga, 1968) and -8.8‰ (Zheng, 1994). At 765°C, which is the estimated upper temperature limit of decomposition, a partitioning of -5.8‰ (Zheng, 1994) and -4.6‰ (Bottinga, 1968) is calculated. The isotope partitioning between calcite and magnesite is estimated to be very low at temperatures exceeding 300°C. The isotopic fractionation between calcite and dolomite at 300°C is as low as -1.0‰ and at 765°C less than -0.1‰ (Sheppard and Schwarz, 1970; Golyshev et al., 1981).

Figure 9.11 is a sketch illustrating the isotopic evolutionary pathway from magnesite to periclase in the δ^{18}O-T diagram.

The following model is inferred: Magnesite breaks down to periclase at a temperature somewhere between 300°C and 765°C. The resulting periclase is depleted in ^{18}O relative to

[2] AO denotes: atmospheric oxygen

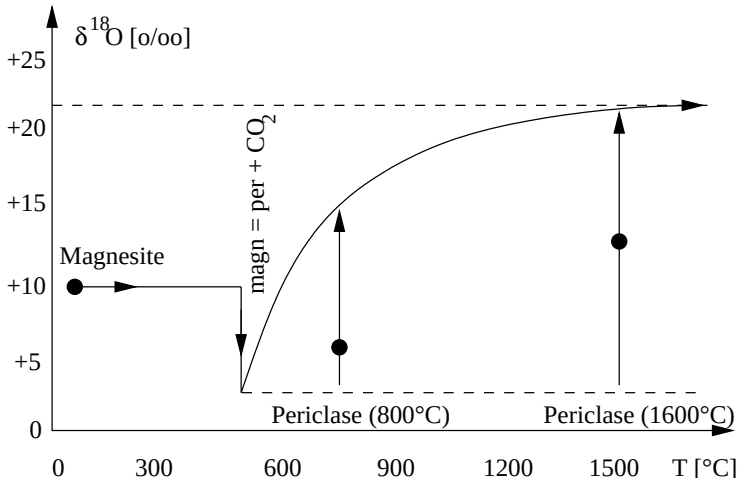

Figure 9.11: Sketch illustrating the inferred isotopic pathway of magnesite to periclase in the δ^{18}O-T diagram. At 300–765°C the magnesite educt reacts to periclase which is depleted in ^{18}O relative to the magnesite. Annealing of the periclase leads to a shift in isotope composition towards the δ^{18}O of the oven atmosphere (+23.5‰). The filled circles outline the δ^{18}O data obtained from magnesite (+11‰), and periclase annealed at 800°C (+6.7‰) and 1600°C (+12.0‰)

the magnesite. Annealing of the periclase at higher temperatures leads to recrystallization and diffusive exchange with the oven atmosphere. Depending on the annealing time and temperature, a δ^{18}O value identical to the oven atmosphere is approached (see Herbrich et al., 1990). The δ^{18}O values obtained in two periclase samples annealed at 800°C and 1600°C do not mirror equilibrium. In equilibrium with the gas phase, a δ^{18}O value of the periclase close to +23.5‰ is expected (Herbrich et al., 1990).

Chapter 10

Thermodynamics

Als das gemeinschaftliche und nächstliegende Ziel [...] können wir jenes hinstellen, die Frage, welche Vorgänge werden sich bei einer gegebenen Anordnung eines (endlich ausgedehnten) Systems abspielen, und welches wird der Zustand dieses Systems nach dem Verlaufe einer bestimmten Zeit sein, in möglichst vielen Fällen, möglichst gründlich und möglichst einfach zu beantworten.

Walther Nernst
Theoretische Chemie vom Standpunkt der Avogardoschen Regel und der Thermodynamik, 1921

10.1 Introduction

Thermodynamic calculations of reactive systems are described by the *Gibbs' Equation*

$$\Delta G_T^0 = -RT \cdot \ln K_R \tag{10.1}$$

with ΔG_T^0 being the Free Gibbs Enthalpy relative to the reference state and at elevated temperatures T. R is the gas constant and is 8.31441 JK·mol^{-1} (Wedler, 1987) and T the temperature in K. K_R is the reaction constant and is defined as

$$K_R = \prod a_i^{\nu_i} \tag{10.2}$$

where a_i are the activities of the components i and ν_i the stoichiometric coefficients of the components, respectively. The activities of the components are the product of the activity coefficient γ_i and the mole fraction X_i of the component

$$a_i = \gamma_i \cdot X_i. \tag{10.3}$$

The Gibbs Free Enthalpie as molar quantity is expressed as:

$$\frac{\partial \Delta G_T^0}{\partial i} = \mu_{i,T}^0 \tag{10.4}$$

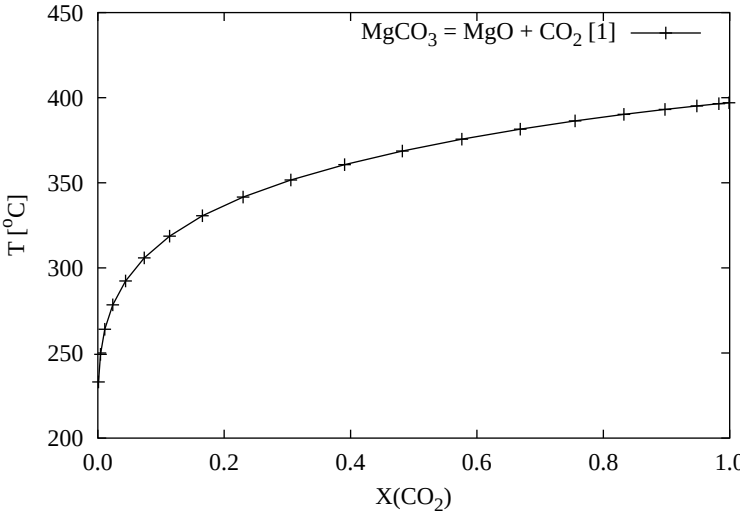

Figure 10.1: T-X(CO_2) section of the calcination reaction of magnesite (data from Holland and Powell, 1998, 1, p = 1 bar).

$\mu^0_{i,T}$ is the partial molar Gibbs Free Enthalpie and is also termed the *chemical potential*.

The activity coefficients a_i are determined in experiments. A compilation of activity coefficients for binary alloys are compiled in Hultgren et al. (1973). High temperature thermodynamic data were published by Robie et al. (1979), Berman (1988). Holland and Powell (1998) and Mallard and Linstrom (2000). Each of the thermodynamic data sets is internally consistent, i. e. thermodynamic calculations should be conducted using only one data set. The differences between the data sets are usually not more than a few kJ/mol ($\mu^0_{i,T}$). Since not all phases were present in all data sets, values from different sets were mixed in the calculations. The error which is introduced by using non-consistent data sets, however, was proved to be small and not of importance for the results of this study.

The following calculations are all based on Equation 10.1. For gaseous phases, the partial pressure p_i was used instead of the activity which implies that the gas phase was assumed to behave ideal (i. e. $p_i^{gas} \sim X_i^{gas}$).

10.2 Magnesite calcination

At high temperatures, magnesite reacts to periclase and CO_2. The temperature of calcination was determined by Trojer et al. (1981) in experiments[1] to 720–765°C .

Using THERMOCALC (Holland and Powell, 1998), a T-X(CO_2) section of the reaction $MgCO_3 \rightleftharpoons MgO + CO_2$ can be calculated (Fig. 10.1).

The difference between the calculated and the experimentally determed decomposition temperature is in the range of more than 300°C. In an atmosphere of pure CO_2, a decomposition temperature close to 400°C is calculated., which is still more than 300°C below the values experimentally obtained by Trojer et al. (1981). The reason for the difference is enigmatic. Turčániová et al. (1996) and Jesenák et al. (1997) illustrated that grain size and the

[1] DTA, 5–10°/min, atmospheric conditions, i. e. $p_{CO_2} \approx 0.03$ bar

defect concentration of the reactants can considerably influence the kinetics of the reaction. The presence of impurities, including silica, iron oxide and lime, in the magnesite can also lead to a difference between calculated and observed calcination temperatures.

10.2.1 Brucite dehydration

The dehydration reaction of brucite in dependence on the water activity was calculated using THERMOCALC (Holland and Powell, 1998). A decomposition temperature between 158°C ($a_{H_2O} = 10^{-2}$ bar) and 273°C ($a_{H_2O} = 1$ bar, $p_{tot} = 1$ bar) was calculated. Trojer et al. (1981) determined a dehydration temperature of brucite of 425–470°C under atmospheric conditions (DTA, 10°C/min, without controlling the water activity). Again, a significant difference between the experimental data by Trojer et al. (1981) and the calculated data is observed. Kinetic effects are inferred as explanation of the discrepancy.

10.3 Redox reactions

10.3.1 Al-Al_2O_3 deoxidation equilibrium

Aluminium metal is used to deoxidize the steel melt in the ladle. The deoxidation reaction is:

$$\begin{aligned} 4Al_{\ell}^{Fe} + 3O_2 &\rightleftharpoons 2Al_2O_3 \\ \text{with } K_R &= \frac{a^2_{Al_2O_3}}{a^4_{Al} \times p^3_{O_2}} \,. \end{aligned}$$

$a_{Al_2O_3}$ can be assumed to be unity since corundum is the alumina bearing phase. a_{Al} is the activity of aluminium dissolved in the steel melt. Concentrations of aluminium vary only in a narrow range close to 0.04 wt%, which corresponds to a mole fraction of $X_{Al} = 0.00083$. The activity coefficient of aluminium in dependence of the mole fraction of the alloying metal in the iron liquid at 1873 K is illustrated in Figure 10.2 (Hultgren et al., 1973). The activity coefficient decreases considerably with decreasing X_{Al}^{Fe}.

The activity of 0.04 wt% Al in liquid steel at 1873 K is $a_{Al}^{Fe} = 0.06 \times 8.28 \times 10^{-4}$ $(= 4.97 \times 10^{-5})$ (Fig. 10.2). Inserting of T and a_{Al}^{Fe} gives the equilibrium oxygen partial pressure at 1873 K:

$$\lg p_{O_2} = \frac{\Delta G_T^0}{3 \times 2.303 \times RT} - \frac{4}{3} \lg a_{Al}^{Fe}(X_{Al}^{Fe}, \gamma_{Al}^{Fe})_{1873\,K} \qquad (10.5)$$

lg is used as synonym for the expression $\log_{10}$. The oxygen partial pressure buffered by the system Al–Al_2O_3 at 1873 K is $p_{O_2} = 10^{-14.249}$ bar (thermochemical data by Mallard and Linstrom, 2000). This calculated value corresponds to a value given by Bannenberg (1995) of $< 10^{-14}$ bar at 1873 K and 0.04 wt.% Al. The dependence of the γ-value on temperature is neglected here. The temperature of the steel bath in ladle and tundish deviates only little from 1600°C in a range within 1545–1630°C.

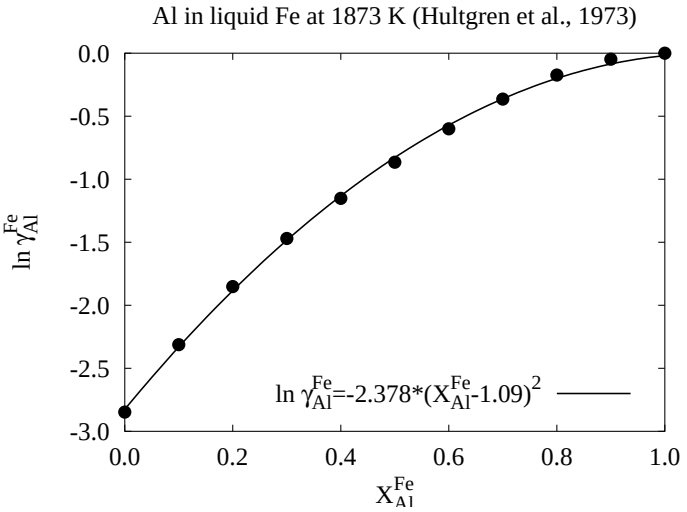

Figure 10.2: Plot of $\ln \gamma_{Al}^{Fe}$ vs. X_{Al}^{Fe} in the binary System Fe-Al at 1873 K. The data are fitted by the empiric function: $\ln \gamma_{Al}^{Fe} = -2.378 \times (X_{Al}^{Fe} - 1.09)^2$

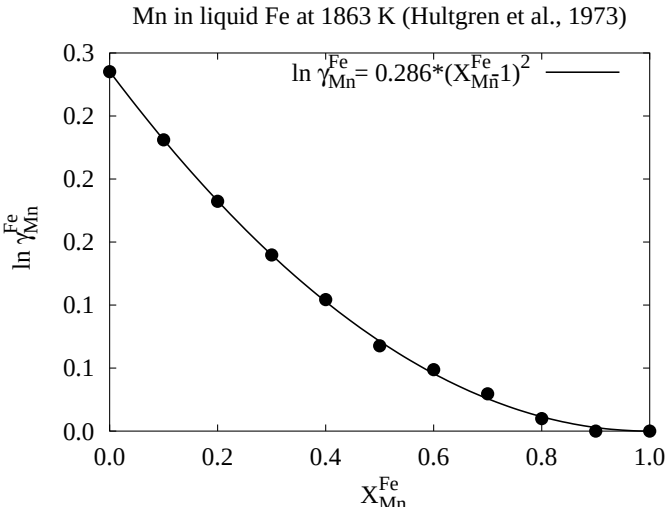

Figure 10.3: Plot of $\ln \gamma_{Mn}^{Fe}$ vs. X_{Mn}^{Fe} in the binary System Fe-Mn at 1863 K. The data are fitted by the function: $\ln \gamma_{Mn}^{Fe} = 0.286 \cdot (X_{Mn}^{Fe} - 1)^2$

10.3.2 Periclase of the tundish lining

It was observed that the periclase in the tundish lining contains considerable amounts of Fe and Mn. Manganese is the predominant alloying element in the low alloyed Al-killed steels. Concentrations vary between 0.1 and 1.4 wt%, respectively. Manganese tends to leave the iron melt at 1873 K as indicated by an activity coefficient greater than one (Fig. 10.3).

The activity of Mn in a steel melt containing 1.0 wt.% dissolved Mn is $a_{Mn}^{Fe} = 0.01 \times 1.32 = 0.0132$.

Periclase in equilibrium with the steel melt, at 1873 K, contains 0.13 mol% FeO and 0.12 mol% MnO. At a Mn content of the steel of 1.4 mol%, 0.6 mol% MnO are stable in the periclase. The MnO and FeO contents increase significantly at lower temperatures. The dark intermediate zone is the product of enrichment of Mn and Fe in the cooler part of the tundish lining. At a temperature of 1773 K which is estimated in the center of the tundish lining (see

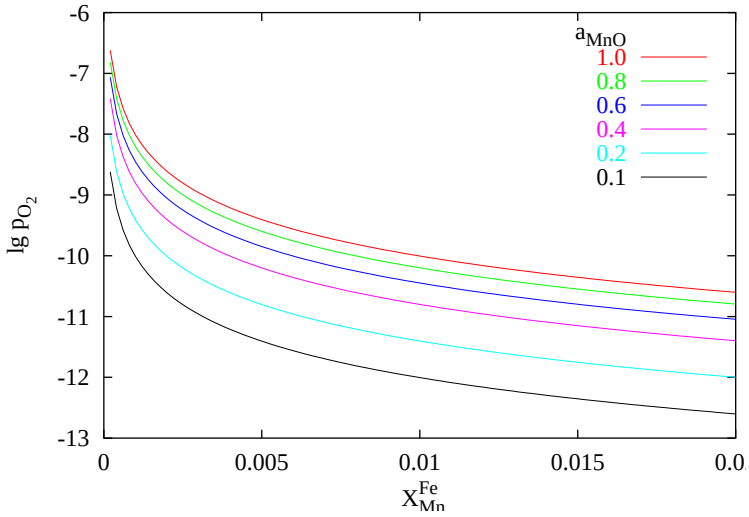

Figure 10.4: Plot of the Mn-oxidation reaction in a diagram of p_{O_2} vs. X_{Mn}^{steel} (T = 1873 K, thermodynamic data from Robie et al., 1979; Mallard and Linstrom, 2000).

von Witzleben et al., 1996), an increase in the Mn content by the factor of 4.3 is observed at a buffered p_{O_2} of $10^{-14.25}$ bar.

The MnO contents in the silicate tundish slag are inferred to be caused by assimilation of Mn from the steel melt. The ladle lining contains approximately 5 wt.% MnO (dark slag). Concentrations of up to 17 wt.% MnO were determined in the tundish slag. Hence assimilation of ladle slag can not be responsible for the MnO content in the tundish slag. Figure 10.4 shows the positions of the reaction lines of the reaction $2\,Mn_\ell + O_2 \rightleftharpoons 2\,MnO$ in a plot of X_{Mn}^{steel} vs. p_{O_2} at 1873 K and various MnO activities.

The diagram shows that the oxygen partial pressure buffered by the system Mn-MnO varies considerably in dependence on the activity of MnO which is part of the liquid silicate slag. At a Mn-concentration of 0.3 wt.%, an oxygen partial pressure between 10^{-11} ($a_{MnO} = 0.1$) and 10^{-9} bar ($a_{MnO} = 1.0$) is buffered. The oxygen partial pressure buffered by the system $Si_\ell^{Fe} - SiO_{2\ell}$[2] at 1873 K is as high as $10^{-7.4}$ bar. This shows evidently that alloyed Mn reduces silica of the tundish slag which is reflected in the high concentrations of MnO in the slag. This conclusion, however, only shows the direction of the reaction. No quantitative estimate can be made since no thermodynamic data are available from such Mn-rich melts which are not known to occur in natural systems.

10.4 Gas phase mediated reactions

Dohmen et al. (1998) have illustrated that considerable mass transfer of components that are commonly regarded as immobile can occur through a gas phase. The conditions necessary for such a process are high temperatures, low p_{O_2}, and presence of phases rich in the volatile components. All these three conditions are fulfilled in the system steel melt and oxide refrac-

[2]Thermodynamic data of Si and O_2 from Mallard and Linstrom (2000), of $SiO_2\ell$ from Holland and Powell (1998), and of γ_{Si}^{Fe} from Hultgren et al. (1973)

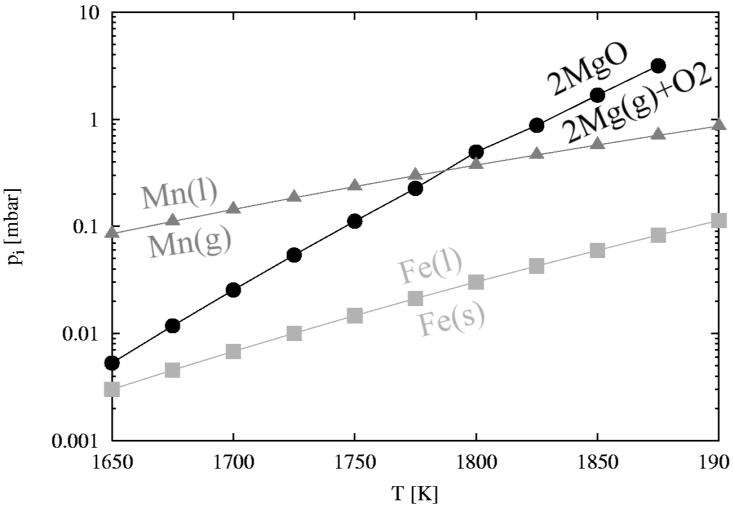

Figure 10.5: Plot of $\lg p_i$ [mbar] of the calculated partial pressures of Fe, Mn, and Mg over a binary Fe-alloy and periclase, respectively, vs. temperature in. Note the high partial pressure of Mn as compared to Fe (data from Mallard and Linstrom, 2000).

tories. Temperatures are even higher than in the experiments conducted by Dohmen et al. (1998) in Knutsen cell mass spectrometry.

The sprayed tundish lining is highly porous with an interconnected porosity as high as 50 vol.%. The composition of the gas phase is unknown and, so far, no data have been published concerning reactions involving the gas phase in the pore space.

Dohmen et al. (1998) have investigated the reaction between solid iron and forsterite at elevated temperatures ($>$ 1000°C) and reducing conditions buffered by the presence of iron metal (IW-buffer). They showed that Fe, Mg and SiO are the major constituents of the gas phase. Mg and SiO originate from vaporized olivine and Fe from the iron metal. At the end of the experiment, the olivine crystal was rimmed by a layer of fayalitic olivine, i. e. Fe migrated through the gas phase from the metal block to the olivine. The composition of the gas phase was monitored by Knudsen cell mass spectrometry throughout the experiments.

The system described is very similar to that studied in the steel plant. The iron metal (steel bath) is separated from forsterite in the refractory by a gas phase in the pore space. The composition of the gas phase is controlled by Fe and Mn vapor from the steel melt, SiO and Mg from the forsteritic olivine, and Mg from vaporized periclase. Periclase is known to have a relatively high vapor pressure (Konopicky, 1957; Trojer et al., 1981; Pelton et al., 1998).

Figure 10.5 illustrates the calculated composition of the gas phase of the model system liquid iron + alloyed Mn + periclase at temperatures between 1650 and 1900 K and $p_{O_2} = 1 \times 10^{-14.25}$ bar (buffered by Al-Al_2O_3 at 1873 K).

$$2MgO_s^{per} \rightleftharpoons 2Mg_g^0 + O_{2g} \text{ with } p_{O_2} = 10^{-14.249}\, bar \quad (10.6)$$

$$Fe_l^{Fe} \rightleftharpoons Fe_g \quad (10.7)$$

$$Mn_l^{Fe} \rightleftharpoons Mn_g \text{ with } X_{Mn}^{Fe} = 0.01 \quad (10.8)$$

The gas phase in the pore space is dominated by Mg^0 vapor from vaporization of MgO (Eqn. 10.6). It exceeds the Mn partial pressure by one order of magnitude in the temperature

range of 1825–1900 K. Notable is the high volatility of Mn as compared to Fe although the Fe concentration approaches 100% and the Mn concentration is only 1 wt.%. The rims of the olivine may also be caused by reaction between Mn-rich gas phase and forsterite.

10.5 Fe-partition between spinel and steel melt

The concentration of FeO in the spinel of the clogging is typically 0.8 mol%. Oxygen buffering reaction is $2\,Fe_\ell + O_2 + Al_2O_3 \rightleftharpoons 2\,FeAl_2O_4$. a_{Fe}^{steel} and $a_{Al_2O_3}$ can be assumed to be unity. The equilibrium constant is expressed as

$$K_R = \frac{a_{herc}^{spl_{SS}}}{p_{O_2}}$$

Thermodynamic calculations show that spinel in equilibrium with a steel melt contains between 0.4 and 1.1 mol% hercynite in the temperature interval between 1823 and 1923 K. 0.8 mol% hercynite point to a temperature of formation of 1890 K. Temperatures in the tundish are typically below 1873 K. The difference rather points to oxygen partial pressures exceeding those calculated with the Al-alumina buffer reaction (Eqn. 10.5).

Despite of the difference, the caclulations show that spinel with only small amounts of hercynite is stable in equilibrium with a steel melt containing 0.04 wt.% Al. Therefore, the hercynite-rich compositions observed in sample 48 can not be regarded to be in thermochemical equilibrium with the steel melt.

10.6 Olivine reduction

The fayalite component of olivine in the sprayed tundish lining is reduced during the casting process. A set of reactions (Eqns. 10.9–10.13) are inferred to describe the reduction process:

$$fa \rightleftharpoons 2\,Fe_s + O_2 + crist \quad (10.9)$$

$$fa + fo \rightleftharpoons 2\,Fe_s + O_2 + enL \quad (10.10)$$

$$2\,fa \rightleftharpoons 4\,Fe_s + 3\,O_2 + 2SiO \quad (10.11)$$

$$fa \rightleftharpoons 2\,Fe_s + 2\,O_2 + 2\,Si \quad (10.12)$$

$$2per + fa \rightleftharpoons 2\,Fe_s + O_2 + fo \quad (10.13)$$

Equations 10.9, 10.10, and 10.12 can be excluded by the results of the TEM study. Evaporation of forsterite to Mg, SiO, and oxygen was observed by Dohmen et al. (1998) in Knutsen cell experiments. SiO is gaseous and does not affect the mechanical stability of the forsterite host, i. e. through formation of a glass of enstatitic composition. The formation of such a glass was observed in the oxidation experiment conducted by Broß (1995) and was reported by Koltermann et al. (1985).

Equation 10.13 infers mass transfer of Mg through the gas phase. The reaction can be split into two equations:

$$2\,MgO_s \rightleftharpoons 2\,Mg_g^0 + O_2 \tag{10.14}$$

$$2\,Mg_s^0 + Fe_2SiO_4 \rightleftharpoons Mg_2SiO_4 + Fe_s \tag{10.15}$$

The first equation expresses periclase evaporation which was reported at elevated temperatures, for instance, by Koeppel (1938), Trojer et al. (1981), and Pelton et al. (1998). The evaporation was, however, not related to the formation of non-metallic inclusions in steel. The vapor pressure of Mg depends on the oxygen partial pressure. Periclase occurring adjacent to the steel melt is at the same temperature than the oxygen buffering system. Periclase distal from the melt contact, however, is exposed to the same oxygen partial pressure (porosity), but has a different temperature. Two different curves arise in the p_{Mg}-T plot (Fig. 10.5). At temperatures above 1873 K, only the buffered system makes sense since the temperature of the refractory is lower or equal to the temperature of the buffering system (steel melt).

At reducing conditions buffered by a steel melt containing 0.04 wt.% alloyed Al and a temperature of 1873 K, a Mg partial pressure of 3 mbar was calculated (Fig. 10.5). With distance from the steel melt, the temperature will drop and as a result also the periclase partial pressure will drop. At an estimated temperature of 1700 K in the center of the refractory, a Mg partial pressure of only 1 mbar is in equilibrium with the periclase. As a result of the temperature difference, Mg will migrate through the gas phase towards the cooler regions of the refractory.

This model is in good agreement with observations made by von Witzleben et al. (1996). They have investigated the reaction between the sprayed tundish lining and the permanenet lining. It was observed that Na and Mg migrate into the permanent lining. Na was correctly inferred to be transported through the gas phase. But Mg was interpreted to have been transported by diffusion into the permanent lining. As a result of this interpretation and experiments based on this assumption, no explanation could be found for the deep penetration of Mg into the permanent lining. Taking into account that Mg behaves mobile in the gas phase, the observations can be explained very well.

The second equation is the reaction between vapor and olivine. The forsterite to fayalite activity can be estimated from the equation:

$$\frac{-\Delta G}{RT} + 2\ln p_{Mg} = \ln \frac{a_{fo}}{a_{fa}} \tag{10.16}$$

The equations shows that olivine exposed to a Mg-rich vapor phase and reducing conditions will be almost pure (>99.9 mol%) forsterite.

10.7 Cation exchange equilibria

The Mn-rich olivine is in apparent equilibrium with the Mn-rich tundish slag. The Nernst distribution coefficients D between olivine, spinel and melt in the Mn-rich system were investigated in detail. The average compositions of the phases are listed in Table 10.7. The

Table 10.1: Element partition coefficients between olivine and melt and spinel and melt. The system is rich in Mn but poor in Fe.

	Olivine	1σ	Spinel	1σ	Glass	1σ	$D^{ol-melt}$	1σ	$D^{spl-melt}$	1σ
SiO_2	37.66	6.13	0.19	0.13	42.13	0.71	0.89	0.146	0.005	0.003
TiO_2	0.04	0.02	0.13	0.02	0.36	0.08	0.12	0.058	0.355	0.095
Al_2O_3	4.05	10.38	68.41	0.61	23.06	1.05	—	—	2.967	0.138
FeO	0.92	0.07	0.51	0.06	0.67	0.05	1.37	0.148	0.756	0.101
MnO	16.92	1.14	6.37	0.45	16.98	0.79	1.00	0.081	0.375	0.032
MgO	40.80	3.41	23.33	0.32	5.06	1.19	8.07	2.013	4.615	1.087
CaO	0.49	0.04	0.06	0.01	10.80	0.55	0.046	0.005	0.005	0.001

BSE image corresponding to the data is Figure 6.17. Only the cores of the olivine were used in the calculation of D. The rims showed a considerable increase in MnO leading to a $D_{Mn}^{ol-melt}$ of up to 1.5, which is inferred to refect the Mn-distribution at lower temperatures.

Although many studies were conducted to determine the element partitioning coefficients between olivine, spinel and melt, no data were published for Mn-rich systems. The knowledge of the partition coefficients, on the other hand, allows to predict the interaction between slag and minerals of the refractory lining.

The partition coefficient of Mn between olivine and melt is 1.00 ± 0.08 at a MnO concentration of 17 wt.%. The rims of the olivine laths are enriched in MnO due to continued equilibration with falling temperature. This indicates that Mn fractionates into the olivine at low temperatures.

In conclusion it can be stated that the Mn-rich olivine in the sprayed tundish lining most probably was formed through crystallization from the Mn-rich slag. This is also indicated by textural characteristics.

Chapter 11

Discussion

IR-laser fluorination CF*irm*MS is proved to be an appropriate tool to determine the oxygen isotope composition of refractory materials.

The system of ladle lining and ladle slag was briefly investigated and the few samples of the ladle refractory can not be regarded as representative. The mineral assemblage and the composition of the phases (wustite, hercynite) in a sample of a neutral bauxite refractory castable (Sample 101) indicate high oxygen partial pressures. EPMA measurements of spinel in a single specimen of the castable, however, revealed local variation in a_{FeO} within the millimeter to centimeter range. This variations point to disequilibrium on a medium scale. The re-use of the ladle refractories up to 100 times contributes to the disequilibrium in the materials as they, in fact, represent multi-stage alteration products.

The oxygen partial pressure was lower in basic lined ladles[1] as indicated by the low contents of FeO and MnO in the ladle slag.

The change in chemical composition of the sprayed tundish lining during casting is caused by mechanical admixture (i. e. infiltration and penetration) of tundish slag. The relative decrease of the periclase/forsterite ratio is due to periclase loss rather and to formation of tephroitic olivine. Evidence for formation of forsterite through the reaction

$$\mathrm{SiO_2}_{\ell}^{\mathrm{slag}} + \mathrm{MgO}_{\mathrm{s}}^{\mathrm{per}} \rightleftharpoons \mathrm{Mg_2SiO_4}_{\mathrm{s}}$$

could *not* be found.

The high concentrations of MnO in the tundish slag result in formation of Mn-rich olivine via the reaction

$$\mathrm{MnO}_{\ell}^{\mathrm{slag}} + \mathrm{SiO_2}_{\ell}^{\mathrm{slag}} + \mathrm{MgO}_{\mathrm{s}}^{\mathrm{periclase}} \rightleftharpoons (\mathrm{Mg,Mn})_2\mathrm{SiO}_{4\mathrm{s}} \ .$$

Tephroite can also form as a result of crystallization from the molten tundish slag without participation of periclase. Indirectly, however, MgO was introduced through periclase dissolution into the acid tundish slag.

[1] For deep desulphurization, which is performed in basic lined ladles, also low oxygen partial pressures have to be maintained.

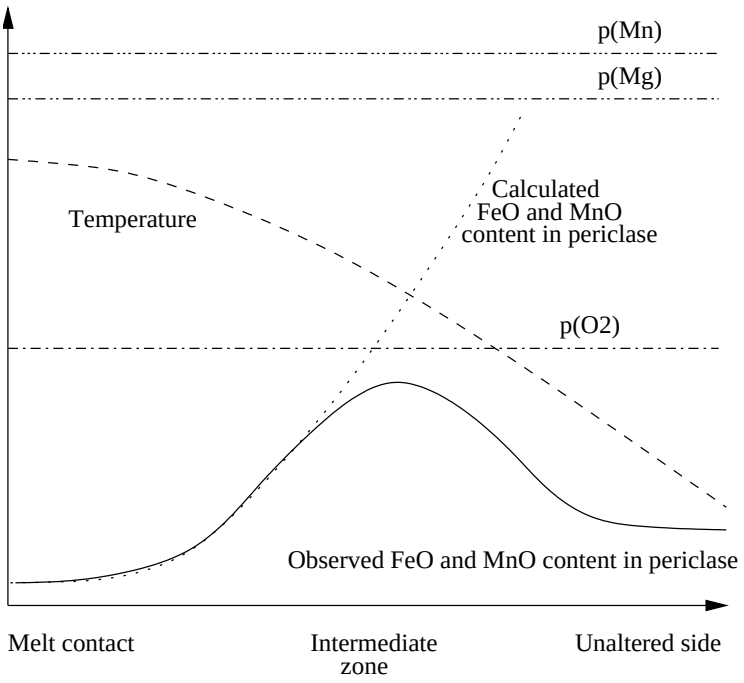

Figure 11.1: Sketch illustrating the variation of temperature, FeO and MnO contents of olivine and the composition of the gas phase across the sprayed tundish lining. The vapor pressures of Fe, Mn, and O_2 are assumed to be externally buffered by the steel melt. With decreasing temperature, an increase in FeO and MnO content in the periclase is calculated. The velocity of the incorporation of Fe and Mn into the periclase, however, is too low in the unaltered side. The periclase remains unaltered in this part of the tundish lining.

Spinel forms as product of the reaction

$$MgO^{per} + Al_2O_3^{slag,(inclusion?)} \rightleftharpoons MgAl_2O_4 \,.$$

Alumina participating in the reaction occurs dissolved in the tundish slag, but may also be supplied by uprising alumina particles from the steel melt. The spinel analyzed adjacent to the tundish lining contains up to 3.5 mol% hercynite component. In equilibrium with the steel melt at 1600°C, the coexisting spinel contains only <1 mol% hercynite component. The occurrence of a spinel with 3.5 mol% points to a temperature of formation of the spinel of less than 1600°C or/and an oxygen partial pressure exceeding $10^{-14.25}$ bar.

The periclase in the intermediate zone contains notable amounts of iron and manganese. The enrichment in Fe and Mn at distance to the interface with the steel melt is attributed to the reaction between the periclase and a gas phase rich in Fe and Mn. With decreasing temperature towards the central part of the disposable lining, an increase of the MnO and FeO concentration in the periclase is expected to occur[2] which is reflected in the increase of FeO and MnO in the periclase of the intermediate zone (see Fig. 11.1). The increase in FeO and MnO in the intermediate zone reflects this reaction.

Figure 11.1 is a sketch illustrating the relations between FeO and MnO contents in the periclase, the temperature, and the externally buffered partial pressures of Fe, Mn, and O_2 across the disposable tundish lining. The temperature profile is probably not linear since the porosity of the sprayed tundish lining decreases towards the steel melt contact. The MnO and FeO contents in the periclase increase with decreasing temperature. Therefore, an increase

[2]The composition of the gas phase is assumed to be buffered by the steel melt at 1873 K.

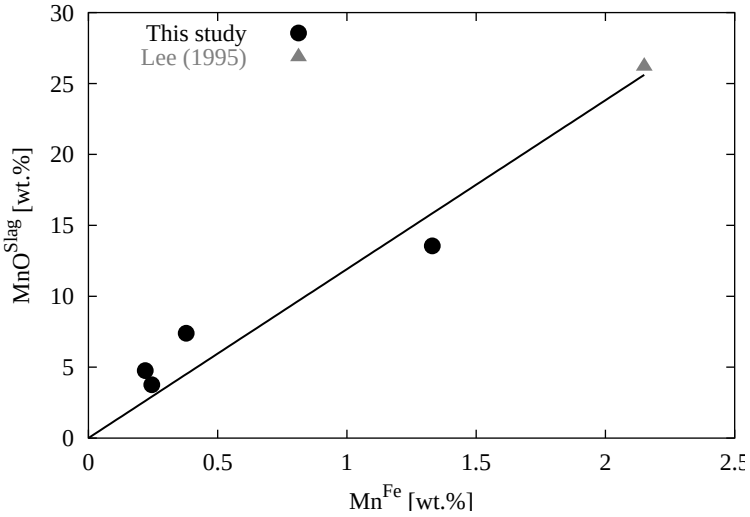

Figure 11.2: Plot of the MnO concentration in the tundish slag (XRF analyses) vs. Mn concentration in the steel melt. The MnO content in the slag correlates with the Mn content in the steel bath. The correlation is expressed by the function $MnO^{Slag} = 11.9 \times Mn^{Fe}$.

in MnO and FeO towards the central part was observed. Since the kinetics of Fe- and Mn-incorporation into the periclase is too slow in the unaltered side, no or only minor alteration of periclase is observed in this part of the tundish lining.

The assumption, that the composition of the gas phase is buffered by the steel melt throughout the entire tundish lining, however, is probably not realistic. A gradient in the gas phase composition and oxygen partial pressure is more likely. As a first approximation, however, the model of an externally buffered gas phase gives hints about the direction of reactions in the refractory.

The high MnO content which was generally detected in the tundish slag is caused by redox reaction between Mn dissolved in the steel melt and silica of the tundish slag:

$$2\,Mn_\ell + SiO_{2\ell} \rightleftharpoons 2\,MnO_\ell + Si_\ell \; .$$

Silica is reduced by Mn to Si-metal and MnO remains in the liquid silicate melt. The observation that silica-rich refractories are attacked by Mn-rich steel melts was already published by Rait (1943, in Lee, 1995) and Shultz (1979). Slag carry-over from the ladle is *not* the reason for the increase in MnO content in the tundish slag. It was shown that reduced activities of Mn and Si in the steel melt result in a decrease of the oxidation potential of the system Mn-MnO and an increase in the oxidation potential of the system Si-SiO_2 (see also White, 1974). The increase of the MnO content in the slag decreases the viscosity of the silicate melt (Lee, 1995) which results in an increase of the infiltration depth into the refractory. The MnO/Mn ratio[3] was calculated by linear regression to 11.9±0.9 (Fig. 11.2).

Figure 11.2 illustrates that it is possible to predict the approximate MnO concentration in the tundish slag. However, EPMA analyses of tundish slag revealed the slag to be very heterogeneous in composition. An experimental study on the equilibrium between Mn-containing steel and Mn-rich silicate melt (at defined oxygen partial pressure) would be useful to obtain informations about the activity coefficient of MnO in high-MnO silicate

[3]MnO in the slag, Mn in the melt, data in wt.%.

melts. Then it would also be possible to predict the MnO concentration in silicate phases in equilibrium with the MnO-rich slag.

The empiric data presented in this study indicate that the MnO concentration in the olivine is equal to the MnO-content of the slag (i. e. D = 1.0, at crystallization temperatures of the olivine).

Olivine in the sprayed tundish lining undergoes solid state reduction of the fayalite component. The reduction begins in the intermediate zone and proceeds towards the steel melt contact. The iron metal which is one of the reaction products remains entrapped within the forsterite host. No silica which would mechanically destabilize the forsterite has formed during this reaction.

Two different reduction mechanisms are inferred. The first mechanism includes the formation of gaseous SiO. The second reduction mechanism is driven through substitution of ferrous iron by Mg from the gas phase. The vapor pressure of periclase is considerably high at low oxygen partial pressures. At 1873 K and an oxygen partial pressure of $10^{-14.25}$ bar, a Mg_g partial pressure of as high as 3 mbar was calculated.

Which of these two mechanisms is predominant is difficult to decide. The second mechanism is favored because decay of periclase was actually observed, whereas no indication was detected for the decomposition of forsterite. The calculated fayalite content in equilibrium with the Mg-rich gas phase is in the range of less than 0.01 mol%, i. e. the resultant olivine is almost pure forsterite. This corresponds to a measured composition of up to 99.3 mol% forsterite and only 0.7% fayalite. Integrating analysis of silicate and dispersed iron metal, however, adversly affected the measurement of the olivine composition.

The outstanding result is that olivine with small amounts of fayalite is *not* destabilized through formation of silica melt. The reduced olivine is a very pure forsterite. The reduction results in exsolution of dispersed iron metal blebs. Evaporation of periclase from the tundish lining and a resultant high Mg-vapor pressure shifts the equilibrium towards the forsterite end-member. The olivine, in turn, is a sink for Mg and hence destabilizes the periclase.

The clogging is composed of corundum, calcium aluminate, spinel, and a CAS-rich vitreous phase. Al_2O_3, SiO_2, CaO and MgO are the major chemical components in the deposits. The occurrence of a Ca- and Al-rich vitreous phase was also reported by Gaye et al. (1994). The vitreous phase is a mixture of calcium aluminate phases and gehlenite with a melting point around 1530°C, well below the minimum of the temperature in the tundish.

The occurrence of spinel in the clogging is always closely associated to the unstoichiometric vitreous CAS-phase which occurs as matrix between octahedra of spinel. The spinel has probably crystallized from the vitreous matrix during solidification (see Gaye et al., 1994). The hercynite content of the spinel in the clogging is generally below 2 mol%. Only in some oxidized samples, hercynite-rich spinel was detected. This spinel is not assumed to be in thermodynamic equilibrium with the steel melt. The occurrence of hematite in the oxidized clogging is evidence for secondary oxidation. This implies that the composition of the samples could change after casting was finished. The red glowing hot submerged entry nozzles are exposed to air and slowly cool down within a time span of approximately 30 min. The FeO content of spinel, which may crystallize on air within the Ca-Al-rich matrix, can be taken as tracer to detect secondary alteration under oxidizing conditions.

The oxygen isotope composition of the clogging in steel plant A varies in a wide range between +5‰ and +14‰. Atmospheric oxygen and BOF process oxygen are, most probably, *not* the source for the oxygen in the alumina of the inclusion precipitates! Values in the range of +24‰ would be expected in case of atmospheric or BOF process oxygen as source for the oxygen in the precipitates. This result implies that the stirring of the melt in the ladle effectively removes deoxidation particles. The use of purged shroud tubes and SENs and the protection of the melt with slags largely avoids re-oxidation by air oxygen.

The materials which are in contact with the steel bath in the ladle (+17 to +20‰) do probably not contribute to the formation of oxide inclusions. These data, however, are preliminary, and a more detailed invistigation is necessary to map the isotopic composition of the different refractories and slags used in the ladle.

The oxygen isotopic composition of periclase of the sprayed tundish lining (+13.7‰) resembles the maximum $\delta^{18}O$ values observed in the clogging. Isotope measurements on various periclase raw materials showed that these are not homogeneous with respect to isotopic composition. Most periclase samples vary between +7 and +18‰ with an average at +11‰.

It was also shown that periclase evaporates under reducing conditions. The oxygen which is liberated during this reaction can contribute to the formation of non-metallic inclusions. Borgianni and Casella (1993, *in* Bannenberg, 1995) showed in laboratory experiments that alloyed Al is oxidized due to redox reaction between a periclase lining and the steel bath. The best results, with respect to redox reaction with the alloyed Al, were obtained with pure CaO refractories[4]. This clearly shows that periclase does contribute to the oxidation of alloyed Al.

Thus it is inferred that periclase in the tundish, and possibly in the ladle, contributes the *major part* of the oxygen required for the formation of non-metallic inclusions. The silica-rich slag used in the tundish acts, in addition, as oxygen pump through reduction of silica. Not only Mn, but also Al can reduce silica in the slag (see Bannenberg, 1995). The tundish slag, however, is enriched in ^{18}O relative to the clogging which contradicts the hypothesis that ladle slag reduction leads to the formation of alumia inclusions.

It was shown by Dohmen et al. (1998) that olivine evaporates under reducing conditions to Mg, SiO, and O_2. The conditions in the tundish are more reducing and the temperatures are higher than in the experiments conducted by Dohmen et al. (1998). The evaporation of olivine is thus inferred to be also a possible source for the formation of non-metallic inclusions.

The SEN bottom side precipitates in steel plant A exhibit a zonation in the oxygen isotopic composition. The zonation along the bottom side is interpreted to be a record of the "inclusion history". The precipitates at the contact interface with the SEN are enriched in ^{18}O relative to the precipitates at the steel melt contact. The following model is envisaged to explain this zonation: The first precipitates are inclusions that form by oxidation of Al through oxygen liberated from periclase. These inclusions are similar in isotope composition than the periclase used in the tundish. With increasing casting time, the contribution

[4] CaO was not reduced by alloyed Al.

of olivine to the formation of the inclusions increases. The δ^{18}O values of the inclusions formed by oxidation of Al by oxygen released from the olivine are thus in the range of +5‰. More data are necessary to establish this model. Additionally, inclusions should be measured *in-situ* in the steel slab to monitor the isotopic composition of the inclusions during casting.

All these considerations base on the assumption that isotopic fractionation between coexisting phases is negligible at temperatures as high as 1550–1600°C. Unfortunalety, there are no high temperature experimental data for refractory phases available to verify this assumption. The oxygen isotope partition is usually expressed by a function of the form:

$$1000 \ln \alpha_{\mathrm{a-b}} = \frac{\mathrm{A} \times 10^6}{\mathrm{T}^2} + \mathrm{B} \; .$$

The equations reported are, in most cases, only valid for a certain temperature range. With $B \neq 0$ a partition even at infinitly high temperature is indicated. This contradicts theoretical considerations.

It was shown that low-temperature hydration of periclase to brucite and dehydration of brucite at elevated temperatures dos most probably *not* lead to a formation of periclase depleted in ^{18}O relative to the initial composition of the periclase educt. The isotopically "light" precipitates analyzed in steel plant B (average of +2.7‰) may be a product of kinetically controlled isotope fractionation.

The results presented show that more oxygen isotope measurements are necessary to be able to draw a more detailed picture of the origin and the development of inclusions and precipitates during casting.

Chapter 12

Summary and conclusions

Figure 12.1 is a drawing which illustrates the interaction between tundish lining, tundish slag and the steel melt. Periclase of the tundish lining is vaporized. The oxygen which is liberated is bond in alumina inclusions. The high-Mg vapor pressure and reducing conditions result in reduction of the fayalite component in olivine. Iron metal is exsolved and the lattice position of ferrous iron is occupied by magnesium from the vapor phase. Forsterite vaporizes and contributes to the formation of non-metallic inclusions. Alloyed aluminum and manganese reduce silica in the slag. Magnesium vapor may migrate towards the contact between permanent and disposable lining and lead to the formation of spinel.

An important result of this study is that periclase is the major source of oxygen in the clogging in the SEN bore. The interaction between tundish lining, slag and steel melt was investigated in detail. Periclase of the ladle may also contribute to the increase in oxygen content in the steel melt. Atmospheric oxygen and endogeneous deoxidation particles are most probably *not* the major source for non-metallic precipitates and inclusions. The isotopicall "light" δ^{18} values obtained in steel plant B remain enigmatic. No conclusive model was found yet to explain the δ^{18} values of +1.4 to +5.8‰ in the clogging of steel plant B.

This was a first reconnaissance on the oxygen isotopic composition of oxide deposits and refractories used in steel making processes. As a result of a great number of isotope studies during the last four decades, it is nowadays possible to characterize in detail the physico-chemical conditions in natural systems that are not directly accessible. We know more about the oxygen isotope compositions of pre-solar corundum grains, which are older than the earth, than about corundum in high-alumina refractories. Oxygen isotope studies in combination with *state-of-the-art* petrographical methods and conventional engineering methods could provide a new approach for solving problems in the field of steel making.

12.1 Proposal for further investigations

It was shown by Dohmen et al. (1998) and also inferred from the results of this study that mass transfer via a gas phase is an important mechanism at high temperatures and reducing conditions. It would be very interesting to explore the reactions between steel melt and refractories in Knutsen cell experiments. The proposed set up is illustrated in Figure 12.2.

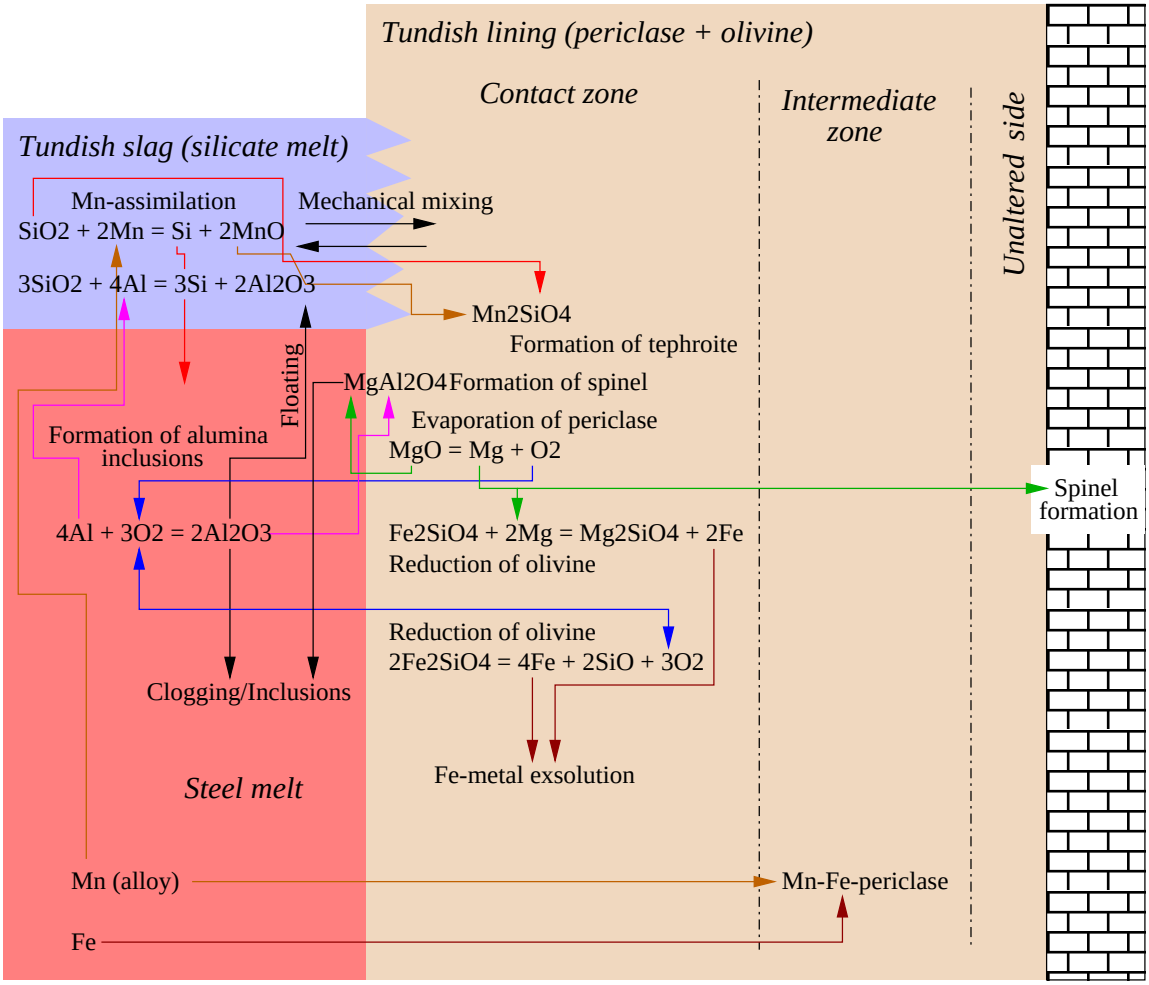

Figure 12.1: Drawing illustrating the interaction between tundish lining (*right*), melt (*bottom left*) and tundish slag (*top left*).

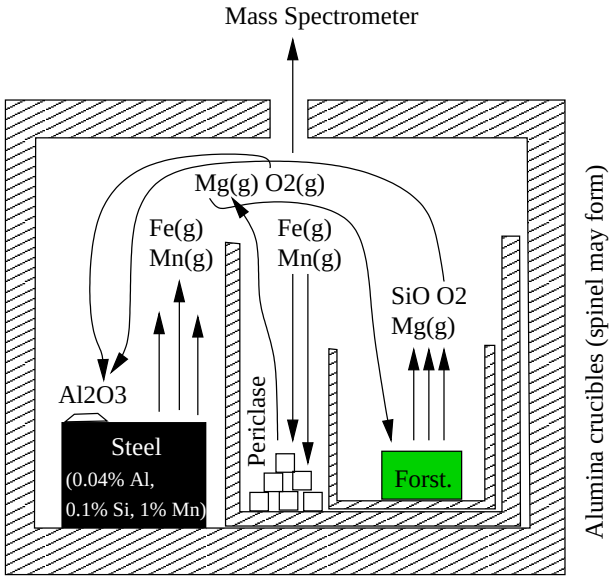

Figure 12.2: Proposed set up in the Knutsen cell experiment. The solid three phases are steel (0.04% Al, 1% Mn, 0.2% Si), pure periclase and an upper mantle forsterite of the raw material. The operation temperature should be in the range up to 1450°C. A temperature below the steel liquidus is recommendable to avoid hazardous problems with liquid steel in the cell. The gas phase composition (Mg, Fe, Mn, and SiO) is monitored by mass spectrometry. Periclase should evaporate and incorporate some Fe and Mn, depending on the temperature of operation. Olivine should be reduced without a volume decrease (substitution of Fe by Mg) or with decrease of volume (evaporation of the fayalite component). The composition of the steel will change throughout the experiment through formation of alumina and loss of Fe and Mn to the gas phase. Therefore the volume of the steel block should be $\gg$ than the volumes of periclase and olivine. The alumina crucible should behave chemically inert. Formation of spinel, however, may occur.

Phases participating in the reaction are separated and diffusive exchange is excluded. Reaction between periclase and the alumina crucible may lead to the formation of spinel. Therefore a “thick” layer of periclase is recommendable. The temperature is varied between approximately 700°C up to more than 1400°C. The data a temperature of 1600°C can be extrapolated. It might be hazardous to run the experiment with liquid iron at extremely high temperatures.

With this experimental set up, a detailed investigation of the interaction between gas phase and solids is possible. The phases are characterized using electron microprobe analysis and TEM (Fe-exsolution in forsterite). The phases can isotopically be analyzed (including the crucible material). The alumina should carry the oxygen isotope value of the oxygen source, which is inferred to be periclase. The isotopic compositions of the starting materials should be all different and should not be close to +23.5‰. The first experiments, however, may be conducted with only two reactants, but should always include the steel. The presence of the steel with defined Al concentration is necessary to control the oxygen partial pressure.

Bibliography

Asprey, L. B. (1976). The preparation of very pure fluorine gas. *Journal of Fluorine Chemistry*, 7:359–361. 25

Bannenberg, N. (1995). Demands on refractory material for clean steel production. In *Global Development of Refactories*, pages 36–59, Japan. Technical Association of Refractories. 3, 13, 105, 116

Bednarek, E. (1995). LASCO: Development of Calcium Metallurgy. In McPherson, N. A. and McLean, A., editors, *Non-Metallic Inclusions in Continuously Cast Steel*. The Iron and Steel Society, Inc. 13

Berger, R., Köhler, K.-U., and Schütt, H. (1989). Umstellung der Verteiler bei den Stranggießanlagen der Hoesch Stahl AG auf monolithische Dauerfutter. *Stahl und Eisen*, 110(11). 16

Berman, R. G. (1988). Internally-consistent thermodynamic data for stoichiometric minerals in the system Na_2O-K_2O-CaO-MgO-FeO-Fe_2O_3-Al_2O_3-SiO_2-TiO_2-H_2O-CO_2. *Journal of Petrology*, 29:445–522. 104

Birch, R. E. and Wicken, O. M. (1949). Magnesite and related minerals. In Dolbear, S. H. and Bowels, O., editors, *Industrial Minerals and Rocks*, pages 521–541. The American Institute of Mining and Metallurgy Engineers, New York. 1156 pp. 100

Bottinga, Y. (1968). Calculation of fractionation factors for carbon and oxygen isotopic exchange in the system calcite-carbon dioxide-water. *J. Phys. Chem.*, 72:800–808. 101

Broß, R. (1995). *Mineralreaktionen in basischen Feuerfestmassen*. PhD thesis, Rheinische Friedrich-Wilhelms-Universität, Bonn. 196 pp. 49, 51, 66, 70, 78, 81, 82, 83, 109

Buhr, A. (1996a). *Tonerdereiche Feuerfestbetone für den Einsatz im Stahlwerk*. PhD thesis, Rheinisch-Westfälische Technische Hochschule, Aachen. 14, 15

Buhr, A. (1996b). Tonerdereiche Feuerfestbetone für den Einsatz im Stahlwerk. *Stahl und Eisen*, 116:59–66. 14, 15

Buhr, A. and Koltermann, M. (1996). Neue feuerfeste Roh- und Werkstoffe mit mehr als 60% Al_2O_3–Entwicklungsrichtungen und Versuche in Torpedo und Staglgießpfannen. In *39. Internationales Feuerfest-Kolloquium*, pages 161–165, Aachen. 14, 15

Buseck, P. R. (1992). Principles of transmission electron microscopy. In Buseck, P. R., editor, *Minerals and reaction at the atomic scale: Transmission electron microscopy*, Reviews in Mineralogy. Mineralogical Society of America. 39

Cornides, I. and Kusakabe, M. (1977). Preparation of carbon dioxide from magnesite for isotopic analysis. *Fresenius Zeitschrift für Analytische Chemie*, 287:310–311. 100

Deer, W. A., Howie, R. A., and Zussman, J. (1966). *An introduction to the rock-forming minerals*. Longman Scientific & Technical. low priced edition, 528 pp. 49

Dohmen, R., Chakraborty, S., Palme, H., and Rammensee, W. (1998). Solid-solid reactions mediated by a gase phase: An experimental study of reaction progress and the role of surfaces in the system olivine+iron metal. *American Mineralogist*, 83:970–984. 107, 108, 109, 116, 118

Dole, M., Lane, G. A., Rudd, D. P., and Zaukelies, D. A. (1954). Isotopic composition of atmospheric oxygen and nitrogen. *Geochimica et Cosmochimica Acta*, 6:65–78. 88

Droop, G. T. R. (1987). A general equation for estimating Fe^{3+} concentrations in ferromagnesian silicates and oxides from microprobe analyses, using stochiometric criteria. *Mineralogical Magazine*, 51:431–435. 76, 81, 84

Gaye, H., Gatellier, C., and Riboud, P. V. (1994). Control of endogeneous inclusions in Al-killed and low-Al steels. In *Proceeding of the Ethem T. Turkdogan Symposium: Fundamentals and Analysis of new and Emerging Steelmaking Technologies*, pages 113–124, Pittsburgh, U.S.A. Iron and Steel Society, Inc.; The Minerals, Metals and Materials Society; U.S. Steel Group of USX Cooperation. 3, 13, 115

Golyshev, S. I., Padalko, N. L., and Pechenkin, S. A. (1981). Fractionation of stable isotopes in carbonate systems. *Geochem. International*, 10:85–99. 101

Gotthelf, D. (1999). *Gießtechnische Maßnahmen zur Verbesserung des Reinheitsgrades und zur Herabsetzung des Blasenfehlers kaltgewalzter IF-Stähle*. PhD thesis, Fakutlä für Bergbau, Hüttenwesen und Maschinenwesen der Technischen Universität Clausthal. 104 pp. 10, 13

Hagen, B. (2000). *Analyse von O-Isotopen zur Quantifizierung des Metamorphosepfades von Gesteinen des Sächsischen Granulitgebirges durch irm-MS in Kombination mit Laserfluorination*. PhD thesis, Mineralogisch-Petrologisches Institut und Museum der Rheinischen Friedrich-Wilhelms Universität, Bonn. in press. 23

Hansen, M. (1958). *Constitution of Binary Alloys*. Metallurgy and Metallurgical Engineering Series. McGraw-Hill Book Company, Inc., 2 edition. 1305 pp. 6, 7

Herbrich, P., Mörtel, G., and Hoernes, S. (1990). Der Anteil von schwerem Sauerstoff (^{18}O) in Sintermagnesia-Produkten. *Radex-Rundschau*, 2/3. 98, 100, 101, 102

Hoefs, J. (1996). *Stable Isotope Geochemistry*. Springer Verlag, 4 edition. 201 pp. 89

Holland, T. J. B. and Powell, R. (1998). An internally consistent thermodynamic data set for phases of petrological interest. *Journal of Metamorphic Geology*, 16:309–343. 104, 105, 107

Horbach, U., Rödl, S., Abratis, H., and Höfer, F. (1995). Strömungsuntersuchungen in geregelten verteilerausgüssen zur vermeidung von clogging. *Stahl und Eisen*, 115(11):71–76. 13

Horita, J. and Wesolowski, D. J. (1994). Liquid-vapor fractionation of oxygen and hydrogen isotopes of water from the freezing to the critial temperature. *Geochimica et Cosmochimica Acta*, 58:3425–3437. 97, 98

Huiquing, H. (1995). Development and application of scum weir for a tundish and exploration for its antislag erosion mechanism. In *Unified International Technical Conference on Refractories, Fourth Biennial Worldwide Conference on Refractories: Global Development of Refractories*, pages 285–292, Kyoto, Japan. The Technical Association of Refractories, Japan. 13

Hülsmans, A., Schmücker, M., Mader, W., and Schneider, H. (2000a). The transformation of andalusite to mullite and silica: Part i. Transformation mechanisms in $[001]_a$ direction. *American Mineralogist*, 85:980–986. 63

Hülsmans, A., Schmücker, M., Mader, W., and Schneider, H. (2000b). The transformation of andalusite to mullite and silica: Part i. Transformation mechanisms in $[100]_a$ and $[010]_a$ direction. *American Mineralogist*, 85:987–992. 63

Hultgren, R., Desai, P. D., Hawkins, D. T., Geisler, M., and Kelley, K. K., editors (1973). *Selected Values of the Thermodynamic Properties of Binary Alloys*. American Society of Metals. 104, 105, 107

Imagumbai, M. and Takeda, T. (1994). Influence of calcium-treatment on sulfide- and oxide-inclusions in continuous-cast slab of clean steel-dentrite structure and inclusions. *Iron and Steel Institute Journal (International)*, 34(7):574–583. 13

Jacobi, H., Ehrenberg, H.-J., and Wünnenberg, K. (1998). Reinheitsentwicklung verschiedener Stähle für Flach- und Rundprodukte. *Stahl und Eisen*, 118(11):87–95. 3, 13

Jesenák, V., Turčániová, L., and Tkáčová, K. (1997). Kinetic analysis of thermal decomposition of magnesite—influence of generated defects and their annealing. *Journal of Thermal Analysis*, 48:93–106. 104

Jones, R. H. and Danielson, L. R. (1997). A chondrule origin for dusty relict olivine in unequilibrated chondrites. *Meteoritics and Planetary Science*, 32:753–760. 54

Klaassen, M. (1997). Verschleißmechanismus von tonerdereichen Feuerfestbetonen in Stahlgießpfannen. Master's thesis, Institut für Kristallographie, Rheinisch-Westfälische Technische Hochschule Aachen. unpublished, 107 pp. 9, 14, 15, 16, 70

Koeppel, C. (1938). *Feuerfeste Baustoffe silikatischer und silikathaltiger Massen*, volume 18 of *Chemie und Technik der Gegenwart*. Verlag von S. Hirzel, Leipzig. 296 pp. 110

Koltermann, M., Selveit, A., and Scheel, R. (1985). Olivin als feuerfester Baustoff. *Stahl und Eisen*, 105:683–688. 62, 66, 109

Konopicky, K. (1957). *Feuerfeste Baustoffe: Herstellung ung Verwendung*, volume 14 of *Stahleisen-Bücher*. Verlag Stahleisen mbH, Düsseldorf. 51, 100, 108

Krauss, A. (1902). *Eisen-Hütten-Kunde: Das Roheisen*, volume 1 of *Sammlung Göschen*. G. J. Göschen'sche Verlagshandlung, Leipzig. 85 pp. 8

Lee, Y.-C. (1995). Effect of manganese oxide on the corrosion behaviour of alumina-silica-graphite shroud nozzle in continous casting. In *Unified International Technical Conference on Refractories, Fourth Biennial Worldwide Conference on Refractories: Global Development of Refractories*, pages 101–108, Kyoto, Japan. The Technical Association of Refractories, Japan. 114

Levin, E. M., Robbins, C. R., and McMurdie, H. F. (1964). *Phase Diagrams for Ceramists*. The American Ceramic Society. 47, 86

Mallard, W. G. and Linstrom, P. J., editors (2000). *NIST Standard Reference Database Number 69*. National Institute of Standards and Technology, Gaithersburg MD, 20899 (http://webbook.nist.gov). 104, 105, 107, 108

Mattey, D. P., Lowry, D., and MacPherson, C. (1994). Oxygen isotope composition of mantle peridotites. *Earth and Planetary Science Letters*, 128:231–241. 89

McPherson, N. A. and McLean, A., editors (1995). *Non-Metallic Inclusions in Continuously Cast Steel*, volume 7 of *Continous Casting*. The Iron and Steel Society, Inc. 59

Merrit, D. A. and Hayes, J. M. (1994). Factors controlling precision and accuracy in isotope-ratio-monitoring mass spectrometry. *Analytical Chemistry*, 66:2336–2347. 31

Miller, M. F., Franci, I. A., Sexton, A. S., and Pillinger, C. T. (1999). High precision δ^{17}O isotope measurements of oxygen from silicates and other oxides: method and application. *Rapid Communications in Mass Spectrometry*, 13:1211–1217. 25, 26, 42

Ozgu, M. R. (1996). Continuous caster instrumentation: State-of-the-art review. *Canadian Metallurgy Quarterely*, 35(3):199–223. 10

Pack, A. and Hoernes, S. (2000a). The behavior of olivine in refractories used in steel making processes—Thermodynamic considerations. In Rammlmair, D., Mederer, J., Oberthür, T., Heimann, R. B., and Pentinghaus, H., editors, *Applied Mineralogy in Research, Economy, Technology, Ecology and Culture*, volume 2, pages 875–878. A. A. Balkema. 5

Pack, A. and Hoernes, S. (2000b). Solid state reduction of olivine used in basic refractories in steel making processes. *European Journal of Mineralogy*, 12:143. Beiheft zur 75. Jahrestagung der Deutschen Mineralogischen Gesellschaft vom 24. bis 29. September 2000 in Heidelberg, abstract. 5

Pack, A., Hoernes, S., Broß, R., Göbbels, M., and Buhr, A. (2000). IR-laser fluorination as tool to determine the origin of oxide inclusions in continuously casted steel—An interdisciplinary approach. In Rammlmair, D., Mederer, J., Oberthür, T., Heimann, R. B., and Pentinghaus, H., editors, *Applied Mineralogy in Research, Economy, Technology, Ecology and Culture*, volume 2, pages 617–620. A. A. Balkema. 5

Pelton, A. D., Eriksson, G., Krajewski, D., Göbbels, M., and Woermann, E. (1998). Measurement and thermodynamic evaluation of phase equilibria in the Mg-Ti-O system. *Zeitschrift für Physikalische Chemie*, 207:163–180. 108, 110

Pleschiutschnigg, F.-P. (1989). *Das Verhalten oxidischer Einschlüsse sowie ihre Kontrolle in Al-beruhigtem Stahl während der Stahlerzeugung und de Stranggießens*. Fakultät für Bergbau, Hüttenwesen und Geowissenschaften, RWTH Aachen, Germany. 3, 13

Prosser, S. J. (1998). *Europa Scientific: Calculation Manual*. PDZ Europa. 31 pp. 4, 43

Putnis, A. (1992). *Introduction to Mineral Sciences*. Cambridge University Press. 39

Rait, J. R. (1943). Castin pit refractories as a source of non-metallic inclusions in steel. *Transactions of the British Ceramic Society*, 42:57–90. 114

Ricketts, J. A. (2000). How a blast furnace works. published in the world wide web at http://www.steel.org/learning/howmade/blast_furnace.htm. 8

Robie, R. A., Hemmingway, B. S., and Fisher, J. R. (1979). *Thermodynamic Properties of Minerals and Related Substances at 289.15 K and 1 Bar (10^5 Pascal) Pressure and at Higher Temperatures*. Geological Survey bulletin 1452. United States Geological Survey. 456 pp. 104, 107

Roth, R. S., Negas, T., and Cook, L. P., editors (1982). *Phase diagrams for ceramists*, volume 4. The American Ceramic Society. 47

Savin and Lee (1988). Isotopic studies of hydrous phyllosilicates. In Bailey, S. W., editor, *Hydrous Phyllosilicates (exclusive of micas)*, volume 19 of *Reviews in Mineralogy*, pages 189–233. Mineralogical Society of America. 97, 100, 101

Sawada, I., Okazawa, K., Takeuchi, E., Shigematsu, K., and Tanaka, H. (1995). Development and application of simulator for analyzing molten steel flow and inclusion behaviour in continuous caters. Technical Report 67, Nippon Steel Technical Report. 13

Schneiderhöhn, H. (1962). *Erzlagerstätten—Kurzvorlesungen zur Einführung und Wiederholung*. Gustav Fischer Verlag, Stuttgart, 4 edition. 371 pp. 14

Sharp, Z. D. (1990). A laser based microanalytical method for the in-situ determination of oxygen isotope ratios of silicates and oxides. *Geochimica et Cosmochimica Acta*, 54:1353–1357. 23

Sharp, Z. D. (1995). Oxygen isotope gechemistry of the Al_2SiO_5 polymorphs. *American Journal of Science*, 295:1058–1076. 95

Sheppard, S. M. F. and Schwarz, H. P. (1970). Fractionation of carbon and oxygen isotopes and magnesium between coexisting metamorphic calcite and dolomite. *Contributions to Mineralogy and Petrology*, 26:161–198. 101

Shultz, R. L. (1979). Attack of alumino-silicate refractories by high manganese steel. *Steelmaking Proceedings*, 62:232–235. 114

Steinmetz, E., Lindenberg, H.-U., Mörsdorf, W., and Hammerschmid, P. (1977). Ausbildungsformen und Entstehung von Aluminiumoxiden in Rohblöcken und Stranggußbrammen. *Stahl und Eisen*, 97:1154–1159. 59

Thiemens, M. H. (1999). Mass-independent isotope effects in planteary atmospheres and the early solar system. *Science*, 283:341–345. 42

Thiemens, M. H., Jackson, T., Zipf, E. C., Erdman, P. W., and van Egmond, C. (1995). Carbon dioxide and oxygen isotope anomalies in the mesosphere and stratosphere. *Science*, 270:969–972. 42

Trojer, F., Obst, K.-H., and Münchberg, W. (1981). *Mineralogie basischer Feuerfest-Produkte*. Number 12 in Applied Mineralogy. Springer-Verlag, New York. 15, 51, 104, 105, 108, 110

Turčániová, L., Paholič, G., and Mateová, K. (1996). Stimulating the thermal decomposition of magnesite. *Thermochimica Acta*, 277:75–84. 104

Verein Deutscher Eisenhüttenleute, editor (1989). *Stahlfibel*. Verlag Stahleisen mbH, Düsseldorf. 135 pp. 6, 10

von Witzleben, M., Kollenberg, W., and Bannenberg, N. (1996). Untersuchungen der Reaktion zwischen Feuerfestbeton und Spritzmasse im Tundish. *Stahl und Eisen Special*, pages 111–117. XXXIX. Internationales Feuerfestkolloquium, Aachen, Germany. 16, 17, 107, 110

Wedler, G. (1987). *Lehrbuch der Physikalischen Chemie*. VCH Verlagsgesellschaft mbH, Weinheim, 3rd edition. 924 pp. 103

White, J. (1974). The thermodynamic stability of oxide refractories. *Journal of the Australian Ceramic Society*, 10:1–4. 114

Wiechert, U., Ionov, D. A., and Wedepohl, K. H. (1996). Spinel peridotite xenoliths from Atsagin-Dush volcano, Dariganga lava plateau, Mongolia: a record of partial melting and cryptic metasomatism in the upper mantle. *Contributions to Mineralogy and Petrology*, X:Y–Z. contributed. 89

Wijk, O. (1995). Inclusion engineering. In *Scaninject VII, Part I*, pages 35–67, Luleå, Schweden. MEFOS. 7th International Conference on Refining processes. 3, 9

Wintz, M., Bobadilla, M., Lehmann, J., and Gaye, H. (1995). Experimental study and modelling of the precipitation of non-metallic inclusions during solidification of steel. *ISIJ Inertational*, 35(6). 10

Young, E. D., Fogel, M. L., Rumble III, D., and Hoering, T. C. (1998). Isotope-ratio-monitoring of O_2 for microanalysis of $^{18}O/^{16}O$ and $^{17}O/^{16}O$ in geological materials. *Geochimica et Cosmochimica Acta*, 62(18):3087–3094. 31, 33

Zheng, Y. F. (1994). Zheng, y.f. (1994) oxygen isotope fractionation in metal monoxides. *Mineralogical Magazine*, 58:1000–1001. 101

Zimmermann, A. (1974). *Die Entstehung oxidische Einschlüsse im Stahl unter besonderer Berücksichtigung des Einflusses feuerfester Materialien des Systems SiO_2-Al_2O_3*. PhD thesis, Fakultät für Bergbau und Hüttenwesen und Maschinenwesen der Technischen Universität Clausthal (Germany). 3

Appendix A

Source code of Intefix

 denotes a line break made for this print out only.
 is absent in the actual source code. The source code and binaries for *Windows9x/NT* and *Linux* are also part of the attached CD-ROM.

```
{

/*  Programm zum numerischen Integrieren von Zahlenkolonnen,
    letzte Aenderung: 23.07.2000              */

#include <stdio.h>
#include <string.h>

main()
{
  /* die Zeiger *rawdata, *outputdata und *logfile verweisen
     auf eine Datei (FILE)                                  */
  FILE *rawdata, *outputdata, *logfile, *clipboard;

  /* die folgenden Variablen koennen positive Werte
     zwischen 0 und 4294967296 haben                        */

  unsigned long int

    /* Ionenstroeme I: */
    I_32 = 0,
    I_33 = 0,
    I_34 = 0,
    I_mittel32_unt1 = 0,
    I_mittel33_unt1 = 0,
    I_mittel34_unt1 = 0,
    I_mittel32_unt2 = 0,
    I_mittel33_unt2 = 0,
```

```
  I_mittel34_unt2 = 0,

  /* Produkte von Strom*Zeit=Peakflaechen */
  It_32_raw = 0,
  It_33_raw = 0,
  It_34_raw = 0,
  It_32 = 0,
  It_33 = 0,
  It_34 = 0,\graphicspath

  /* Hilfsvariable */
  x0 = 0, x = 0,
  y0 = 0, y = 0,
  z0 = 0, z = 0;

/* die folgenden Variablen koennen positive Werte
   zwischen 0 und 65535 haben                                  */

unsigned int

  /* Zeiten */
  t = 1,
  t_peak_anf,
  t_peak_end,
  t_scan,


  /* Peaknummern */
  n = 1, N = 1;


/* die folgende Variable ist eine Zeichenkette aus ASCII
   Zeichen (0-255), max. 20 Zeichen */

char
  inputfilename[10],
  rawdatafilename[20],
  scan[10],
  m32[10],
  m33[10],
  m34[10];

/* Beginn der Eingabe von der Tastatur                         */

system("clear");
```

```
  printf("\t\t\t INTEFIX\n
          \twritten by Andreas Pack (Version July 2000)
          \n
         ");
  printf("\nFilename of rawdata\t\t: ");
  scanf("%s", &inputfilename);
  strcpy(rawdatafilename,inputfilename);
  strcat(rawdatafilename,".txt");
  rawdata = fopen(rawdatafilename, "r");
  if((rawdata) == NULL)
    {
      printf("\nERROR: Sorry, file %s could not be found in current directory!<br>
\n\n",rawdatafilename);
      exit(1);
    }
  else printf("\t\t\t\t  -> File %s is opened in read only mode\n",rawdatafilename
  printf("Begin peak\t\t\t: ");
  scanf("%u", &t_peak_anf);
  printf("\t\t\t\t  -> 1st background from %u s to %u s\n",t_peak_anf-10,t_peak_an

  printf("End peak\t\t\t: ");
  scanf("%u", &t_peak_end);
  printf("\t\t\t\t  -> Peak from %u s to %u s
          \t\t\t  -> 2nd background from %u s to %u s\n",
          t_peak_anf,t_peak_end,t_peak_end,t_peak_end+10);

  printf("Total number of peaks\t\t: ");
  scanf("%u", &N);
  printf("Scan time per sample\t\t: ");
  scanf("%u", &t_scan);



  /* Vorbereitung der Rohdaten. Loeschen der Zeilen mit String-
     ausdruecken. Die modifizierten Rohdaten werden in der
     Datei clipboard.txt gespeichert                              */

  clipboard = fopen("clipboard.txt", "w");
  if((clipboard) == NULL)
    {
      printf("\nERROR: Sorry, file clipboard.txt could not be created in<br>
current directory!\n\n");
      exit(1);
    }
  else printf("\t\t\t\t  -> Temporary file clipboard.txt is created succesfully\n"
```

```
  for(t=1 ; t<t_scan*N+N+1 ; ++t)
    {
   fscanf(rawdata, "%s %s %s", &m32, &m33, &m34);
      if(m32[0]=='B')
        {
          fscanf(rawdata, "%s %s %s", &m32, &m33, &m34);
        }
      else
        fprintf(clipboard,"%s\t%s\t%s\n",m32, m33, m34);
    };

  fclose(rawdata);
  fclose(clipboard);

  /* Beginn des eigentlichen Rechencodes                          */

  logfile=fopen("logfile.csv", "w");
  if((logfile) == NULL)
    {
      printf("\nERROR: Sorry, file logfile.csv could not be created in current<br>
             directory!\n\n");
      exit(1);
    }
  else printf("\t\t\t\t  -> Logfile file logfile.csv is created succesfully\n");

  outputdata = fopen("outputdata.csv", "w");
  if((outputdata) == NULL)
    {
      printf("\nERROR: Sorry, result file outputdata.csv could not be created<br>
in current directory!\n\n");
      exit(1);
    }
  else printf("\t\t\t\t  -> Result file outputdata.csv is created and opened<br>
             succesfully\n");

  printf("\t\t\t\t  -> Beginning numeric integration procedure\n\t\t\t\t     ");


  fprintf(outputdata,
          "File\tDate\tTyp\tNr.\tBeam1\tBeam2\tBeam3\tBeam1(BC)\tBeam2(BC)<br>
\tBeam3(BC)\tR33\tR34\tR17\tR18\tD17\tD18\tDiff\tD18(DC)\n"
          );

  /* Aeussere Schleife, N+1 Peaks werden durchlaufen              */

  clipboard = fopen("clipboard.txt", "r");
```

```
do
  {
    fprintf(logfile,"N %u\n", n);

    /* 1. Abschnitt: Bis zum Anfang des Untergrundes-I       */

    for(t=1 ; t<t_peak_anf-10 ; ++t)
      {
        fscanf(clipboard, "%u %u %u", &I_32, &I_33, &I_34);
        fprintf(logfile,"Pre-U1 %u,%u \n", t, I_32);
      };

    /* 2. Abschnitt: Untergrund-I                            */

    x0 = x = y0 = y = z0 = z = 0;
    for(t ; t<t_peak_anf ; ++t)
      {
        x0 = x , y0 = y, z0 = z;
        fscanf(clipboard, "%u %u %u", &I_32, &I_33, &I_34);
        x = x0 + I_32, y = y0 + I_33, z = z0 + I_34;
        fprintf(logfile,"U1 %u\n", t);
      };
    I_mittel32_unt1 = x / 10;
    I_mittel33_unt1 = y / 10;
    I_mittel34_unt1 = z / 10;

    fprintf(logfile, "U1: , %u, %u, %u\n",
            I_mittel32_unt1, I_mittel33_unt1, I_mittel34_unt1
            );

    /* 3. Abschnitt: Peak                                    */

    x0 = x = y0 = y = z0 = z = 0;
    for(t ; t<t_peak_end ; ++t)
      {
        x0 = x , y0 = y, z0 = z;
        fscanf(clipboard, "%u %u %u", &I_32, &I_33, &I_34);
        fprintf(logfile,"Peak %u\n", t);
        x = x0 + I_32, y = y0 + I_33, z = z0 + I_34;
      };
    It_32_raw = x;
    It_33_raw = y;
    It_34_raw = z;

    fprintf(logfile, "Peak(roh): , %u, %u, %u\n",
```

```
        It_32_raw, It_33_raw, It_34_raw
        );

/* 4. Abschnitt: Untergrund-II                              */

x0 = x = y0 = y = z0 = z = 0;
for(t ; t<t_peak_end+10 ; ++t)
  {
    x0 = x , y0 = y, z0 = z;
    fscanf(clipboard, "%u %u %u", &I_32, &I_33, &I_34);
    fprintf(logfile,"U2 %u\n", t);
    x = x0 + I_32, y = y0 + I_33, z = z0 + I_34;
  };
I_mittel32_unt2 = x / 10;
I_mittel33_unt2 = y / 10;
I_mittel34_unt2 = z / 10;

fprintf(logfile, "U2: , %u, %u, %u\n",
        I_mittel32_unt2, I_mittel33_unt2, I_mittel34_unt2
        );

/* 5. Abschnitt: Bis zum Ende des Scans                     */

for(t ; t<=t_scan ; ++t)
  {
    fscanf(clipboard, "%u %u %u", &I_32, &I_33, &I_34);
    fprintf(logfile,"Ende %u\n", t);
  }

/* 6. Abschnitt: Untergrundkorrektur und Ausgabe            */

/* Anweisungen sind schon Befehle fuer die Zellen in Excel
   oder StarOffice                                         */

It_32 = It_32_raw - (I_mittel32_unt1 + I_mittel32_unt2)/2
        * (t_peak_end - t_peak_anf);
It_33 = It_33_raw - (I_mittel33_unt1 + I_mittel33_unt2)/2
        * (t_peak_end - t_peak_anf);
It_34 = It_34_raw - (I_mittel34_unt1 + I_mittel34_unt2)/2
        * (t_peak_end - t_peak_anf);

fprintf(outputdata, "%s\t\t\t%2.0u\t%11.0u\t%11.0u\t%11.0u\t\t\t\t<br>
                    =I%.0u/H%.0ld\t=J%.0u/H%.0ld\t=K%.0u/2\t<br>
                    =(L%.0u-M%.0uˆ2)/2\t=(((M%.0u-M%.0u)/M%.0u+1)*<br>
                    (O%.0u/1000+1)-1)*1000\t=(((N%.0u-N%.0u)/N%.0u+1)*<br>
                    (P%.0u/1000+1)-1)*1000\n",
```

```
              inputfilename,
              n ,
              It_32, It_33, It_34,
              n+1, n+1,
              n+1, n+1,
              n+1, n+1, n+1,
              n+1, N+3, N+3, N+3,
              n+1, N+3, N+3, N+3);

      n++;
      printf(" +");
    }
  while (n<=N);
  fclose(clipboard);

  printf("\n");
  printf("\t\t\t\t  -> Background correction
          \t\t\t  -> Results successfully written to file outputdat.csv\n<br>
          \t\t\t\t  -> All files closed, finished! <-\n\n");

  fclose(outputdata);
  fclose(logfile);

  /* Ende des Programms                                          */

}
```

Appendix B

Sample List

Table B.1: Two sample of basic oxygen furnace process (BOF) oxygen were taken in steel plant A (BOF-A) and B (BOF-B).

Sample	Type	Description
BOF-A	O_2	Basic oxygen furnace (BOF) process oxygen; sample was taken in the oxygen plant; steel plant A
BOF-B	O_2	Basic oxygen furnace (BOF) process oxygen; sample was taken in the oxygen plant; steel plant B

Table B.2: List of a set of samples of raw materials used in refractories for steel making.

Sample	Type	Description
107	Periclase	producer: Harbison & Walker (USA); beige sinter pellets; Ø 10–20 mm
108	Periclase	origin: China (China 95); beige sinter pellets; Ø up to 50 mm
109	Periclase	origin: China (China 90); beige sitered pellets
110	Periclase	produced from sea water precipitated brucite; origin: USA (97% HLS); angular pellets; Ø 10–25 mm
112	Periclase	origin: Brasil (M10); angular pellets; Ø $\leq$5–35 mm, crushed sample dark gray
A-097	Olivine	olivine from the Åheim deposit, Norway; used as raw material of the sprayed tundish lining; fired at 800°C for 4 h; oxidizing atmosphere
A-109	Olivine	same olivine as A-097; fired at 1600°C for 4 h, oxidizing atmosphere; dark brown to black color
02	Magnesite	White magnesite raw material; coarse grained
03	Magnesite	White magnesite raw material; very fine grained

to be continued...

continuation of Table B.2

Sample	Type	Description
A-099	Periclase	Sample 02; decarbonatized at 800°C for 4 h, oxidizing atmosphere
A-111	Periclase	Sample 03; decarbonatized at 1600°C for 4 h, oxidizing atmosphere
A-100	Periclase	Decarbonatized magnesite (Sample 02); T = 800°C; 4 h; oxidizing atmosphere
A-112	Periclase	Decarbonatized magnesite (Sample 03); T = 1600°C; 4 h; oxidizing atmosphere

Table B.3: List of samples of unused refractories and slags from ladel and tundish.

Sample	Type	Description
06	Slag	Unused silica rich tundish slag; is composed of the ash of burned rice pealing; high content of carbon
74/1	Brick	MgO-C refractory brick (steel plant A); used as lining in the basic ladles
100	Brick	Mg-C brick, basic ladle, slag zone (steel plant A)
103	Brick	Brick from the bottom side of the ladle (unused, steel plant C); MgO-C brick; large periclase embedded in C rich matrix
104	Brick	MgO-C brick from the inner wall of the ladle (unused, steel plant C); in appearence similar to Sample 103
105	Brick	Mg-C brick used in the upper part of the ladle (unused, steel plant C)
106	Brick	MgO-CaO-C brick; ladle (unused, steel plant C); very sensitive to hydration processes; disintegrated at air
116	Brick	Andalusite refractory brick (steel plant B); remains of andalusite; not entirely mullitized
117	Brick	Andalusite refractory brick (steel plant B); brown iron oxide inclusions; beige gray color; mullitized andalusite
118	Brick	Andalusite refractory brick (steel plant B); brown iron oxide inclusions; beige gray color; mullitized andalusite

Table B.4: List of the samples of used refractories from ladle and tundish.

Sample	Type	Description
54	SEN	Black submerged entry nozzle (steel plant A)
75a/1	Castable	High alumina castable; bottom of basic lined ladles (steel plant A); white to gray
76a/1	Castable	White to gray high alumina castable; neutral ladle (steel plant A)

to be continued...

continuation of Table B.4

Sample	Type	Description
101	Castable	High alumina castable; neutral ladle lining (steel plant A); adjacent dark slag and veinlets of infiltrated slag
102	Ar-Nozzle	White argon stirring nozzle from the bottom side of the ladle (steel plant A)

Table B.5: List of samples of the sprayed tundish lining (STL), the tundish slag (TS), and of clogging (CL-X)taken in steel plant A. The clogging samples were taken along the inner walls of the SEN (CL-I) or from the bottom side (CL-B). The sample list is subdivided into blocks of samples which were taken from the same charges.

Sample	Type	SEN	Description
29/1	CL-I	3	Oxide deposit; SEN lower part
30/1	CL-I	4	Thin oxide deposit; SEN lower part
32/1	TL-M		Tundish lining; adjacent steel
32/2	TL-C		
32/3	TL-UA		
33/1	TS		Glassy tundish slag
36/1	CL-I	1	Thick oxide deposits, SEN lower part
37/1	CL-I	2	Thick deposits, SEN lower part
42/1	TL-M		
42/2	TL-C		
42/3	TL-UA		
43/1	TS		Glassy tundish slag; brownish green
52/1	CL-I		cm-thick bright gray deposit, white fraction, SEN lower part
52/2	CL-I		cm-thick bright gray deposit, yellowish fraction of Sample 52/1, SEN lower part
53/1	CL-I		Thin white deposit, SEN central part
54/1	CL-I	2	SEN lower part
54/2	CL-I	2	SEN central part
54/4	SEN	2	SEN, one layer, T46
55/2	CL-I	2	Thin white deposit, SEN central part
56/1	CL-B	2	SEN contact zone
56/2	CL-B	2	Central part of bottom side precipitates
56/3	CL-B	2	SEN bottom side precipitate; steel melt contact
57/1	TS		
58a/1	TL-UA		
58a/2	TL-C		
58a/3	TL-M		
59a/1	TS		

to be continued...

continuation of Table B.5

Sample	Type	SEN	Description
58b/1	CL-B	3	SEN contact zone
58b/2	CL-B	3	Central part of the deposit
58b/3	CL-B	3	Steel melt contact
59b/1	CL-I	3	Thin, dark gray deposit, SEN central part
60/1	CL-B	4	Steel melt contact
60/2	CL-B	4	Central part
60/3	CL-B	4	SEN contact
61/1	CL-I	4	Thin white deposit, SEN central part, low Fe content
62/1	CL-I	3	Thick white deposit, SEN lower part
63/	CL-I	4	Thick white deposit, SEN lower part
66/1	TS		
66/1	TS		
67/1	TL-UA		Sprayed tundish lining, unaltered side (T41)
67/2	TL-M		Melt contact
70/1	CL-I	3	Thick yellowish to white colored deposit, SEN lower part, white fraction, much Fe
70/2	CL-I	3	Yellowish fraction of Sample 70, much Fe
71/1	CL-I	4	Thick yellowish-white deposit, SEN lowerer part, white fraction, much Fe
71/2	CL-I	4	Yellowish fraction of Sample 71, much Fe
72/1	TL-UA		
72/2	TL-C		
72/3	TL-M		Sprayed tundish lining, melt contact, blue colored vitreous separates of adjacent TS
72/4	TL-M		
73/1	TS		Brownish to black colored, porous tundish slag
87/1	CL-B		Steel melt contact
87/2	CL-I		White to gray colored deposit
87/5	CL-B		Central part, much Fe
87/6	CL-B		SEN contact, much Fe
88/1	CL-I	2	Consolidated deposit, SEN central part
89/1	TL-UA		
89/2	TL-C		
89/3	TL-C		
90/1	TS		

Table B.6: List of samples of reduced ladle slag which were taken in steel plant A during sampling campaign. This type of slag is used in basic lined ladles.

Sample	Type	Description
75b/1	LS	Sample taken during steel refinement, final composition: Sample 76b/1
76b/1	LS	
77/1	LS	
78/1	LS	Sample taken during steel refinement, final composition: Sample 79/1
79/1	LS	
80/1	LS	Sample taken during steel refinement, final composition: Sample 81/1
81/1	LS	
82/1	LS	
83/1	LS	
84/1	LS	
85/1	LS	
86/1	LS	

Table B.7: Steel analyses and corresponding samples (steel plant A, data reported in wt.%)

Steel	Corresponding samples	C	Si	Mn	Al
1	58b, 59b, 60, 61, 62, 63, 66, 67	0.093	0.027	0.378	0.039
2	36,37,42,43	0.194	0.175	1.326	0.037
3	52, 53, 54, 55, 56, 57, 58a, 59a	0.051	0.015	0.220	0.032
4	24, 25, 26, 27, 28, 31	0.034	0.017	0.224	0.033
5	29, 30, 32, 33	0.021	0.020	0.245	0.041

Appendix C

Oxygen isotope analyses

Table C.1: Oxygen isotope composition of clogging samples from steel plant A. The data are reported in ‰.

Date	Sample	δ^{18}O [‰]	Aver. [‰]	Date	Sample	δ^{18}O [‰]	Aver. [‰]
25/06/99	29/1 A	11.02	10.7	09/09/99	59b/1 A	10.59	10.1
01/07/99	29/1 B	10.47		09/09/99	59b/1 B	9.61	
25/06/99	30/1 A	10.90	10.4	09/09/99	60/1 A	4.87	4.7
26/06/99	30/1 B	9.96		09/09/99	60/1 B	4.59	
20/07/99	36/1 A	11.48	11.4	09/09/99	60/2 A	8.92	8.6
20/07/99	36/1 B	11.24		09/09/99	60/2 B	8.28	
20/07/99	37/1 A	11.74	11.2	09/09/99	60/3 A	11.94	11.2
20/07/99	37/1 B	10.61		09/09/99	60/3 B	10.37	
07/08/99	52/2 A	8.98	8.2	09/09/99	61/1 A	12.32	12.5
07/08/99	52/2 B	7.39		09/09/99	61/1 B	12.64	
26/07/99	53/1 A	9.55	9.6	09/09/99	62/1 A	5.12	6.7
17/03/00	55/1 A	13.65	13.7	09/09/99	62/1 B	8.26	
17/03/00	55/1 B	13.83		10/09/99	63/1 B	8.10	8.1
08/08/99	56/1 A	12.66	11.8	17/03/00	70/1 A	10.30	10.6
08/08/99	56/1 B	10.88		17/03/00	70/1 B	10.83	
08/08/99	56/2 B	8.91	8.9	17/03/00	70/2 A	6.35	6.3
08/09/99	56/3 A	4.92	5.8	17/03/00	70/2 B	6.17	
08/09/99	56/3 B	6.69		20/04/00	87/1 A	11.00	11.0
08/09/99	58b/1 A	10.11	9.9	04/05/00	87/1 B	11.00	
08/09/99	58b/1 B	9.72		20/04/00	87/2 A	12.20	11.6
08/09/99	58b/2 A	9.07	8.6	04/05/00	87/2 B	11.07	
08/09/99	58b/2 B	8.19		20/04/00	87/5 A	8.30	8.8
08/09/99	58b/3 A	6.19	5.7	04/05/00	87/5 B	9.29	
08/09/99	58b/3 B	5.23		20/04/00	87/6 A	8.10	9.2
				04/05/00	87/6 B	10.26	

Table C.2: Oxygen isotope composition of samples of the sprayed tundish lining from steel plant A. The data are reported in ‰

Date	Sample	δ^{18}O [‰]	Aver. [‰]	Date	Sample	δ^{18}O [‰]	Aver. [‰]
25/06/99	32/1 A	13.43	13.0	20/07/99	42/3 A	12.51	12.1
01/07/99	32/1 B	12.49		20/07/99	42/3 B	11.67	
25/06/99	32/2 A	11.44	11.4	08/09/99	58a/2 A	10.97	11.0
25/06/99	32/3 A	11.85	11.5	08/09/99	58a/3 A	11.50	11.5
01/07/99	32/3 B	11.19		12/11/99	67/1 A	12.41	12.7
20/07/99	42/1 A	15.86	16.0	12/11/99	67/1 B	12.95	
20/07/99	42/1 B	16.08		14/11/09	72/1 A	11.51	11.5
20/07/99	42/2 A	12.78	12.9	14/11/09	72/2 A	12.20	12.2
20/07/99	42/2 B	13.00		14/11/09	72/3 A	17.90	17.9

Appendix D

XRF-Analyses

Table D.1: Major, minor, and trace element composition of different periclase raw material samples as determined by XRF. Sample 109 is used as raw material in the sprayed tundish lining. Data of major and minor elements are reported in wt.% of the oxides, data of trace elements in ppm.

Sample	SiO_2	TiO_2	Al_2O_3	Fe_2O_3	CaO	MgO	MnO	Na_2O	K_2O	P_2O_5	Total
109	4.77	0.04	0.80	0.76	1.22	92.95	0.02	0.06	<0.01	0.06	100.68
107	0.70	0.01	0.12	0.12	1.96	98.27	0.02	0.09	<0.01	<0.01	101.29
108	2.12	0.02	0.57	0.54	1.41	96.16	0.07	0.03	<0.01	0.09	101.01
110	0.84	0.01	0.11	0.12	1.96	98.34	0.01	0.06	<0.01	<0.01	101.45
111	0.58	<0.01	0.08	0.45	0.74	96.22	0.08	0.06	<0.01	0.02	98.23
112	2.21	0.02	0.53	2.34	0.89	93.83	0.70	0.05	<0.01	0.04	100.61

Sam.	Sc	V	Cr	Co	Ni	Cu	Sr	Y	Zr	Nb	Ba	La	Ce	Pr	Nd	Hf
109	<2	9	10	44	17	183	26	11	13	<2	19	<5	<6	<3	<3	2
107	5	<3	<5	62	17	194	11	5	<2	<2	<6	5	<6	<3	<3	<2
108	8	5	<5	174	21	212	17	4	4	<2	<6	8	<6	<3	<3	3
110	7	20	<5	50	28	213	21	6	<2	<2	36	<5	21	4	<3	3
111	9	33	<5	46	26	220	4	22	<2	<2	<6	<5	9	10	<3	3
112	8	23	25	125	43	194	34	3	6	<2	16	43	<6	<3	<3	<2

Table D.2: Major, minor and trace element analyses of a submerged entry nozzle (SiC-C-Al_2O_3, sample 54) and of a spinel forming, high alumina refractory castable (Sample 76a, XRF analyses). Data of major and minor elements are reported in wt.% of the oxides, data of trace elements in ppm.

Sam.	SiO_2	TiO_2	Al_2O_3	Fe_2O_3	CaO	MgO	MnO	Na_2O	K_2O	P_2O_5	L.O.I.	Total
76a/1	2.33	0.02	87.92	2.67	0.06	4.87	<0.01	1.28	1.56	0.01	n.d.	100.72
54/4	12.36	1.96	70.39	0.68	0.37	0.20	0.01	1.32	0.06	0.08	13.46	100.89

Sample	Sc	V	Cr	Co	Ni	Rb	Sr	Y	Zr	Nb	Ba	La	Ce	Pr	Nd	Hf
76a/1	30	3	130	473	354	2	2	26	2	19	6	96	6	19	3	8
54/4	28	28	56	611	168	2	152	67	1452	2	6	5	174	42	3	38

Table D.3: Major, minor and trace element composition of different basic refractory bricks. Sample 74/1 and 100 are samples of used material from steel plant A. The other samples are unused bricks made available by R. Broß. With exception of Sample 74/1, all samples were annealed prior to analysis. Data of major and minor elements are reported in wt.% of the oxides, data of trace elements in ppm.

Sample	SiO_2	TiO_2	Al_2O_3	Fe_2O_3	CaO	MgO	MnO	Na_2O	K_2O	P_2O_5	Total
103	1.01	0.01	0.44	0.30	1.98	97.65	0.02	0.08	<0.01	0.08	101.57
104	0.97	0.01	0.32	0.34	1.87	94.17	0.02	0.02	<0.01	0.06	97.78
105	0.88	0.01	0.15	0.22	1.98	97.81	0.02	0.07	<0.01	0.04	101.18
106	1.35	0.03	0.47	0.69	40.31	57.29	0.12	<0.02	<0.01	0.03	100.29
100	1.73	0.02	0.44	0.62	1.78	97.09	0.04	0.05	<0.01	0.05	101.82
74/1	0.87	0.01	0.56	0.44	0.04	84.39	0.04	1.69	0.57	0.01	88.62

Sample	Sc	V	Cr	Co	Ni	Cu	Sr	Y	Zr	Nb	Ba	La	Ce	Pr	Nd	Hf
103	6	13	21	36	28	204	37	7	3	<2	31	36	<6	10	<3	2
104	13	10	35	38	30	196	30	<2	5	<2	25	50	<6	<3	<3	<2
105	<2	5	56	75	51	194	31	6	<2	<2	21	14	<6	<3	<3	4
106	<2	17	75	21	32	157	77	11	20	<2	12	<5	13	8	6	2
100	3	27	54	31	95	195	22	8	22	<2	<6	8	12	4	30	4
74/1	2	8	261	11	35	3	18	8	14	2	6	55	6	16	3	2

Table D.4: Major, minor, and trace element analyses of bulk samples of tundish lining (XRF analyses). Data of major and minor elements are reported in wt.% of the oxides, data of trace elements in ppm.

Sam.	SiO_2	TiO_2	Al_2O_3	Fe_2O_3	P_2O_5	MgO	MnO	CaO	Na_2O	K_2O	L.O.I.	Total
32/1	22.56	4.51	9.67	3.98	0.03	55.95	1.62	1.19	0.50	0.15	-0.17	99.99
32/2	18.58	0.74	1.84	4.03	0.11	71.46	0.12	2.89	0.61	0.12	0.08	100.58
32/3	17.71	0.16	1.15	4.01	0.07	75.54	0.10	1.76	0.56	0.05	0.04	101.15
42/1	31.26	0.19	10.44	3.14	0.11	43.45	6.72	3.30	1.17	0.14	-0.91	99.01
42/2	21.93	0.12	3.86	3.23	0.08	64.16	2.56	2.76	0.60	0.07	-0.12	99.25
42/3	18.75	0.08	1.72	3.64	0.12	73.52	0.10	2.23	0.68	0.04	-0.10	100.78
58a/1	18.76	0.07	1.69	3.67	0.08	73.93	0.27	1.61	0.55	0.05	n.d.	100.68
58a/2	19.82	0.11	2.17	3.58	0.15	70.07	0.10	3.50	0.64	0.17	n.d.	100.31
58a/3	24.72	0.08	8.33	4.27	0.05	57.48	1.96	2.52	0.49	0.14	n.d.	100.04
67/1	17.73	0.08	2.00	2.83	0.08	75.29	0.11	1.69	0.86	0.03	0.33	101.03
67/2	25.07	0.14	8.39	2.75	0.04	57.97	2.73	1.88	0.48	0.08	-0.32	99.21
72/1	17.11	0.07	1.78	2.75	0.08	76.18	0.10	1.63	0.74	0.10	0.14	100.68
72/2	22.90	0.21	6.35	3.10	0.05	59.80	4.47	1.54	0.52	0.09	-0.43	98.60
89/1	18.36	0.06	1.24	3.83	0.11	74.30	0.09	1.60	0.57	0.04	-0.07	100.13
89/2	21.90	0.20	4.47	3.34	0.07	62.70	1.89	4.78	0.47	0.14	-0.19	99.77
89/3	26.96	0.22	7.69	3.87	0.09	51.57	5.04	3.19	1.39	0.08	-0.91	99.19

Sample	Sc	V	Cr	Co	Ni	Rb	Sr	Y	Zr	Nb	Ba	La	Ce	Pr	Nd	Hf
32/1	2	113	1331	88	772	7	10	8	162	2	22	55	40	10	22	5
32/2	9	11	775	102	749	5	62	12	89	8	52	37	20	12	24	5
32/3	4	17	831	66	818	2	37	11	34	3	70	80	6	3	3	3
42/1	20	3	474	209	564	31	14	41	137	67	6	94	67	5	65	13
42/2	8	22	648	124	573	2	42	16	241	41	32	71	6	10	3	6
42/3	2	15	749	83	752	2	51	11	133	11	65	50	45	14	21	4
58a/1	10	9	806	106	758	2	34	11	121	8	55	90	6	8	3	4
58a/2	2	17	747	97	702	3	84	14	204	5	130	38	6	3	3	5
58a/3	19	21	1835	89	691	8	14	9	206	4	21	79	6	12	3	5
67/1	23	12	955	140	749	4	45	12	36	2	17	54	6	7	3	3
67/2	15	33	2306	119	660	2	17	2	57	6	6	68	45	10	14	2
72/1	9	29	870	80	695	4	48	12	31	4	6	116	6	3	15	2
72/2	9	22	906	230	578	9	8	6	225	9	18	84	6	12	8	6
89/1	7	6	753	91	842	2	34	7	19	2	57	91	6	3	3	2
89/2	5	33	579	85	605	2	81	12	71	154	176	78	107	28	44	2
89/3	26	87	646	56	615	2	17	23	7	151	6	67	6	41	3	9

Table D.5: Major, minor, and trace element analyses of tundish slag (XRF analyses). Data of major and minor elements are reported in wt.% of the oxides, data of trace elements in ppm.

Sam.	SiO_2	TiO_2	Al_2O_3	Fe_2O_3	P_2O_5	MgO	MnO	CaO	Na_2O	K_2O	L.O.I.	Total
6/1	92.04	0.01	0.17	0.10	0.66	0.18	0.74	0.50	0.02	2.02	4.79	101.23
33/1	46.53	12.10	16.14	6.29	0.14	3.76	6.62	7.54	1.03	0.55	-0.62	100.07
43/1	54.10	0.27	11.40	6.40	0.21	13.55	4.85	4.92	0.83	0.60	0.00	97.12
57/1	50.02	0.32	25.15	3.07	0.19	4.76	10.64	3.61	0.97	0.55	0.00	99.29
59a/1	45.09	0.19	28.11	3.99	0.13	6.02	8.32	6.50	1.17	0.48	0.00	100.00
66/1	45.24	0.24	18.12	6.72	0.13	7.39	5.85	13.98	1.09	0.75	-0.69	98.83
72/3	45.88	0.42	20.25	2.69	0.30	7.10	4.19	16.53	1.14	0.90	-0.91	98.50
73/1	51.69	0.56	15.11	2.75	0.19	14.36	5.05	5.65	1.01	0.62	0.00	96.99
90/1	50.37	0.43	13.58	4.26	0.22	10.02	11.13	7.96	1.56	0.70	-0.70	99.53

Sample	Sc	V	Cr	Co	Ni	Rb	Sr	Y	Zr	Nb	Ba	La	Ce	Pr	Nd	Hf
6/1	2	3	5	37	29	72	14	3	71	2	127	57	13	9	3	2
33/1	70	201	565	154	287	28	25	56	241	15	6	96	6	35	3	14
43/1	90	34	1196	133	615	55	26	36	46	101	27	322	6	18	4	13
57/1	10	14	3268	132	338	30	23	32	5403	2	134	177	22	3	3	111
59a/1	47	46	1529	137	286	22	37	27	67	2	6	147	6	3	3	11
66/1	51	20	1691	103	368	36	30	38	19	9	6	110	6	20	13	11
72/3	15	34	630	347	261	39	33	33	258	13	110	111	6	43	3	16
73/1	2	9	4434	142	339	19	31	16	160	2	32	162	6	18	3	8
90/1	21	169	1386	102	421	49	56	54	13	305	43	187	6	6	3	8

Table D.6: Major, minor, and trace element XRF analyses of clogging from inside the submerged entry nozzle. Data of major and minor elements are reported in wt.% of the oxides, data of trace elements in ppm. All analyses were normalized to 100 wt.% of the total of major and minor elements. Iron was excluded from the data because of varying of iron metal (3–49 wt.%) adjacent to many samples and Fe $\gg$ (Fe^{2+}+Fe^{3+}).

Sample	SiO_2	TiO_2	Al_2O_3	CaO	MgO	MnO	Na_2O	K_2O	P_2O_5	ZrO_2	Total
29/1	2.98	2.90	90.36	0.48	0.15	0.37	0.90	0.02	0.08	1.75	100.00
30/1	1.77	2.94	91.39	0.51	0.16	0.18	1.78	0.01	0.09	1.15	100.00
36/1	10.12	0.30	58.67	12.17	13.52	1.45	3.58	0.09	0.07	0.03	100.00
37/1	10.60	0.38	58.44	12.78	12.54	0.99	4.02	0.10	0.07	0.08	100.00
52/1	0.15	0.21	92.80	1.26	3.37	0.07	1.42	0.51	0.01	0.19	100.00
52/2	0.40	0.13	93.92	1.17	2.67	0.18	1.16	0.33	0.02	0.04	100.00
54/1	0.35	0.23	94.36	1.41	2.41	0.15	0.84	0.18	0.03	0.04	100.00
54/2	2.81	0.10	90.14	1.57	3.24	0.59	1.15	0.37	0.02	0.02	100.00
62/1	1.61	0.08	84.42	2.27	9.42	0.14	1.79	0.01	0.06	0.18	100.00
63/1	1.24	0.07	82.85	2.35	11.58	0.14	1.68	0.01	0.05	0.01	100.00
70/1	0.18	0.18	87.73	3.91	6.66	0.30	0.46	0.01	0.02	0.54	100.00
70/2	0.17	0.07	85.50	3.32	9.17	0.82	0.64	0.01	0.03	0.26	100.00
71/1	0.42	0.14	83.20	4.80	9.82	0.57	0.42	0.01	0.03	0.59	100.00
71/2	1.51	0.10	84.54	3.12	8.64	0.96	0.64	0.01	0.03	0.44	100.00
87/2	1.41	0.08	64.74	12.03	20.73	0.24	0.45	0.01	0.04	0.26	100.00
53/1	1.42	0.13	92.35	1.30	1.04	0.06	2.96	0.62	0.05	0.05	100.00
55/1	6.38	0.70	90.27	1.56	0.25	0.05	0.66	0.02	0.06	0.06	100.00
59b/1	0.45	0.82	90.47	1.12	1.75	0.11	1.09	0.03	0.10	4.06	100.00
61/1	2.11	0.36	85.56	4.39	2.76	0.18	2.11	0.03	0.11	2.38	100.00

Sample	Sc	V	Cr	Co	Ni	Rb	Sr	Y	Nb	Ba	La	Ce	Pr	Nd	Hf
29/1	26	35	195	266	9	15	4	18	33	432	402	13	24	7	219
30/1	2	60	180	1079	711	25	2	11	13	7	17	7	32	80	164
36/1	52	63	59	554	360	27	147	131	51	199	271	252	51	179	17
37/1	14	29	145	249	478	24	195	138	34	381	346	210	49	147	21
52/1	18	6	61	355	100	4	34	12	7	35	88	11	7	3	27
52/2	7	4	64	385	121	7	23	8	14	47	83	37	5	8	7
54/1	4	6	74	221	80	4	34	6	2	67	176	22	9	12	7
54/2	3	3	152	484	66	13	4	10	18	13	96	28	3	3	3
62/1	39	4	114	755	362	17	2	59	13	7	166	114	15	37	37
63/1	14	22	24	221	294	3	2	47	12	6	251	6	7	117	14
70/1	24	17	12	466	32	4	271	113	9	441	295	526	62	282	74
70/2	23	4	85	754	84	2	330	143	6	728	361	572	70	382	37
71/1	32	19	54	560	95	2	306	128	4	442	331	533	68	337	79
71/2	22	16	35	1111	81	6	258	110	16	598	277	559	54	309	61
87/2	28	55	93	216	268	6	424	197	43	825	441	816	92	533	37
53/1	40	64	61	702	348	31	2	56	2	6	5	171	32	81	19
55/1	16	38	27	79	145	23	81	36	34	685	305	14	34	7	14
59b/1	5	21	74	1199	11	5	40	5	5	16	13	53	27	141	558
61/1	41	54	235	1057	263	34	52	52	23	80	27	251	52	123	341

Table D.7: Major, minor, and trace element analyses (XRF) of clogging samples taken from the bottom side of the SEN. Data of major and minor elements are reported in wt.% of the oxides, data of trace elements in ppm.

Sample	SiO_2	TiO_2	Al_2O_3	CaO	MgO	MnO	Na_2O	K_2O	P_2O_5	ZrO_2	Total
56/1	2.53	1.42	91.85	2.35	0.30	0.03	1.28	0.01	0.09	0.12	100.00
56/2	3.31	0.21	91.62	1.60	1.25	0.11	1.68	0.13	0.05	0.02	100.00
56/3	2.47	0.16	88.62	1.98	1.61	0.10	3.88	1.07	0.06	0.03	100.00
58b/1	2.51	0.70	90.35	1.44	0.64	0.05	1.67	0.01	0.10	2.49	100.00
58b/2	2.71	0.10	87.08	5.54	2.59	0.07	1.58	0.01	0.08	0.23	100.00
58b/3	2.04	0.07	84.44	4.04	5.79	0.10	3.22	0.11	0.05	0.13	100.00
60/1	4.20	0.21	82.73	1.45	7.25	0.82	3.02	0.16	0.06	0.10	100.00
60/2	3.90	0.19	90.36	0.95	2.32	0.24	1.66	0.01	0.09	0.25	100.00
60/3	2.18	0.84	91.89	0.64	0.12	0.05	1.24	0.01	0.11	2.89	100.00
87/1	1.84	0.44	91.68	1.54	2.37	0.60	0.55	0.04	0.03	0.91	100.00
87/5	2.32	0.56	86.04	2.66	4.37	1.20	1.86	0.01	0.05	0.93	100.00
87/6	1.15	0.51	86.65	3.10	6.07	1.42	0.64	0.09	0.03	0.34	100.00

Sample	Sc	V	Cr	Co	Ni	Rb	Sr	Y	Nb	Ba	La	Ce	Pr	Nd	Hf
56/1	68	98	98	2092	332	15	86	65	18	6	5	299	20	3	31
56/2	75	4	111	3342	467	24	7	47	5	7	6	7	4	4	18
56/3	36	38	60	3119	482	38	2	44	17	7	95	7	4	4	19
58b/1	2	48	36	1274	304	28	32	26	2	72	252	44	40	116	354
58b/2	45	3	37	852	297	9	13	51	2	21	29	7	13	3	44
58b/3	2	35	65	1243	303	3	2	17	2	7	38	204	79	34	26
60/1	2	3	339	1056	509	39	2	50	10	7	62	7	3	3	29
60/2	17	4	140	1960	470	45	2	35	12	107	253	7	4	4	48
60/3	2	3	81	2128	245	28	35	4	2	26	96	15	20	3	408
87/1	2	173	95	856	155	2	29	3	63	270	107	94	21	63	122
87/5	2	109	141	912	299	28	50	71	64	192	193	34	3	67	134
87/6	24	154	81	524	135	6	77	43	75	216	185	226	38	123	46

Table D.8: XRF major, minor and trace element composition of reduced ladle slag. Analyses were performed by XRF on pressed powder pellets. Data of major and minor elements are reported in wt.% of the oxides, data of trace elements in ppm.

Sam.	SiO_2	TiO_2	Al_2O_3	Fe_2O_3	CaO	MgO	MnO	Na_2O	K_2O	P_2O_5	SO_3	F	L.O.I.	Total
75b/1	6.79	0.19	28.02	1.22	55.45	5.90	0.06	1.27	0.01	0.06	0.03	2.84	n.d.	101.83
76b/1	6.73	0.18	28.60	0.79	55.71	5.75	0.06	1.08	0.01	0.04	0.21	2.96	n.d.	102.13
77/1	8.50	0.22	21.18	1.43	42.60	24.89	0.14	1.51	0.01	0.10	0.26	4.18	-1.65	103.37
78/1	5.96	0.20	29.82	1.30	52.99	5.68	0.07	1.35	0.01	0.08	0.38	3.24	-2.42	98.66
79/1	4.73	0.18	28.37	0.31	54.77	5.81	0.08	0.35	0.01	0.02	1.83	4.96	-2.00	99.43
80/1	6.30	0.18	19.56	0.91	47.98	19.82	0.10	0.52	0.01	0.03	2.32	6.03	-2.59	101.17
81/1	6.10	0.17	19.64	0.95	48.60	19.69	0.09	0.43	0.01	0.03	2.04	4.91	-2.01	100.65
82/1	4.84	0.19	25.07	0.33	54.89	9.99	0.07	0.38	0.01	0.02	1.78	2.16	-0.24	99.48
83/1	8.03	0.29	25.07	0.33	56.02	6.82	0.10	0.35	0.01	0.03	2.86	2.29	-3.23	98.96
84/1	10.07	0.29	25.12	0.28	55.89	6.88	0.10	0.66	0.10	0.02	2.90	2.15	-3.21	101.25
85/1	5.81	0.16	28.08	0.37	55.27	6.26	0.07	0.31	0.01	0.02	2.63	2.05	-2.85	98.19
86/1	6.86	0.26	27.42	0.78	54.44	6.86	0.07	0.35	0.01	0.02	2.36	2.02	-3.11	98.35

Sample	V	Cr	Co	Ni	Sr	Y	Zr	Nb	Ba	La	Ce	Pr	Nd	Hf	Ta	Pb
75b/1	28	5	62	246	202	31	117	2	93	85	103	56	3	9	2	50
76b/1	60	5	60	267	164	50	61	20	162	244	92	29	71	15	20	3
77/1	3	82	2	231	165	38	105	26	325	26	6	13	3	9	36	44
78/1	3	48	195	353	178	27	90	16	162	261	87	34	97	12	38	3
79/1	10	5	28	29	244	27	203	25	199	136	9	6	13	3	2	16
80/1	3	112	15	61	198	18	138	28	180	125	6	3	18	3	2	3
81/1	25	100	24	29	202	22	138	29	170	70	32	14	27	3	5	10
82/1	3	8	16	20	242	17	164	13	185	74	10	13	19	3	5	27
83/1	3	89	49	64	245	12	216	2	154	119	38	7	15	4	18	25
84/1	15	42	23	32	248	22	221	3	657	61	6	8	19	4	2	20
85/1	3	5	48	55	245	14	175	12	167	108	6	4	3	3	5	12
86/1	3	5	56	38	243	17	278	18	169	97	58	6	26	6	2	36

Appendix E

Electron-probe microanalyses

The results of all EP-microanalyses would require more than hundred printed pages. Therefore, the author has decided to add these data electronically as PDF-documents. In the printed version, these documents are available on the attached CD-ROM disk (ISO9660 with Joilet extension). In the online-version of this thesis, hyperlinks in the PDF-document refer to the respective data files.

E.1 Fired olivine raw material

- Olivine (fired at 800°C)
- Glass (fired at 1600°C)
- Magnesioferrite (fired at 1600°C)
- Olivine (fired at 1600°C)

E.2 Clogging

- Calcium-*di*-aluminate
- Corundum
- Wuestite
- Gehlenite
- Hematite
- Iron (EMP-calibration on oxide standards)
- Linescans (Sample 48) 1, 2, 3, 4
- SiC
- Spinel
- Ti-rich phase

E.3 Ladle lining

- Calcium-*mono*-aluminate
- Calcium-*di*-aluminate
- Calcium-*hexa*-aluminate, Hibonite
- Corundum
- Gehlenite
- Iron (EMP-calibration on oxide standards)
- Peroskite
- Spinel
- Wuestite

E.4 Sprayed tundish lining

- Chromite
- Glass
- Olivine
- Spinel
- Linescans (Sample 42) 1, 3, 4
- Grids (Sample 89) 1, 2

E.5 Tundish slag

- Glass
- Spinel